SAW based phononic crystal microfluidic sensor platform

Dissertation

zur Erlangung des akademischen Grades

Doktoringenieur
(Dr.-Ing.)

Von: Dipl. –Ing. Aleksandr Oseev

geboren am: 06.07.1983 in Borovichi

genehmigt durch
die Fakultät für Elektrotechnik und Informationstechnik
der Otto-von-Guericke-Universität Magdeburg

Gutachter: Prof. Dr. –Ing. Ulrike Steinmann

              Prof. Dr. –Ing. Michael J. Vellekoop

Promotionskolloquium am: 20.09.2017

SAW BASED PHONONIC CRYSTAL

MICROFLUIDIC SENSOR PLATFORM

Dipl.-Ing. Aleksandr Oseev

Institute of Micro and Sensor Systems (IMOS)

Otto-von-Guericke-University Magdeburg

This dissertation is submitted for the degree of Doctor of Philosophy

January 2017

To my family

SUMMARY

Current contribution demonstrates the author's original scientific work in a field of microfluidic sensors driven by acoustic principles. The main purpose of current research is the development of a novel analytical platform based on phononic crystal sensor approach that allows integration of velocimetry based sensor concept into a single chip integrated solutions, such as Lab on a Chip devices or Micro Total Analysis Systems (µTAS). To complete the research task, author introduce novel sensor concept that merges advantages of ultrasonic velocimetry analytic systems and microacoustic sensor approach (more specifically surface acoustic wave (SAW) sensors). That kind of sensor platform was not previously introduced and is currently the state of the art.

In contrast to classic SAW sensors that are mostly sensitive to near the surface effects, the proposed in current work solution allows detecting the volumetric properties of liquid analytes. More specifically, the detection of speed of sound of liquids, that gains the sensor response directly influenced by intermolecular interactions of analyte. To complete the sensor system with an ability to detect volumetric properties of liquids, the sensor concept based on phononic structure made as a periodic arrangement of microfluidic channels with confined within liquid analyte is proposed. It is performed as an integrated into SAW device planar solution, that makes the sensor competitive with miniaturized system platforms.

Current research work includes fundamental theoretical investigations with numerical methods of resonances in periodic arrangement of microfluidic channels integrated into SAW devices. Obtained numerical simulation results demonstrate rather complex structure vibration with several isolated acoustic modes that respond to material properties of confined within liquid analyte. To confirm the theoretical predictions, the sensor arrangement was fabricated. The respective technological process was developed and completed by the author within the framework of current research. Results of conducted experimental investigations confirm theoretical findings and proof the proposed sensor concept. The results of current work can be utilized for novel miniaturized on a single chip based analytical platforms for bio-medical and many other applications.

ZUSAMMENFASSUNG

Die Entwicklung einer neuartigen analytischen Plattform ist Gegenstand dieser Arbeit. Diese Plattform basiert auf dem phononischem Kristallsensoransatz. Das geschwindigkeitsmessungsbasierte Sensorkonzept wird in einem Chip integriert, wie es bei Lab on a Chip und Micro Total Analysis Systems(µTAS) zur Anwendung kommt. Es wird ein neuartiges Sensorkonzept vorgestellt, das die Vorteile der analytischen Systeme der Ultraschall-Geschwindigkeitsmessung und des mikroakustischen Sensoransatzes (insbesondere der SAW-Sensoren) zusammenführt. Diese Art von Sensorplattform wurde bisher nicht eingeführt und ist derzeit der Stand der Technik.

Im Gegensatz zu klassischen SAW-Sensoren, die meist nahe den Oberflächen empfindlich sind, ermöglicht, das in dieser Arbeit vorgeschlagene Sensorkonzept, die Messung der volumetrischen Eigenschaften von flüssigen Analyten. Die Schallgeschwindigkeit von Flüssigkeiten, die die Sensorantwort enthält, ist abhängig von den intermolaren Wechselwirkungen. Basierend auf einer phonischen Struktur, welche als periodische Anordnung von mikrofluidischen Kanälen mit eingeschlossenen flüssigen Analyten ausgeführt ist, wird ein Sensorkonzept vorgeschlagen, das die volumetrischen Eigenschaften detektiert.

Aktuelle Forschungsarbeiten umfassen fundamentale theoretische Untersuchungen mit numerischen Methoden der Resonanzen in der periodischen Anordnung von mikrofluidischen Kanälen, die SAW-Strukturen enthalten. Numerische Simulationsergebnisse zeigen eine komplexe Strukturvibration mit mehreren isolierten akustischen Moden, die auf Materialeigenschaften, die in einem flüssigen Analyten eingeschlossen sind, reagieren. Die Sensoranordnung wurde hergestellt, um die theoretischen Ergebnisse zu bestätigen. Das jeweilige technologische Verfahren wurde im Rahmen der Arbeit entwickelt und ergänzt. Die Ergebnisse der durchgeführten experimentellen Untersuchungen verifizieren die theoretischen Ergebnisse und bestätigen das vorgeschlagene Sensorkonzept. Die Ergebnisse dieser Arbeit können für neuartige miniaturisierte auf einem Single-Chip-basierte analytische Plattformen für bio-medizinische und viele andere Anwendungen genutzt werden.

ACKNOWLEDGEMENTS

CONTENTS

LIST OF TABLES

LIST OF FIGURES

LIST OF ABBREVIATIONS AND ACRONYMS

SAW - surface acoustic wave

MHz – megahertz

kHz - kilohertz

μm - micrometer

QCM - quartz crystal microbalance

IDT - interdigital transducer

PMMA - Poly(methyl methacrylate)

SU-8 - epoxy-based negative photoresist

DNA - Deoxyribonucleic acid

RON – research octane number

MEMS - Microelectromechanical systems

ZnO - Zinc oxide

Si - Silicon

FEM - finite element method

COMSOL - finite element analysis, solver and simulation software

FDTD - finite-difference time-domain method

ANSYS - engineering software developer

PML - perfectly matched layer

ST-cut - quartz wafer cut

AT-cut - quartz wafer cut

Z-cut - wafer cut

HF - high frequency

PnC – phononic crystal

PDMS – Polydimethylsiloxane

DI - deionized

HB – hard bake

SB – soft bake

PEB – post exposure bake

PVD - physical vapor deposition

TI Prime - adhesive promoter

AZ - photoresist developer

AZ400K - photoresist developer

mr600Dev - photoresist developer

ANPE - aluminum etcher

LS 500 ES - physical vapor deposition equipment

SUSS_MA6_BA6 - mask aligner

SUSS SB6E - substrate bonder

Zeiss EVO 50 - scanning electron microscope

FTR MicroProf 300 – profilometer

LiNbO3 - lithium niobate

AZ EBR - edge bead remover

SEM - scanning electron microscope

IF - intermediate frequency

SSMC – connector type

LIST OF APPENDICES

1 INTRODUCTION

In recent years, a general trend towards integration of analytical instruments into miniaturized platforms is observed for a broad variety of applications. The single chip integrated solutions, such as Lab on a Chip and Micro Total Analysis Systems (μTAS), require application of compatible approaches performing the functional elements of analytical systems. These systems include an ability to conduct on a single planar integrated solution basis the samples chemical analysis, analyte separation, manipulation and detection of specific targets. The platforms that are built upon those principles are aimed to operate with extremely small analyte volumes. This is advantageous, especially in case of biomedical applications. They allow to analyze the complex liquid probes non-invasively within a single analytical chip gaining all required information from the samples of down to picoliter volumes.

Acoustic methods of liquid analyses are well known and already applied since decades demonstrating great advantages in comparison to alternative approaches. Starting from a macro scale liquid analysis and raising new concepts in a micro scale by analyzing liquids in extremely low volumes, these methods serve as a convenient and well established analytical approach. The advantage of the method is in its ability to directly sense the result of interaction of analyte with acoustic wave. A variety of methods allows detecting the wave propagation through the liquid or interrogation of acoustic waves at a liquid-solid interface. The information about analyzed solution can be obtained from volumetric properties analysis, such as velocity of sound, density and viscosity; attenuation of the wave in liquid medium; mass load of absorbed analyte on

the propagation path and many other approaches. The acoustic methods of liquids analysis nowadays are widely utilized for chemical sensors, biosensors and in medical applications.

In a micrometer wavelength range, microacoustic devices provide a well-established platform for sensor realization. The advantages of microacoustic devices are in their relatively simple fabrication process, utilization of standard materials (such as quartz or lithium niobate), ability to be performed as a disposable sensor, relatively high sensitivity to perturbations of wave propagation path (mass load, change of surface electrical condition). Nowadays, microacoustic devices are widely utilized as delay lines, resonators and filters. These devices can be divided into several categories by the utilized wave type. Bulk acoustic wave devices, also known as quartz crystal microbalance (QCM) devices, are already widely applied as highly stable resonators that utilize a thickness shear bulk acoustic wave. Another category of microacoustic devices is the devices with an acoustic energy strongly confined at the surface of piezoelectric substrate (piezoelectric waveguide). So called surface acoustic wave (SAW) devices is a well-developed platform that is already utilized in a broad variety of applications especially as frequency selective devices. Since several decades the microacoustic devices attract a considerable attention for the utilization in sensor purposes.

Basic operational principle of SAW devices is an excitation and detection of acoustic waves with interdigital transducers (IDTs). In most cases, the input IDT excites a surface acoustic wave that travels along the waveguide surface and is detected by output IDT. The wave propagation path in most SAW devices remains open for interrogation with external medium, that can be utilized for sensor purposes. Due to high localization of acoustic energy at the waveguide surface, any change at surface boundary: mechanical (mass load, introduction of viscous medium) or electrical (conductivity change at the surface), vary the wave propagation. That kind of direct interrogation with a surface wave was initially utilized in Rayleigh wave SAW sensors. Tailoring the open part of SAW waveguide with sensitive polymers was one of the first sensor approaches allowing to complete the detection of organic gases. Later, the same concept based on sensitive layers was widely utilized to build various SAW based gas sensors. Early attempts of utilization of the same Rayleigh wave SAW devices for liquid sensor

purposes were unsuccessful because of strong radiation of Rayleigh wave into a liquid that was causing significant wave attenuation. The utilization of other wave types and liquid recognition layers allowed to realize the liquid sensors that provide an information based on near the surface effects, such as adsorption in sensitive layer or binding to recognition layer.

At the same time, methods of ultrasonic velocimetry that have development background similar to SAW devices, afford to conduct the volumetric properties analysis of liquid analytes. The utilization of ultrasonic measurement approaches allows detecting intermolecular interactions in multicomponent mixtures and material properties of separate liquids. The method is based on measurements of acoustic wave propagation parameters, such as sound velocity, attenuation, scattering, absorption and etc. In recent years, the methods of high resolution ultrasonic spectroscopy achieved a significant resolution and widely utilized for sensor purposes. One of the challenges of that approach is an ability to perform the sensor that can be integrated in planar Lab on a Chip platforms.

Recently introduced phononic crystal sensor platform provides an alternative solution for the sensor realization that utilizes advantages of ultrasonic velocimetry methods and provides an opportunity for the sensor miniaturization. As a result, it fulfills the required integration into Lab on a Chip planar platforms. The most critical point is an ability of the novel sensor system to satisfy high demands regarding sensitivity that developed sensor platforms have already demonstrated. The ability to measure a variation in speed of sound up to 0.1m/s and lower is the most critical point regarding the sensor performance. The current state of development of phononic crystal liquid sensors theoretically predicts the possibility of the concept to fulfill sensor demands to make the approach competitive to existing sensor systems and perspective considering integration in Lab on a Chip platforms.

1.1. Microacoustic liquid sensors

Nowadays microacoustic sensors are already a well-established concept that is applied for gas detection, liquids analysis, stress sensors, torque sensors, pressure sensors and other sensor systems. Adjusted for mass production fabrication process allows manufacturing cost efficient sensors for a broad variety of applications. The operation

principle of microacoustic devices is based on a propagation of bulk or surface acoustic waves. Initially bulk acoustic wave sensors [1–3] received in the past a great attention with respect to gas and liquid properties analysis. Thickness shear mode devices also known as quartz crystal microbalance (QCM) are bulk wave devices, where waves propagate in the complete piezoelectric substrate. QCMs are well known as devices which are sensitive to surface interactions. Thus, various QCMs are manufactured as different kinds of sensors by modification of their surface with sensitive layers. The absorption or binding of sensing components causes an increase of the mass load on QCM that finally is detected as a frequency shift of the crystal resonance. An increase in the frequency and, thus, the increase in mass sensitivity [4], is limited by manufacturing, as this would require thinner and more fragile substrates. Typically, frequencies of QCMs main harmonic are between 10 and 50MHz. The utilization of overtone harmonics or mesa structures can give an access to higher frequencies of QCMs. A disadvantage of QCMs sensor approach is a limited ability of the sensor to be integrated in planar platforms such as Lab on a Chip devices, where liquid detection, manipulation and separation are performed within single planar chip.

Another type of microacoustic sensors is based on surface acoustic wave (SAW) devices. Currently exist numerous approaches of application of SAW devices for liquid properties analysis [5–9]. The basic concept of a SAW sensor utilizes an interrogation of external measuring substance with propagating along the waveguide acoustic wave. Initially developed Rayleigh wave SAW sensors were applied for the organic gas detection utilizing polymer sensitive layers [10]. However, an application of the same approach for liquid sensors was associated with a considerable wave attenuation caused by irradiation of normal component of Rayleigh wave into the liquid volume.

Further development of SAW devices discovered a various modes of surface acoustic waves such as horizontally polarized shear waves that were applied for non-polar liquids measurements. Unfortunately, the wave attenuation was still too high because of a significant mismatch of dielectric properties of substrate (commonly used quartz substrates) and liquid. As a result, the wave confinement at the waveguide surface was deteriorated. The current problem was later solved by utilization of substrate materials with dielectric constant that is considerably higher than quartz [11,12]. The application of lithium niobate and lithium tantalite substrates of different cuts allowed the sensor to

operate with high permittivity liquids even in cases where it is directly applied to the waveguide surface. Thus, the SAW sensor based on 36˚ YX cut of $LiTaO_3$ wafer was utilized as a biosensor to detect amounts of an enzyme immobilized on a surface during the catalytic reaction [13].

Later, another type of shear horizontal SAW liquid sensors was developed with the use of Love surface wave. The Love wave is a surface acoustic wave that is localized within the overlayer deposited atop of the SAW waveguide. This type of wave appears in a layered structure and localizes in the overlayer because of its low acoustic wave velocity in comparison to the waveguide. Such acoustic wave localization allows decreasing the surface wave attenuation caused by scattering into the bulk of the substrate. The adjustment of the waveguiding layer thickness may create an acoustic film resonance that significantly improves the sensor sensitivity to mass loading [14].

Various dielectric materials such as silicon dioxide (SiO2) and silicon nitride (Si3N4) can be utilized as a waveguiding layer of Love wave sensor device [15,16]. The silicon dioxide is a relatively dense material with a high shear acoustic velocity. A significant advantage of silica layers is the exhibition of low acoustic losses for frequencies in the MHz range due to the elastic and amorphous nature of the material. Nevertheless, the issue of applying silicon oxide as the waveguide layer is its relatively high speed of sound which is nearly matches to the speed of sound of the piezoelectric substrate. In [17] it was shown that for the SAW sensor with the wavelength of 40μm, the maximum sensitivity can be reached with the waveguiding layer thickness in a range of $3.5 - 6.5$ μm. A deposition of silicon dioxide layers with the thickness more than a micrometer is in most cases associated with necessity to control inducing within the layer high mechanical stress that makes its manufacturing rather complicated.

The Love wave based sensor can be performed also using polymer layers. Poly(methyl methacrylate) (PMMA) [18,19] and SU-8 [20,21] are the polymers that have been intensively used in recent years. They can be applied directly in a photolithographic process and structured as the waveguiding layer [22]. Polymers have an advantage over solid state waveguide materials for the Love wave sensor implementation because of their relatively low shear wave velocity and simplified fabrication. However, due to their viscoelasticity, the crosslinking management or additional curing is necessary in order to avoid acoustic wave attenuation within the layer.

In order to apply the described sensors for a selective detection, the sensing area should be chemically tailored to attract selectively specific components of the analyzed liquid [23]. Most of the methods are based on organic chemistry to form tailored surface for the selective absorption of chosen liquid components. The application of the sensor for a bio liquids analysis requires the application of biospecific layers corresponding to detected analyte. In this case, the sensor binds the target constitute of the liquid, that changes the acoustic properties at the surface of SAW device (resonator or delay line, depending on sensor design) . The immobilization chemistry depends on the initial sensor design and the targeting analyte. The clear quartz surface or silica layer can be used for immobilization of silanes, whereas the functionalized thiols are utilized atop of gold surfaces in most cases. These immobilized layers provide specific active groups at the sensor surface to bind the analyte specific molecules. The first immunosensors utilized immobilized anti- immunoglobulin on a surface of quartz [24] and immobilized on $LiTaO_3$ antiglucose oxidase [22]. The Love wave sensor devices performed with PMMA waveguide and absorbed immunoglobulin into the waveguide layer were performed to detect anti- immunoglobulin and protein A, [25]. The application of the same PMMA layer covered with thin gold film with absorbed protein A as a capture molecule was used to detect to immunoglobulin [26]. A variety of binding schemes with immobilized protein A and protein G on a gold surface utilizing different substrates were investigated in [27–29] enabling oriented immobilization of antibodies. The same approach of analyte-specific immobilized layers based on lipide bilayers and fullerenes were utilized within SAW Love wave concept for antibodies detection [30,31]. Immobilized layers approach was successfully applied for detection of DNA [32], bacteria (such as Escherichia coli, Bacillus thuringiensis, Legionella and etc) [33], as enzyme sensor [34], the sensor for the detection of pesticides [35], sensor for the detection of cocain metabolite in vapor [36] and many other applications. The difficulty of recognition layers approach is in a necessity to avoid unspecific bindings on the sensor surface that causes a sensor measurement error. To overcome that problem, the application of intermediate hydrogel layers was introduced as one of the possible solutions towards reduction of unspecific bindings [37,38].

1.2. Sensors based on ultrasonic velocimetry

Methods of velocimetry are based on measurements of velocity of ultrasonic waves propagating through the analyzed solution. The propagation of ultrasonic waves interacting with the analyte is associated with their attenuation, scattering, absorption refraction or reflection that along with measurements of speed of sound of different wave types provide most complete information about analyzed solution. The main purpose of measurements of complex parameters of wave propagation is the evaluation of elastic properties of the probing solution. Currently developed sensor platforms that use the method, demonstrate a considerably high resolution with respect to speed of sound (up to 0.1 m/s and lower). One of the significant advantages of the method is an ability to gain the information from intermolecular interactions of liquid mixtures. The reaction on molecule interactions is reflected as a change in liquid compressibility that can be detected by probing the analyte with ultrasonic waves. Measurements of sound velocity at certain range of pressures can allow to evaluate thermodynamic quantities of the liquid analyte. The intermolecular forces that can be estimated from the compressibility data determine thermodynamic parameters of the analyzed solution. Considering a homogenous isotropic liquid, prime parameters that describe its elastic properties are isentropic (or adiabatic) β_S and isothermal β_T compressibility. The relation between isentropic compressibility and speed of sound can be presented in a following way: $\beta_S = 1/\rho U^2$ and $\beta_T = \beta_S + k^2 T/\rho C_p$ where ρ is an analyte density, k is coefficient of thermal expansion and C_p is heat capacity.

The most advantageous feature of the ultrasonic velocimetry method is an ability to observe the molecular processes by ultrasonic measurements. These processes involve changes in interaction of some functional groups. Thereby, the difference between measured and adiabatic compressibility provides an excess compressibility that reflects the interaction between mixture constituents. The sign of excess compressibility shows strength of intermolecular interactions in current liquid mixture. For binary mixtures, a negative access compressibility defines preliminary attractive intermolecular interactions. On the other hand, the positive excess compressibility advocates to an establishment of a less "rigid" molecular structure [39,40]. The investigation of the excess compressibility or excess thermodynamic properties of liquid mixtures in general, is a widely used approach that allows obtaining information from intermolecular interactions in multicomponent liquid systems.

Taking an advantage of intermolecular interaction sensing, the processes of binding of ligands by proteins, antigen – antibody interaction, binding of cations by polynucleotides and many others can be examined with ultrasonic velocimetry method. In [41] was demonstrated an example of solubilisation of fatty acid by micellar solution of sodium deoxycholate where dehydrating of fatty acid in the interior of micelle makes a significant contribution in ultrasonic velocity of that solution. The quantitative analysis of processes of intermolecular interactions requires a separate consideration of different reaction contributions. Along with variation of sound velocity, the change in solution relaxation should be taken into account. The complex analysis with ultrasonic measurements allows obtaining the information about binding constants, hydrational effect and other relevant information.

Promising application of ultrasonic velocimetry was discovered with respect to molecular mechanisms of proteins functioning [42,43]. It was found that conformational dynamics and volume fluctuations, that initially related to the isothermal compressibility of globular protein, contribute in relaxation of ultrasonic velocity. The effect can be observed by measuring the sound absorption during the processes in macromolecules [44,45].

A sensitivity of ultrasonic velocimetry to solute-solvent interactions opens a possibility to analyze various biological analytes. Currently the method is widely applied for various applications, such as immunoenzyme analysis [46], control of the blood clotting [47], analyze concentration and properties of blood cells [48]. Moreover it assists in medical applications allowing to conduct the analysis for detection of cancer cells [49], diagnosis of gastritis [50] and many other application. The method is widely used in various analytic systems for food industry, for example as a fat concentration detector in milk containing products.

The ultrasonic velocimetry approach is a powerful tool that has a broad variety of applications. However, nowadays demands require further sensor miniaturization and ability to be integrated in a multifunctional platform on a single chip. That makes it necessary to develop novel sensor platforms that allow to reach requirements and, at the same time, to maintain all advantages of already developed concept. One of the obvious approaches is combination of microacoustic and ultrasonic velocimetry sensor approaches. Velocimetry methods afford to keep advantages of liquids volumetric

properties analysis, when the microacoustic sensor concept satisfies the miniaturization and single chip integration demands.

In current work is proposed a sensor solution that utilizes SAW devices platform for acoustic wave excitation and detection. The sensor part is based on principles of ultrasonic velocimetry concept that is performed as periodical liquid filled microfluidic arrangement. Such periodical structure, also known as phononic crystal, includes liquid volumes as structure constitutes. The variation of volumetric material properties of phononic structure constitutes causes a change in acoustic properties of the whole arrangement that is proposed as a basic sensor principle.

1.3. Phononic crystal sensor approach

Periodical structures have attracted a great attention since the development of a theory of the electronic band theory for solid materials. Similar to periodic potential of the crystal lattice, composite materials with periodic spatial modulation of the dielectric properties on the scale of the optical wavelength, so-called photonic crystals, were introduced several decades ago. An arrangement of scattering centers with dielectric properties that are different to a homogeneous matrix surrounding the scatters is a representation of a typical photonic structure. Due to destructive interference of multiple scattered waves, these structures are featured by regions of wave lengths within which, incident electromagnetic waves cannot propagate through the structure. These ranges of wavelengths with respective frequencies are called the photonic band gaps[51].

In comparison to propagation of transversal electromagnetic waves through the photonic structure, the propagation of acoustic waves in solid periodic composite materials is featured by much richer and at the same time more complicated behavior that is defined by a simultaneous propagation of transversal and longitudinal components of an incident acoustic wave. As an equivalent of photonic crystals, acoustic periodic composite materials with a spatial modulation of elasticity, a mass density and longitudinal and transverse velocities of elastic waves were called Phononic Crystals (PnC). Similarly, as it was demonstrated for electromagnetic waves, the destructive / constructive interference of elastic waves in phononic structures exhibits band gaps in a certain wavelength regions [52,53].

The existence of a band gap in a certain wavelength range can be advocated in the same way as it was originally shown for electron spectrum in a solid material. The band gap can be considered as a region of a very low density of states for the propagation of acoustic waves through the structure with periodical variation of mechanical properties of a medium.

By analogy with solid materials, the acoustic wave propagation behavior in phononic structures can be described by the Bloch's theorem as a wave function in a periodical environment 1.1.

$$\psi(r) = e^{ikr}u(r) \qquad\qquad \textbf{1.1}$$

where r is position, ψ is the Bloch wave, u is a periodic function with the same periodicity as the crystal, k is a vector of real numbers called the crystal wave vector.

Rewriting the same Bloch's theorem for the mechanical displacement provides the following relation

$$u(r) = e^{ikr}u_k \qquad\qquad \textbf{1.2}$$

where u_k is a periodic function with the same periodic structure as mechanical properties of a propagating medium. Placing Fourier series of these periodical functions in the motion equation for an elastic wave in the isotropic body, equation for eigenvalues can be achieved and solved numerically.

1.3.1. Application of phononic crystals for liquid sensor purposes

An application of phononic structures for sensor purposes has several advantages depending on the sensor design. Considering the resonator sensor approaches, the most important performance parameter is a quality factor that is directly related to a sensitivity. It is preferred to have a high quality factor resonance with the frequency dependent on the liquid properties. The application of periodical structures with symmetry reduction allows obtaining a sensor response with separated narrow transmission bands. The disruption of a periodicity with structure defects (such as resonant cavities) causes a local change in state densities for propagating through the structure elastic waves. Constituting the defect with material of interest, the structure defect mode will respond on analyte material properties.

The approach of utilization of the defect mode for sensor purposes was in details described in [54]. It was shown that an introduction of symmetry reduction by altering the mechanical properties of one of scatters causes a disruption of the bandgap and supports the appearance of a narrow transmission window within the bandgap. The application of the analyzed liquid as one of the constitutes of periodical arrangement showed the structure response on volumetric material properties of that liquid. The velocity of sound was found to be one of the major influencing parameters on the position of the defect bands [54–60]. As it was previously described, speed of sound is one of the prime informative parameters analyzed in ultrasonic velocimetry methods. It serves as an integral measure that depends on thermodynamic values of liquids and liquid mixtures that is originally influenced by intermolecular interactions [61,62]. The variation of speed of sound can appear in a much broader range than the variation of other material properties like refractive index, that is used in many optical sensors including photonic crystal sensors.

One of phononic crystal sensor approaches is utilizing resonant cavities that are filled with the analyte as a structure defect. That cavity disrupts the structure periodicity that supports the appearance of a narrow transmission window within the bandgap. The variation of the analyte causes a change of speed of sound of the cavity constitutes. That change influences the cavity response that provides the information about analyzed solution. In this case, the sensor concept can utilize the determination of the transmission maximum frequency that should be completed with a high accuracy. The limiting factor is the peak half bandwidth. Simultaneously, the defect peak should be well separated by the bandgap.

1.3.2. Millimetre wavelength scale phononic crystal sensor realisation

The basic concept of phononic crystal liquid sensor can be exemplified with a millimeter scale arrangement utilizing a cavity mode [56]. The sensor was used for an in-line gasoline analysis in a megahertz frequency range[58,59] that corresponds to a millimeter acoustics wavelength region. It consists of two dimensional arrangement of scatters performed as an array of periodically placed cylindrical holes with a slit cavity in between. The slit cavity acts as an element of symmetry disruption by means of geometry change and as a resonant volume. Analyzed liquid was filling the defect as

well as the structure scatters. The displacement pattern and pressure distribution of the described structure are shown in Figure 1.1. It demonstrates the transmission through the structure at the cavity resonance frequency.
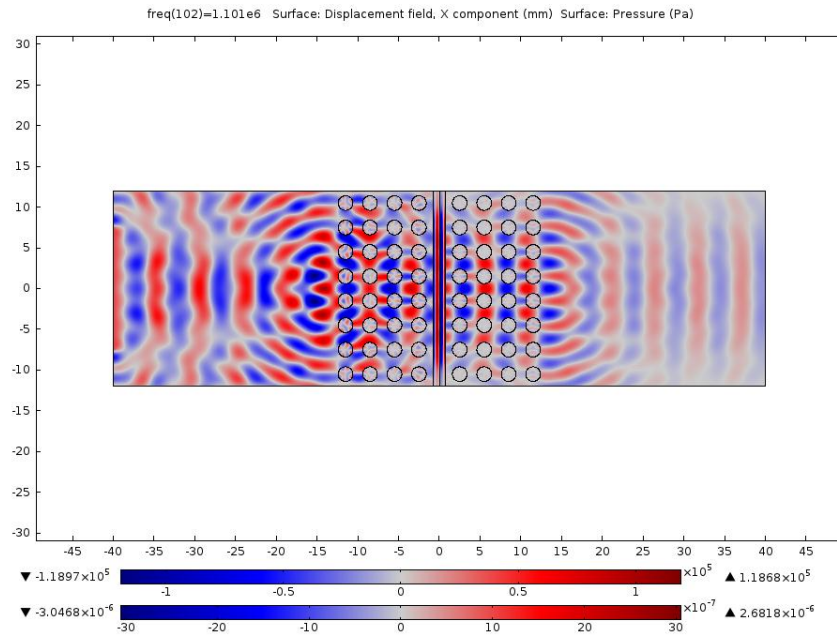
Figure 1.1 Simulation of displacement and pressure distribution for two dimensional phononic structures with the resonant cavity.

The simulation has been performed for the structure filled with liquid of 750 kg/m^3 density and speed of sound of 1100 m/s that correspond to known data for the low temperature gasoline fraction. Experimental investigations were performed with the sensor structure shown in Figure 1.2.
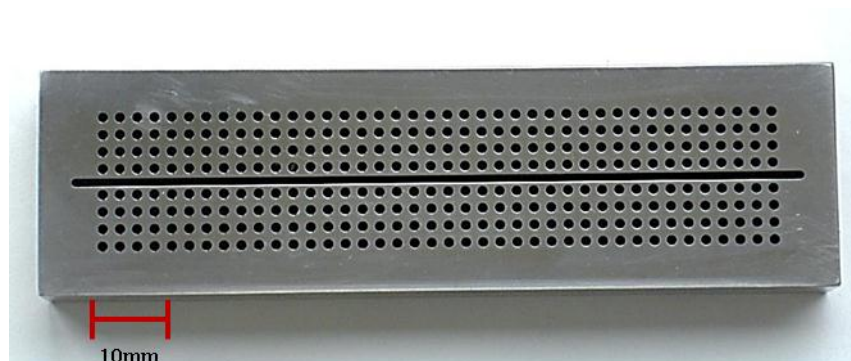
Figure 1.2 Two dimensional phononic crystal sensor completed as an array of periodically placed holes with a slit resonance cavity [59].

The transmission spectrum of the structure was obtained with the use of external contact ultrasonic transducers that were acoustically coupled to the structure with intermediate coupling agent.

The measuring scheme was completed as a two-port device. The transmission was obtained from S_{21} parameter measurement with a network analyzer. The experimental setup is demonstrated in Figure 1.3.
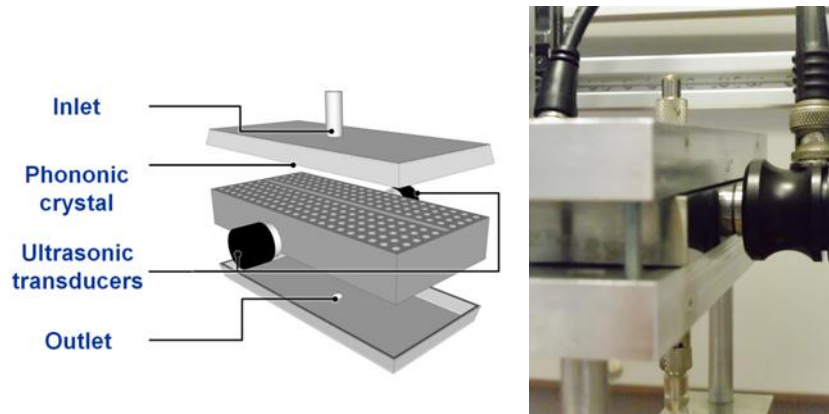
Figure 1.3 Experimental setup for two dimensional phononic crystals with a slit cavity [59]

Measured magnitude response of S_{21}-parameter that was recalculated in transmission spectrum is demonstrated in Figure 1.4.
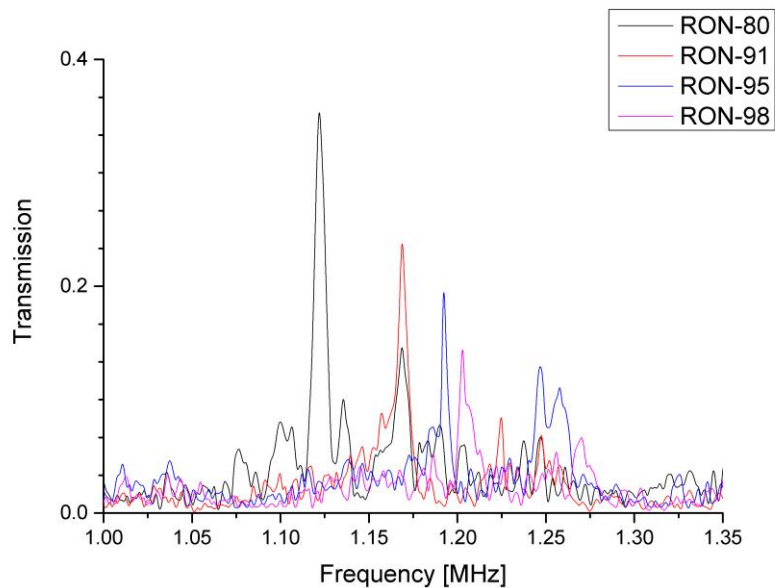
Figure 1.4 Transmission spectrum through the phononic crystal sensor filled with different gasoline samples. (RON – research octane number).

The transmission spectra of the phononic crystal sensor filled with different octane number gasoline blends demonstrates a distinctive sensor response. Each transmission spectrum shows a well distinguishable transmission peak that corresponds to a slit cavity resonance with amplitude considerably above the noise floor.

This periodical arrangement of millimeter wavelength range, vividly exemplifies the features of application of phononic structures for sensor purposes. The ability to exhibit the isolated resonance is very important for obtaining a distinctive sensor response. The arrangement responds to liquid material volumetric properties, such as speed of sound, that makes this concept compatible with ultrasonic velocimetry approach. However, in order to replicate the demonstrated phononic crystal sensor concept in a micrometer wavelength region and have a possibility to utilize it as an integrated part of a single chip device, the acoustic wave excitation and detection should be changed to an appropriate approach.

1.3.3. SAW platform for phononic crystal sensor realisation

In a micrometer wavelength range, more specifically the frequency range from 100 MHz till several GHz, surface acoustic waves (SAW) devices is a widely applied platform. SAW devices have attracted a great attention since 1970s because of a number of advantages that allowed achieving extremely compact high frequency devices. For decades, they have been utilized in a great diversity of devices and applications as functional elements such as resonators, filters, sensors and actuators. Surface acoustic wave devices became irreplaceable for telecommunication industry where their advantages are obvious. Small dimensions, high long term stability, in some cases even temperature irrelevance, pave the way for these devices to a broad variety of applications.

With respect to the sensor application, the SAW platform has a number of advantages that provide a possibility for the excitation of different types of waves by specification of a certain substrate cut, application of a certain IDT's design or utilization of the layered structures. In spite of the fact that SAW devices are already well developed, the state of development of SAW based phononic structures is still in the early stages.

Initially the research works demonstrating the bandgaps for surface acoustic waves in the millimeter wavelength scale were published in late 90th. In [63], the localization in

two dimensional arrangement of surface acoustic waves were studied theoretically with considerations of anisotropic properties of a host material. A subsequent theoretical work in this field demonstrated spatial and frequency distributions of bandgaps for surface and bulk acoustic waves in 2D phononic structures [64]. A theory for two-dimensional phononic structures that consist of a material with anisotropy was reported in [65]. Presented surface wave dispersion relations were derived with a plane wave expansion method. Theoretical results regarding bandgaps characteristics were presented for two-dimensional phononic structures with square and hexagonal lattices for different anisotropic host materials. Bandgap properties for surface acoustic waves of a periodical 2D arrangement that was made of piezoelectric material confined in isotropic body were studied in [66]. Reports on bandgap appearance independent of surface acoustic wave polarization and the surface modes were described in [67]. Theoretically investigated Y-cut lithium niobate based structure was completed as an array of periodically placed cylindrical scatters (holes). Particularly, the propagation and localization of Rayleigh waves in disordered piezoelectric phononic crystals were theoretically studied and reported in [68].

During the last decade, were published the reports on micrometer wavelength scale studies of periodical phononic structures that are mostly applicable for radio frequency communication devices. Unique properties of phononic structures, such as an ability to exhibit bandgaps in certain predefined by structure design frequency range, made them attractive for surface acoustic wave devices (such as filters, resonators etc.) application. Wu et al. [69] reported on a silicon based phononic structure fabricated under standard MEMS technology as well as acoustic wave excitation and detection with a help of piezoelectric ZnO layer with a system of slanted IDTs. PnC structure scatters are performed as an air filled holes with a square lattice. The experimental confirmation of existence of the complete bandgap for surface acoustic waves was demonstrated later by Benchabane et al. [70]. The square-lattice two-dimensional phononic structure was directly etched in lithium niobate waveguide. In this case, surface acoustic waves were excited with standard IDTs. The complete bandgap was experimentally found at frequency around 200 MHz. Afterwards, scattering and propagation of surface acoustic waves through the square-lattice phononic structure was experimentally investigated with optical methods in [71,72]. The bandgap properties of investigated 2D arrangement were vividly demonstrated as measured wave fields at different

frequencies. Considering the phononic structures as an efficient acoustic wave reflector, the two-port SAW devices were combined with phononic reflective gratings [73]. The experimental structure was completed as layered ZnO/Si SAW device with a square lattice phononic structure performed as an array of cylindrical scatters (holes) in a silicon waveguide. The achieved results demonstrated that phononic structures can act as an efficient acoustic wave reflector with significantly reduced number of lattice periods in comparison to the conventional metal reflective gratings.

The described above SAW based phononic crystal approaches are currently the state of the art in terms of liquid sensors application. Most of the works show that the efficiency of phononic structures built on a basis of SAW devices is associated with several challenges (wave scattering losses, mode conversions and etc.) that can considerably deteriorate the sensor performance. In order to minimize the acoustic wave dissipation and improve the sensitivity, designs of SAW based phononic structures have to be reconsidered in order to be efficiently applied for sensor purposes.

2 BACKGROUND

The subject of current work is directly related to problems of propagation of elastic waves in anisotropic as well as isotropic solid materials. In order to describe the distribution of mechanical deformations in isotropic and anisotropic solids, it is necessary to introduce governing equations that are subsequently applied for solving numerical problems for each of simulating domain. Depending on properties of perturbed medium, the introduced mechanical deformations can initiate appearance of propagating elastic waves or additionally, the coupling of mechanical stress into a surface charge (in case of piezoelectric materials). The combination of isotropic and anisotropic mediums within a single simulation model requires separation of the simulating geometry into domains, where each of them is described with certain set of equations. In following chapter, are introduced analytical relations that compile the developed numerical simulation model and performed in a subsequent chapter theoretical analysis.

2.1. Elastic waves – main definitions

During the propagation of elastic waves in an infinite isotropic solid body, the direction of a single particles displacement can be rather coincidental or perpendicular regarding direction of the wave propagation. Each of these wave modes has its own speed of propagation (speed of sound of certain wave mode) that is dependent on material elastic properties. If a solid body is featured by interfaces in a direction of the wave propagation, it opens a possibility for existence of other wave modes.

Elasticity is defined by internal forces that are initiated inside of the solid body when it is moved from a balanced state. When the solid body is not disturbed by any forces acting upon it, each single particle of the body remains in the equilibrium state that can be defined in a system of Cartesian coordinates as (x_1, x_2, x_3). The propagation of acoustic wave through such solid body, initiates the displacement of each point of this body from its balanced state. The vector of displacement that defines a deviation of each of these points from its balanced state can be defined as u_1, u_2, u_3, where each of them is dependent on time and coordinate of the points x_1, x_2, x_3 respectively. In such manner, the deformation of the elementary volume can be represented as a symmetrical tensor of the deformation:

$$S_{ij}(x_1, x_2, x_3) = \frac{1}{2}\left(\frac{\partial u_i}{\partial x_j} + \frac{\partial u_j}{\partial x_i}\right)$$

2.1

i, j = 1, 2, 3 are indexes of three dimensional system of coordinates

Due to any rotation or displacement of a whole body that does not initiate deformations, a tensor of deformations S_{ij} is a symmetrical tensor of second order.

Internal forces of a solid body are described by the mechanical strain tensor T_{ij}. The mechanical strain for elastic materials is proportional to deformation within a defined deformations range. In general, one dimensional case is described by Hooke's law. The coefficient of proportionality can be defined as a fourth order tensor of elastic modules c_{ijkl}.

$$T_{ij} = \sum_k \sum_i c_{ijkl} s_{kl}, \quad i, j, k, l = 1, 2, 3.$$

2.2

In case of dependence of the strain and the deformation on time and coordinates, an application of Newton's law provides a possibility to get a motion equation.

Let's consider an infinitely small cubic volume in a solid state body where all the forces acting upon it can be presented as a set of orthogonal forces. Ridges of the cube are parallel to x_1, x_2, x_3 coordinates and have a length δ. If we sum all the force projections, the resulting force can be presented as

$$\delta^s \left[\sum_i \frac{\partial T_{ij}}{\partial x_j}\right]$$

2.3

Considering a second Newton's law, this force should be equal to the acceleration that can be presented as a second derivative of the displacement d^2u_i/dt^2 multiplied by mass $\rho\delta^3$, where ρ is a mass density. That provides the equation of motion for elastic wave in a solid body:

$$\rho\frac{\partial^2 u_i}{\partial t^2} = \sum_j \frac{\partial T_{ij}}{\partial x_j}, i,j = 1,2,3.$$

$$2.4$$

The same equation can be written omitting the summing symbol due to the summation of the repeatable index j that is already implicated

$$\rho\frac{\partial^2 u_i}{\partial t^2} = \frac{\partial T_{ij}}{\partial x_j}$$

$$2.5$$

2.2. Governing equations for piezoelectric materials

There is a separate class of materials, the internal structure of which exhibits an absence of a symmetry center, where their deformation initiates a proportional electrical polarization. Contrariwise, the electrical field that is applied to the surface creates deformations proportional to its intensity, called piezoelectric materials. The piezoelectric effect is a feature of some anisotropic materials, where elastic deformations and strain are related to the electrical field intensity and the dielectric displacement.

In current work the excitation and detection of acoustic waves are performed utilizing conventional SAW piezoelectric substrates such as quartz and lithium niobate. Numerical simulation that performed within the framework of this contribution include the analysis of piezoelectric domains. In comparison to elastic waves in isotropic medium, the propagation of elastic deformations in piezoelectric materials have more complex analytical description, because of the fact, that the equations for elastic wave have to be solved together with Maxwell equations.

In each point of such piezoelectric material, a mechanical strain tensor T_{ij} is dependent on a tensor of deformations S_{ij} and also on intensity of electrical field E. Relations describe associations between elastic properties of the piezoelectric material $T_{ij} = c_{ijkl}S_{kl}$ and its behavior in the electromagnetic field $D_i = \varepsilon_{ij}E_j$ can be represented as a following system of equations

$$T_{ij} = c^E_{ijkl}S_{kl} - e_{kij}E_k,$$

$$D_i = \varepsilon^S_{ij}E_j + e_{ijk}S_{jk} \qquad \textbf{2.6}$$

where the upper index of elastic constants c^E_{ijkl} demonstrates that they are taken at constant electrical field E and the upper index of tensor of dielectric constants ε^S_{ij} demonstrates that they are measured at the certain deformation. The tensor e_{ijk} that binds the elastic deformation with the electrical field is called a piezoelectric tensor.

Therefore, the propagation of elastic waves in the piezoelectric material is described by the equation describing mechanical displacements 2.5 and Maxwell's equations that are connected by the system of equations presented above 2.6.

The propagation of elastic waves is much slower than electromagnetic waves; therefore, in current case, the electrical field can be presented as a gradient of a scalar potential.

$$E_i = -\frac{\partial \varphi}{\partial x_i} \qquad \textbf{2.7}$$

By combining the equation defining deformation 2.1 and equation describing mechanical displacements 2.5 as well as relations 2.6 and Maxwell's equation $\nabla D = 0$ with consideration of electrical field presented through the gradient of the scalar potential 2.7, following equations that describe the propagation of elastic waves in a piezoelectric material can be achieved:

$$\rho \frac{\partial^2 u_j}{\partial t^2} = c_{ijkl}\frac{\partial^2 u_k}{\partial x_i \partial x_l} + e_{kij}\frac{\partial^2 \varphi}{\partial x_i \partial x_k}$$

$$e_{ikl}\frac{\partial^2 u_k}{\partial x_i \partial x_l} - \varepsilon_{ik}\frac{\partial^2 \varphi}{\partial x_i \partial x_k} = 0 \qquad \textbf{2.8}$$

These equations bring together projections of displacement u and the scalar potential of electric field φ.

In accordance with initial and boundary conditions, these equations completely describe possible wave processes in a volume of the elastic anisotropic solid body with piezoelectric properties.

2.3. Acoustic waves in isotropic materials

As it was mentioned in previous chapters, the structure that will be numerically simulated in subsequent chapters includes isotropic and anisotropic materials. Isotropic model domains are described with linear elastic model. Anisotropic domains are described with piezoelectric material model. A analytical description of propagation of acoustic waves in anisotropic materials is rather complicated with solutions mostly obtained by applying numerical methods; equations for wave propagation in isotropic materials on the other hand, describe the linear elastic part of the model and provide a necessary background for description of wave propagation in anisotropic domains.

The elastic tensor of the isotropic material obtains only two independent components

$$c_{ijkl} = \lambda \delta_{ij} \delta_{kl} + \mu (\delta_{jk} \delta_{jl} + \delta_{il} \delta_{jk}) \qquad \textbf{2.9}$$

where δ_{ij} is Kronecker delta that has two values depending on its indexes

$$\delta_{ij} = \begin{cases} 0 & if\ i \neq j, \\ 1 & if\ i = j. \end{cases} \qquad \textbf{2.10}$$

Constants λ and μ are Lamé parameters, two material-dependent quantities from strain-stress relations.

From 2.9

$$c_{ijkl} = \lambda \delta_{ij} \delta_{kl} + \mu (\delta_{jk} \delta_{jl} + \delta_{il} \delta_{jk}) \qquad \textbf{2.9}$$

it is seen that:

$c_{11} = c_{22} = c_{33} = (\lambda + \mu)$

$c_{12} = c_{13} = c_{23} = c_{21} = c_{31} = c_{32} = \lambda$

$c_{44} = c_{55} = c_{66} = (c_{11} - c_{12})/2 = \mu$

So, all none-diagonal components are zero.

Placing described elastic tensor of isotropic material c_{ijkl} to the mechanical strain for the isotropic material equation 2.2 brings following:

$$T_{ij} = \lambda \delta_{ij} \sum_i \frac{\partial u_i}{\partial x_j} + 2\mu S_{ij}$$

2.11

The motion equation for elastic waves in isotropic material 2.12 is provided by placement of described equation for mechanical strain in the isotropic material into the equation of motion for the elastic wave in a solid body 2.4.

$$\rho \frac{\partial^2 u_j}{\partial t^2} = (\lambda + \mu) \frac{\partial}{\partial x_j} \sum_i \frac{\partial u_i}{\partial x_i} + \mu \sum_i \frac{\partial^2 u_j}{\partial x_i^2}$$

2.12

2.4. Plane waves in infinite isotropic elastic body

In order to obtain a solution for more specific Rayleigh wave, that is utilized in current work for structure excitation, the solutions for motion equations for a plane wave in the infinite isotropic elastic body have to be introduced first. The plane wave is a partial solution of the wave equation and is a convenient model for obtaining wave equation solutions despite the fact that it does not exist within finite dimensions.

According to equation 2.12, the isotropic elastic body supports a propagation of the plane wave. In this case, a vector of displacement can be presented as

$$\vec{u} = \vec{u_0} exp[j(\omega t - \vec{k}\vec{x})]$$

2.13

where $\vec{u_0}$ is a vector constant that is irrelevant to coordinate and time.

By placement of displacement vector 2.13 in the motion equation for elastic wave 2.12, the following relation can be obtained

$$\omega^2 \rho u_j = (\lambda + \mu)(\vec{k}\vec{u_0})k_j + \mu|\vec{k}|^2 u_j; j = 1, 2, 3,$$

2.14

Where $|\vec{k}|^2 = k_1^2 + k_2^2 + k_3^2$

defining projection components of displacement according **2.13**, the introduced equation 2.14 can be presented as:

$$\omega^2 \rho \vec{u_o} = (\lambda + \mu)(\vec{k}\vec{u_0})\vec{k} + \mu|\vec{k}|^2 \vec{u_0}$$

2.15

Two types of solutions for the plane wave are satisfying the vector equation 2.15

First solution introduces the transverse wave. In this case, a wave vector is

$$\left|\vec{k_t}\right|^2 = \omega^2 \rho / \mu \qquad\qquad \textbf{2.16}$$

and a phase speed is

$$V_t = \sqrt{\mu/\rho} \qquad\qquad \textbf{2.17}$$

As it seen, a phase speed does not have a frequency dependence; in other words, a non-dispersive. The vector of displacement $\vec{u_o}$ can have any direction in a plane of the wave front normal to $\vec{k}$.

Another solution is presented as a longitudinal wave. The wave vector can be described by following:

$$\left|\vec{k_l}\right|^2 = \omega^2 \rho / (\lambda + 2\mu) \qquad\qquad \textbf{2.18}$$

where the phase speed is

$$V_l = \sqrt{(\lambda + 2\mu)/\rho} \qquad\qquad \textbf{2.19}$$

That also does not depend on frequency; therefore, it is the non-dispersive as well. The vector of displacement $\vec{u_o}$ is parallel to direction of wave vector $\vec{k}$.

Due to always positive Lamé parameters, the speed of sound for longitudinal waves is always larger than speed of sound for transversal waves.

2.5. Rayleigh waves in isotropic half space

Predicted in 1885 by Lord Rayleigh a type of acoustic waves is capable to propagate along free surface of the solid body, later became one of the most convenient type of waves for surface acoustic wave devices (SAWs). This is the type of the wave that is used in current sensor design. Despite the fact that direct application of Rayleigh wave SAW devices for liquid sensor purposes suffers from strong wave attenuation caused by the liquid, it is applied in current sensor design. The irradiation of normal component of Rayleigh wave is disadvantageous in case of direct contact of analyte with the wave propagation surface. But in current case it performs the excitation of the structure that contains the liquid analyte enclosed in microfluidic channels and is isolated from the waveguide. The structure itself is placed directly above the SAW waveguide. The normal component of Rayleigh wave assist efficient wave – structure coupling.

In isotropic solids, these types of waves cause a single surface particles movement in ellipses orthogonal to the surface along the direction of the propagation. The maximum of the displacement amplitude for Rayleigh waves is reached on a free surface of propagation medium and exponentially decays with increasing of a distance from the surface. Due to that, most of mechanical energy is concentrated in a surface layer with a thickness of the wave length. In case when a solid body has piezoelectric properties, propagating elastic waves generate the surface charge along the propagation path. This charge can be read with metal electrodes placed on the surface of piezoelectric material. This principle is applied in SAW devices where excitation and receiving of the acoustic waves is completed with a set of periodically placed metal stripes electrically connected in a certain manner, called interdigitated transducers (IDTs).

The Rayleigh wave is a surface type of a wave that exists at a boundary of a solid material / vacuum (air or any other gas). In order to obtain a solution for this kind of the wave, an isotropic media that is infinite in x_1 x_2 directions with solid / vacuum boundary at $x_3 = 0$ should be considered. The solid material is defined in a half space with $x_3 < 0$ and vacuum that is defined at $x_3 > 0$. The wave propagates in x_1 direction along a half space interface; a wave front is parallel to x_2 axis, Figure 2.1
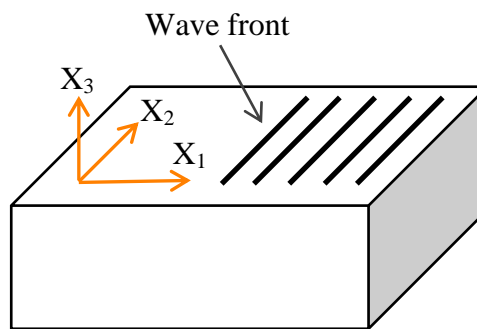
Figure 2.1 A wave is propagating in x_1 direction along the half space interface and the wave front

A solution has to satisfy the motion equation for elastic waves in the isotropic material (12) and boundary conditions according which, the absence of forces on a free surface at $x_3 = 0$ should be provided.

By application of the rule where a vector field can be presented as superposition of gradient and curl fields, a displacement field can be presented in a following way:

$$\vec{u} = \vec{u_l} + \vec{u_t} \qquad\qquad 2.20$$

Where $\vec{u_l}$ and $\vec{u_t}$ can be presented through scalar φ and vector $\vec{\psi}$ potentials by following

$$\vec{u_l} = grad\phi$$

$$\vec{u_t} = rot\vec{\psi} \qquad\qquad 2.21$$

In order to obtain the system of two independent equations 2.22 and 2.23, described component of the displacement field was placed in motion equation for elastic waves in isotropic material.

$$\rho\frac{\partial^2 u_{li}}{\partial t^2} - (\lambda + 2\mu)\sum_j \frac{\partial^2 u_{li}}{\partial x_j^2} = 0 \qquad\qquad 2.22$$

$$\rho\frac{\partial^2 u_{ti}}{\partial t^2} - \mu\sum_j \frac{\partial^2 u_{ti}}{\partial x_j^2} = 0 \qquad\qquad 2.23$$

Equation 2.22 describes a propagation of longitudinal waves whereas 2.23 describes transversal waves.

Due to the unchangeable Rayleigh wave in direction x_2, equations 2.22 and 2.23 for a harmonic wave without an influence from x_2 coordinate can be presented as:

$$\frac{\partial^2\phi}{\partial x_1^2} + \frac{\partial^2\phi}{\partial x_3^2} + k_t^2\phi = 0 \qquad\qquad 2.24$$

$$\frac{\partial^2\psi_2}{\partial x_1^2} + \frac{\partial^2\psi_2}{\partial x_3^2} + k_t^2\psi_2 = 0 \qquad\qquad 2.25$$

Where

$$k_l^2 = \frac{\omega^2\rho}{\mu}, \qquad k_t^2 = \omega^2(\lambda + 2\mu)/\rho \qquad\qquad 2.26$$

Or described through the phase speed of transversal and longitudinal wave

$$|k_t|^2 = \frac{\omega^2}{V_t^2}$$

$$|k_l|^2 = \omega^2/V_l^2 \qquad \textbf{2.27}$$

The equation 2.25 describes only a transversal component of the displacement field that is polarized in x_2 direction; due to that, only ψ_2 component of the vector potential is presented and two others are omitted.

The solution for scalar and vector potentials of the displacement field should be found in a following way:

$$\boldsymbol{\phi(k, x_1, x_3) = \phi_0(k, x_3)\exp(jkx_1 - \omega t)} \qquad \textbf{2.28}$$

$$\boldsymbol{\psi_2(k, x_1, x_3) = \psi_0(k, x_3)\exp(jkx_1 - \omega t)} \qquad \textbf{2.29}$$

Placing 2.28 and 2.29 in 2.24 and 2.25 respectively, two differential equations regarding $\phi_0(k, x_3)$ and $\psi_0(k, x_3)$ can be obtained with solutions as following:

$$\boldsymbol{\phi_0(k, x_3) = A_0\exp(-qx_3)} \qquad \textbf{2.30}$$

$$\boldsymbol{\psi_0(k, x_3) = B_0\exp(-sx_3)} \qquad \textbf{2.31}$$

Where $q = \pm\sqrt{k^2 - k_l^2}$; $s = \pm\sqrt{k^2 - k_t^2}$; A_0, B_0 are arbitrary constants.

From the physical background, solutions with an exponential decay in a depth field are meaningful. With respect to 2.30 and 2.31, solutions 2.28 and 2.29 can be presented as:

$$\boldsymbol{\phi(k, x_1, x_3) = A_0 \exp(-qx_3) \exp(jkx_1 - \omega t),} \qquad \textbf{2.32}$$

$$\boldsymbol{\psi_2(k, x_1, x_3) = B_0 \exp(-sx_3) \exp(jkx_1 - \omega t).} \qquad \textbf{2.33}$$

In order to define main characteristics of a wave such as speed of sound, the pattern of displacement and mechanical strain in x_3 direction, boundary conditions for strain tensor $T_{33} = 0$ and $T_{13} = 0$ to Hooke's law written in a form 2.11 should be applied. Consider solutions for scalar and vector potentials 2.32 and 2.33, we receive the system of two equations regarding constants A_0 and B_0:

$$\left[k\frac{\lambda}{2\mu} - q^2\left(1 + \frac{\lambda}{2\mu}\right)\right]A + iksB = 0, \qquad \textbf{2.34}$$

$$2ikqA + (k^2 + s^2)B = 0. \qquad \textbf{2.35}$$

A non-trivial solution for a presented system of equations exists under condition when the determinant equals zero. Such condition is sequent to following characteristic equation for the wave number determination:

$$4k^2qs - (k^2 + s^2)^2 = 0. \qquad \textbf{2.36}$$

This equation is called the Rayleigh wave equation.

Considering $\quad q = \pm\sqrt{k^2 - k_l^2}\,; \ s = \pm\sqrt{k^2 - k_t^2} \quad$ and $\quad |k_t|^2 = \omega^2/V_t^2$ $|k_l|^2 = \omega^2/V_l^2$ Rayleigh wave equation can be written through parameters of speed of sound as:

$$\left\{2 - \left(\frac{v_R}{v_t}\right)^2\right\}^2 = 4\left\{1 - \left(\frac{v_R}{v_t}\right)^2\right\}^{\frac{1}{2}}\left\{1 - \left(\frac{v_R}{v_t}\right)^2\right\}^{\frac{1}{2}} \qquad \textbf{2.37}$$

where v_R is a phase speed of propagating Rayleigh wave, v_t and v_l are speeds of transversal and longitudinal bulk waves in a solid material.

As a result of derivation should be noticed that, the speed of the surface acoustic wave is always slightly lower than speed of the transversal bulk wave. With knowledge of the phase speed of the Rayleigh wave, values of constants as well as scalar and vector potentials of the displacement field can be obtained from the system of equations 2.34, 2.35.

$$\phi(k, x_1, x_3) = A_0 \exp(-qx_3)\exp(jk_R x_1 - \omega t), \qquad \textbf{2.38}$$

$$\psi_2(k, x_1, x_3) = A_0 \frac{2ik_R q}{k_R^2 + s^2}\exp(-sx_3)\exp(jk_R x_1$$
$$- \omega t). \qquad \textbf{2.39}$$

Equations 2.38 and 2.39 demonstrate that Rayleigh wave consists of two waves, transversal and longitudinal, that propagate along the half space boundary (solid – vacuum interface) with the same speed and attenuate in depth by law

$$\phi(k, x_1, x_3) \sim \exp\left(-\sqrt{k_R^2 - k_l^2}\, x_3\right), \psi_2(k, x_1, x_3) \sim \exp\left(-\sqrt{k_R^2 - k_t^2}\, x_3\right). \quad \textbf{2.40}$$

At the boundary with $x_3 = 0$, these waves mutually compensate initiated strains. Components of displacement that are distinctive from zero can be found by adding equations 2.40 to 2.21.

Expressions for Rayleigh wave components of the displacement propagating in x_1 direction can be presented as:

$$u_1 = C[\exp(kb_1 x_3) - A\exp(kb_2 x_3)]\exp ik(x_1 - v_R t),$$

$$u_3 = -ikb_1 C[\exp(kb_1 x_3) - A^{-1}\exp(kb_2 x_3)]\exp ik(x_1 - v_R t)$$

$$\textbf{2.41}$$

Where $b_1 = \{1 - (v_R/v_l)^2\}^{\frac{1}{2}}, b_2 = \{1 - (v_R/v_l)^2\}^{\frac{1}{2}}$ and $A = (b_1/b_2)^{\frac{1}{2}}$ obtain positive real values, and C is an arbitrary constant dependent on the excitation level.

Longitudinal u_1 and vertical u_3 components of the displacement are shifted on $\pi/2$ for any value of x_3; therefore, particles undergo an elliptical motion with direction of the motion on a free surface opposite to direction of the wave propagation.

By analyzing amplitudes of the displacement of propagating surface acoustic wave that depend on the distance from a half space interface it will be found that the component of displacement u_3, that is orthogonal to the surface, increases at a relatively small depth and then rapidly decays and becomes almost negligible with depth around 2 - 2,5 of the wavelength. The component of displacement u_1 changes its sign at the depth of approximately 0,2 of the wave length and also decays almost completely at the depth of $2 - 2,5$ of the wave length.

The analytical solution for the Rayleigh wave provides necessary understanding regarding the excitation of liquid containing structure. The combination of transversal and longitudinal components presumably initiate various structure modes with efficient coupling. The more detailed description of excited with Rayleigh wave phononic structure will be provided in subsequent chapters.

2.6. Waves in anisotropic piezoelectric half space

The solution for the motion equation 2.8 in an infinite piezoelectric half space in comparison to the isotropic non-piezoelectric case is different due to necessity to introduce a surface potential that propagates along with the acoustic wave and also can be found as a plane wave of the form:

$$\vec{u} = \vec{u_0} exp\left[j(\omega t - \vec{k}\vec{x})\right], \qquad \textbf{2.42}$$

$$\Phi = \Phi_0 exp\left[j(\omega t - \vec{k}\vec{x})\right]. \qquad 2.43$$

Due to the wave propagation in the half space, certain boundary conditions have to be taken into account. In case of the anisotropic piezoelectric half space, boundary conditions can be separated as mechanical boundary conditions where normal components of mechanical strain tensor have to be zero $T_{13}=T_{23}=T_{33}=0$ at $x_3 = 0$.

Placing relations 2.42 2.43 in the motion equation for piezoelectric materials 2.8, the solution can be found as a combination of partial waves in a form of

$$\vec{u'} = \vec{u'_0} \exp(j\gamma x_3) \exp[j(\omega t - \beta x_1)],$$

$$\Phi' = \Phi'_0 \exp(j\gamma x_3) \exp[j(\omega t - \beta x_1)]. \qquad \textbf{2.44}$$

where γ is decay constant in direction x3 and β is a wave vector in x_1 direction.

In this case, solutions for partial waves can be found only numerically. The final solution for the wave propagation is a combination of partial waves

$$\vec{u} = \sum_{m=1}^{4} A_m \vec{u'_m};$$

$$\Phi = \sum_{m=1}^{4} A_m \Phi'_m. \qquad \textbf{2.45}$$

Values of A_m can be defined applying boundary conditions. The obtainment of analytical solutions for waves in anisotropic piezoelectric half space can be completed numerically. Further analytical description becomes rather complex because of the necessity to combine in a single theoretical model the anisotropic solid domains, isotropic solid domains and liquid domains. In order to achieve the most probable solutions, the theoretical structure description is reduced from this point to numerical

approach based on finite element analysis. Analytical relations that are introduced in previous chapters are applied for analytical description of separate domains within integrated multidomain simulation model.

2.7. Numerical simulation of SAW based devices with finite element analysis (FEM) software COMSOL Multiphysics

Widely utilized methods for analytical investigations of periodic structures, such as finite-difference time-domain method (FDTD), describe a behavior of phononic structures utilizing mostly infinite models that allow understanding the physics behind, but are not optimal for description of arrangements with finite dimensions. Also most of the works dealing with calculations of phononic structures with FDTD methods investigate a phononic structure behavior with a certain type of waves such as longitudinal of shear waves. In case where the theoretical investigations are focused on interrogation of periodic arrangements with surface acoustic waves, utilization of that simulation approach becomes rather complex considering variety of surface waves and their possible modes conversions.

On the other hand, finite element method (FEM) can serve as more appropriate tool for numerical simulation of finite structures. FEM is a numerical method of finding of the solutions for partial differential equations at certain boundary conditions. This method is widely utilized for a broad variety of simulation tasks in structural mechanics, heat transfer models, fluidics and electromagnetic problems. Nowadays, ANSYS and COMSOL^{TM} Multiphysics are the most advanced FEM simulation software tools. In order to choose the optimal simulation platform, the simulation problem should be specified in details.

The conventional waveguide materials applied for SAW devices are strongly anisotropic. The material cut, the direction of wave propagation, design of IDTs and their geometry and material properties should be defined according to manufactured SAW structures. Changes in substrate cut parameters or direction of wave propagation cause change of excited wave type. Therefore, the simulation platform has to provide an opportunity to describe anisotropic materials with possibility to specify a certain material cut. The simulation problem of SAW propagation is governed by differential equations that should be solved for certain geometry, material properties at certain cut

and boundary conditions. The relations between applied electric field, stress, strain and electric displacement are the mentioned above system of following equations:

$$T_{ij} = c_{ijkl}^E S_{kl} - e_{kij} E_k,$$

$$D_i = \varepsilon_{ij}^S E_j + e_{ijk} S_{jk} \qquad\qquad 2.6$$

Where T_{ij} represents a stress vector, $c^E{}_{ijkl}$ is the elasticity matrix, S_{kl} is the strain vector, e_{kij} is the strain vector, E_k is applied electric field, D_i is the electrical displacement and $\varepsilon^S{}_{ij}$ is the permittivity matrix.

Solving the Newton's and Maxwell equations related to demonstrated above system of equations provides the electric potential φ as a result:

$$\rho \frac{\partial^2 u_j}{\partial t^2} = c_{ijkl} \frac{\partial^2 u_k}{\partial x_i \partial x_l} + e_{kij} \frac{\partial^2 \varphi}{\partial x_i \partial x_k}$$

$$e_{ikl} \frac{\partial^2 u_k}{\partial x_i \partial x_l} - \varepsilon_{ik} \frac{\partial^2 \varphi}{\partial x_i \partial x_k} = 0 \qquad\qquad 2.8$$

In order to solve the task of wave propagation for piezoelectric material domain, the equations for anisotropic half space 2.45 should be applied. In this case the piezoelectric domain present itself an anisotropic material - lithium niobate 127.86° Y-cut with wave propagation in X direction. That specific material cut has strong coupling to Rayleigh waves. It can be described with Rayleigh wave equation 2.37 with scalar and vector potentials that can be derived from 2.38 and 2.39. The displacement can be obtained from 2.41. Therefore, the FEM simulation tool should describe piezoelectric materials and solve equations for coupling of surface potential into induced mechanical stress and vice versa, the problems of accumulation of surface charge as a result of deformation of piezoelectric material. For that specific task, "Acoustic module" of COMSOL™ Multiphysics software is one of the most appropriate solutions. It allows to describe three dimensional problems with anisotropic materials of certain crystallographic orientation, simultaneously with isotropic solid domains and liquid domains.

The isotropic domains, such as electrodes or isotropic structures (overlayers and etc.) were described as "Linear elastic material". The simulation was governed by equations $2.1 - 2.5$. In order to avoid unnecessary reflections from the finite structure boundaries, the model allows to specify artificial absorbing domains that prescribed as perfectly

matched layers (PML). The geometry of simulation model of SAW part of the sensor structure with described above domains is shown in Figure 2.2.
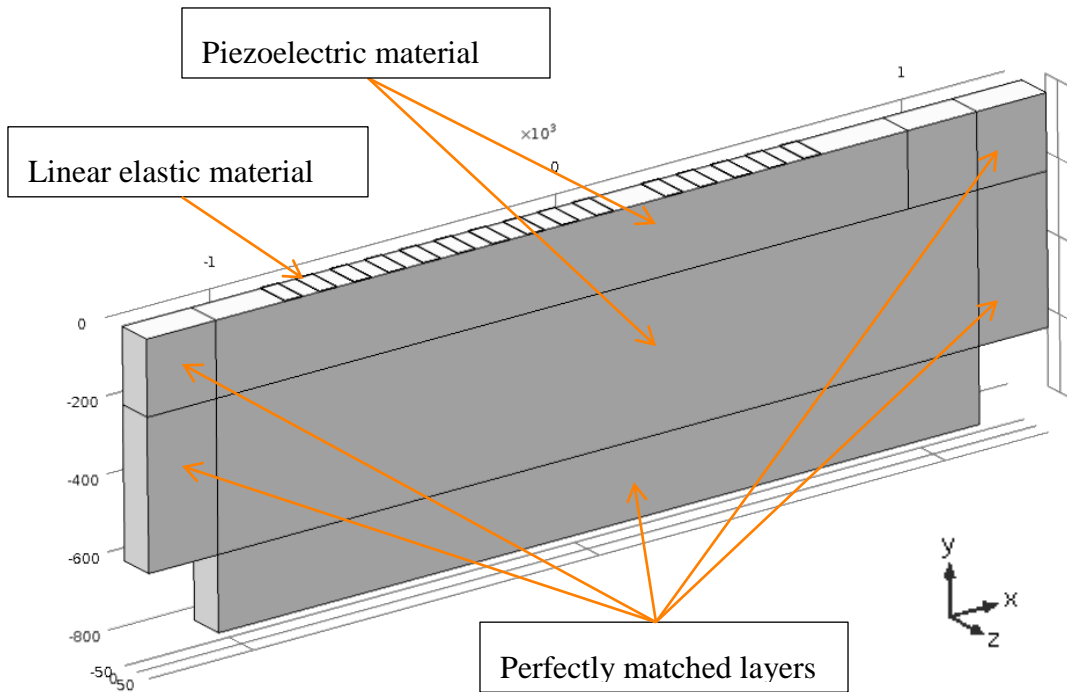
Figure 2.2 Simulation model geometry of SAW part of the sensor structure with specified. domains

In order to simplify the simulation model and integrate it to existent simulation capacity, the geometry was reduced by means of application of periodic boundary conditions. The plane of the waveguide surface is orthogonal to Y direction that defines the Y cut of the geometry. The IDTs are placed perpendicular to X axis along expected wave propagation.

For the planes of lateral sides of the structure in Z direction, the periodic boundary conditions are prescribed. That makes the structure infinitely long in Z direction by periodic translation of displacement and potential, Figure 2.3.
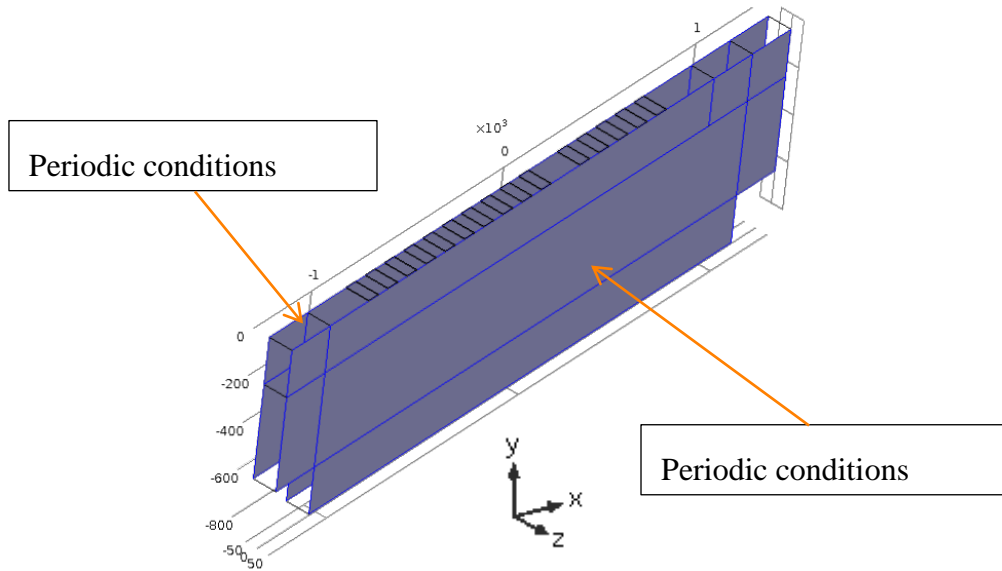
Figure 2.3 Demonstration of planes with applied periodical conditions

In order to simulate the certain wafer cut, it is necessary to implement a rotated coordinate system. The utilized lithium niobate 127.86° Y-cut wafers with a wave propagating in X direction are schematically demonstrated in Figure 2.4 . The cut information is obtained from the wafer manufacturer.
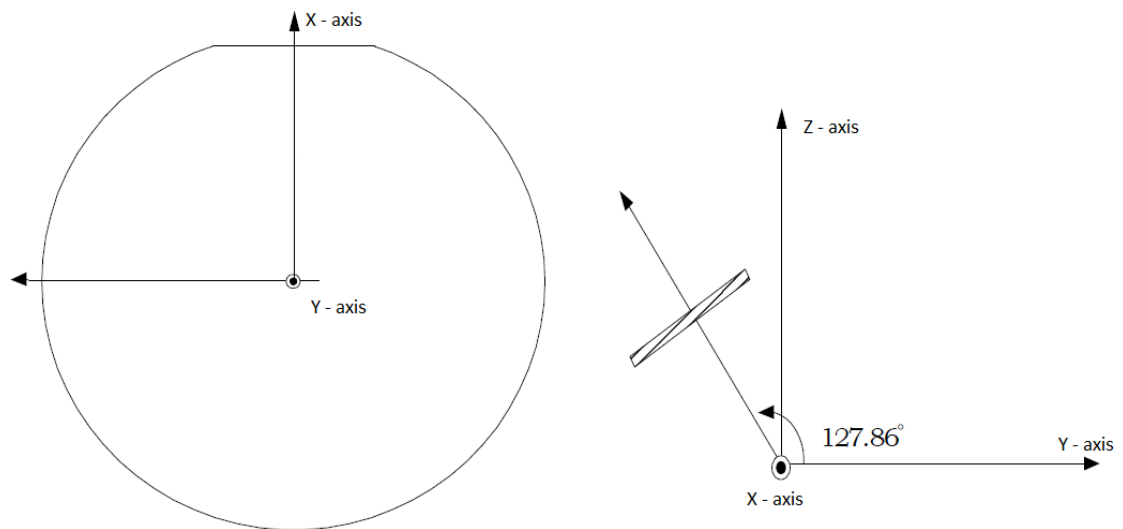
Figure 2.4 Schematic representation of lithium niobate wafer 127.86° Y-cut with wave propagation in X direction

In utilized model, the rotated coordinate system with Euler angles (0, 37.86°, 0) was applied to prescribe the rotation of anisotropic piezoelectric domains. Regardless the

fact that it is relevant only for anisotropic domains, the new rotated coordinate system is applied for the whole model making no influence on isotropic model domains.

The excitation of acoustic waves in a certain frequency range is completed by means of IDTs that are defined as periodically placed metal stripes with geometry defined by the SAW structure design. For the wave excited electrodes the electric potential and grounded electrode's boundaries were specified. The electrodes of receiving part of the two port SAW device were prescribed with floating potential and grounded conditions. Summarized electrodes conditions are shown in Figure 2.5 .
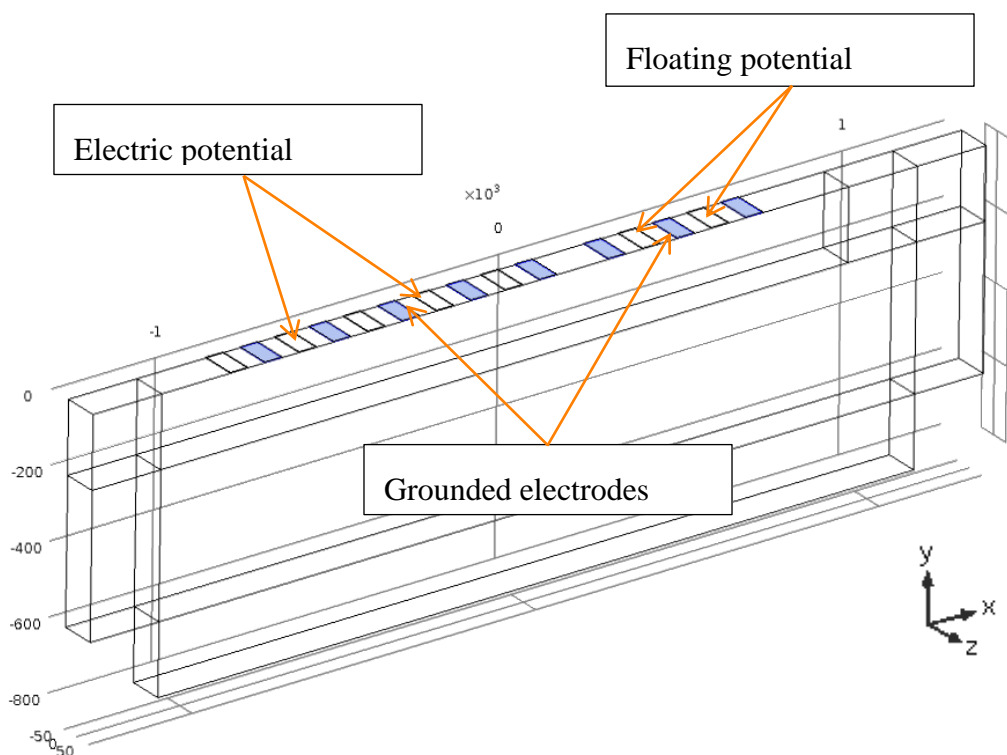
Figure 2.5 Surface boundary conditions for SAW structure electrodes.

Meshing of the structure was completed with COMSOL adaptive mesh refinement tool. The most critical point regarding the meshing is that the meshed structure provides predictable and uniform solutions along the boundaries. Application of periodical boundary conditions makes it critical for the mesh to be optimized for periodic translation. Incorrect meshing at periodic boundaries can create accumulated errors. The meshed simulation model is demonstrated in Figure 2.6.
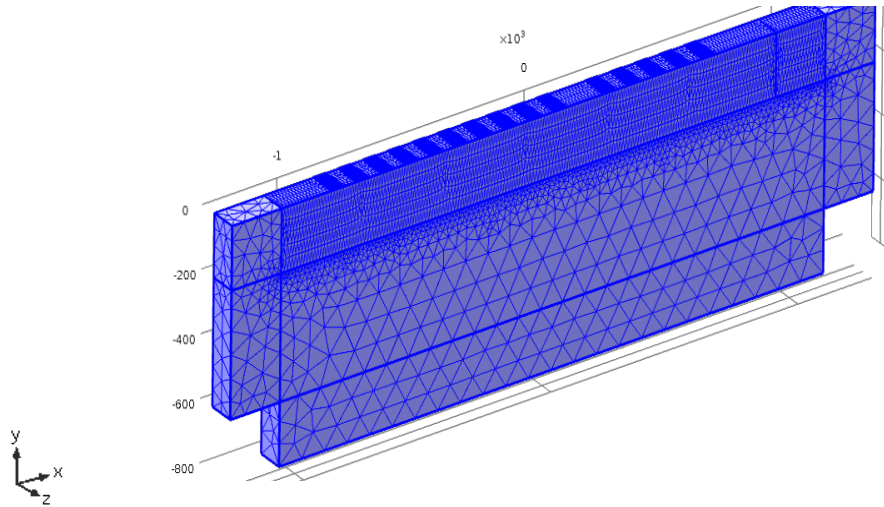
Figure 2.6 Meshing of the simulating geometry.

Demonstrated meshing results were obtained applying of simultaneous meshing of surfaces and domain volumes that allows achieving the mesh uniformity with predefined density for each separated domain. The densification of the mesh is especially required for the areas where the localization of acoustic waves is expected. In current case, the acoustic waves are strongly localized in near the surface region (Rayleigh wave). The numerical simulation of described structure was completed in a frequency domain in the range of 10-30 MHz. The frequency step was set to 50 KHz. The total structure displacement at the boundaries under the receiving electrodes is demonstrated in Figure 2.7.
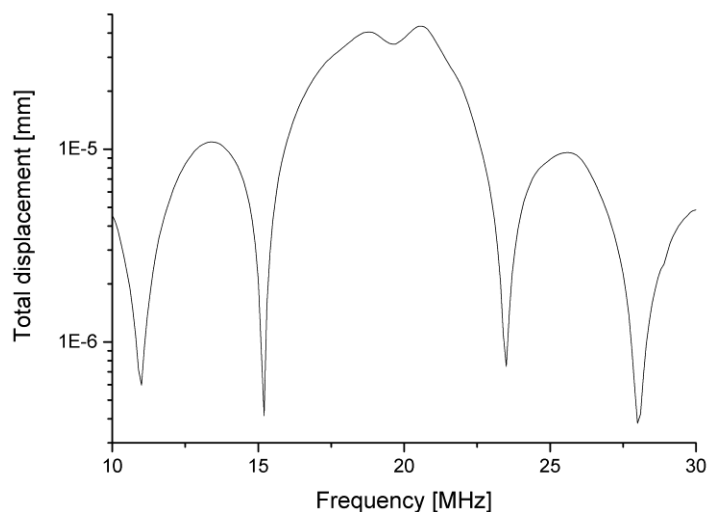
Figure 2.7 Results of the analysis of frequency dependence of total surface displacement at the boundaries under receiving electrodes.

The achieved frequency dependence demonstrates an expected response of the equidistant unapodized SAW structure. The bandwidth of the SAW passband is considerably broad because the number of IDT finger pairs is relatively low. At the same time the expected signal losses are also relatively low because of highly efficient coupling of applied electrical field to surface acoustic wave of chosen lithium niobate 127.86° Y-cut substrate material.

The Y component of the surface displacement field at structure central frequency of 20 MHz is shown in Figure 2.8.
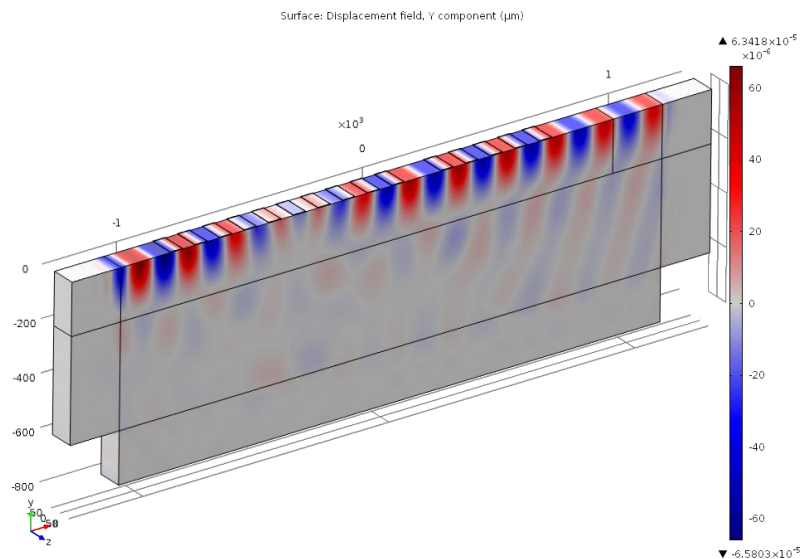
Figure 2.8 The Y component of surface displacement field at 20 MHz.

The components of displacement are shown at different planes in Figure 2.9
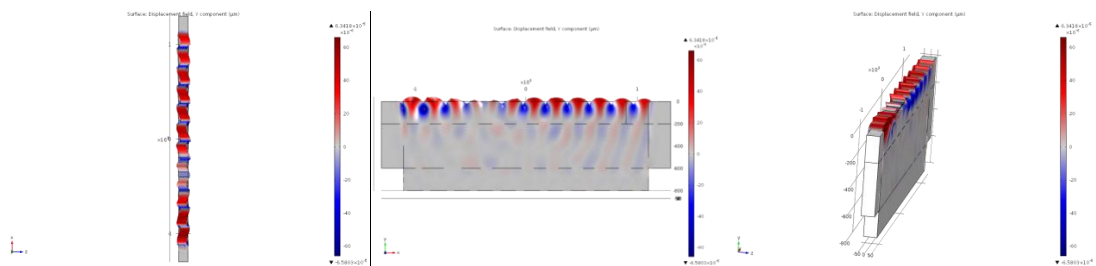
Figure 2.9 Displacement of surface acoustic wave in view from different planes

2.8.   SAW structure design

In order to realize a SAW sensor device that can operate in a reasonable signal input range, the SAW device has to be initially designed to excite and receive acoustic waves in a broad band frequency range. To satisfy this demand, the SAW device can be

designed as apodized broad band SAW filter or as unapodized delay line. Apodization reduces the losses and creates a passband with predefined properties, but at the same time, the simulation of the phononic sensor that is based on apodized SAW is time consuming. Unapodized SAW structures cover the required frequency band as well and achieve a reasonable calculation time.

2.8.1. Unapodized SAW structure design

Excitation and reception of surface acoustic waves is realized usually with inter-digital transducers (IDTs) on a piezoelectric substrate. The IDTs are an array of periodically deposited metal electrode fingers. Several widely applied SAW substrate materials such as quartz, lithium niobate, lithium tantalite can be utilized with different cuts determining the type of the surface wave, the temperature stability, the bandwidth of a passband etc.

Quartz substrates are currently the most cost efficient substrates. The application of well-known cuts such as ST-cut, AT-cut, Y-cut makes possible to build SAW devices based on Rayleigh wave, shear horizontally polarized acoustic waves, Love-waves and etc. Despite the number of advantages, quartz has low electro-mechanical coupling that sequent in signal losses and deteriorating of final sensor efficiency. An increase of the number of IDT finger pairs can considerably improve the signal-to-noise ratio but it considerably narrows the passband of the device (this can be overcome utilizing the apodized IDTs).

Lithium Niobate is well known and widely utilized for SAW devices material similar to quartz but it has considerably higher electro-mechanical coupling coefficient. Depending on the required wave type, different lithium niobate wafer cuts such as 128º Y-cut, 42º Y-cut and Y-cut can be applied for the SAW device. A broad band frequency response without dramatic signal losses can be achieved by placing IDTs with only several pairs of electrodes. Such a trivial design allows reduces the calculation model and supports experimental investigation without considerable sensor signal losses. Lithium niobate 128º Y-cut SAW substrate material has been chosen as a SAW based phononic crystal sensor substrate for its efficient coupling to Rayleigh wave having X-direction of wave propagation.

Active IDTs are connected to a HF-voltage (high frequency) source or an HF-amplifier. The generating electric field penetrates the piezoelectric material and causes mechanical stress. Vice versa they collect the surface charges created by mechanical stress and provide an electrical output signal. Electrodes that are placed without connection to the IDTs bars are called passive electrodes. Periodic spatial distribution of SAW active electrodes along the surface of piezoelectric substrate creates a periodic distribution of electric potential that induces periodical mechanical stress on the piezoelectric surface which initiates a surface wave excitation in case of applied alternating electrical field with appropriate frequency. Vice versa, a surface acoustic wave propagating along the piezoelectric material induces periodical spatial charge distribution that can be read as a receiving signal. Electrodes with an equal aperture, geometry (width and distance between neighboring electrodes) and period along the wave propagation are called equidistant unapodized IDTs. Figure 2.10 demonstrates an example of an equidistant unapodized ITDs.
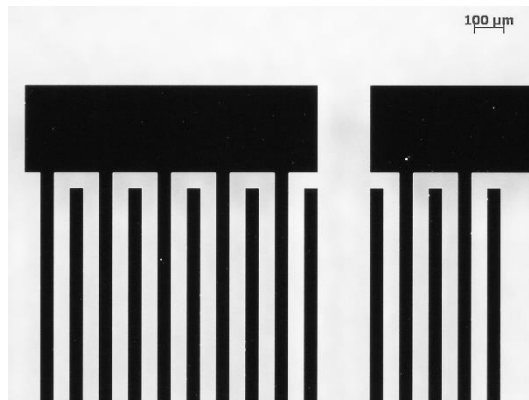
Figure 2.10. Example of manufactured equidistant unapodized IDTs.

If the spatial period of the electric field corresponds to the wavelength of the surface acoustic wave, waves excited by each of the electrodes pairs will be summed up. A distance between neighboring IDT electrodes can be defined as:

$$d = \lambda/2 \qquad\qquad 2.46$$

where: λ is a SAW wavelength $\lambda = v / f_0$; v is a SAW phase speed and f_0 is the frequency of an acoustic synchronism.

For equidistant unapodized IDTs the width of electrodes is $\lambda/4$ and the period of electrodes of the equal potential is λ. The equidistant unapodized IDT and

corresponding potential (a) and displacement (b) fields on lithium niobate 127.86° Y-cut are shown in Figure 2.11.
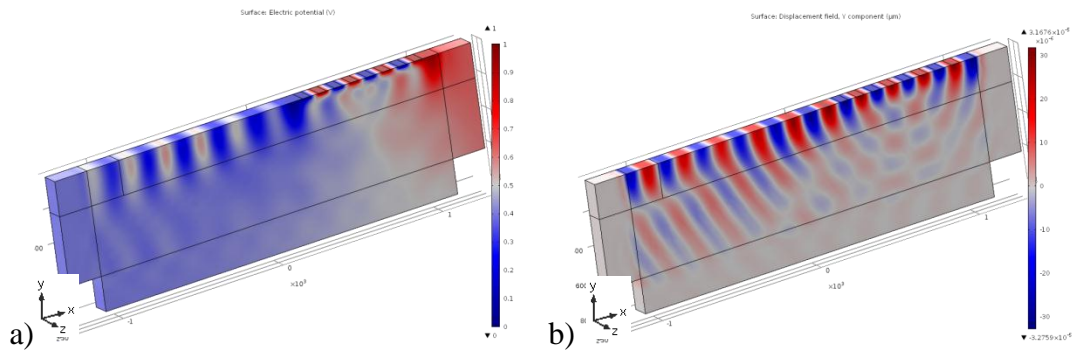
Figure 2.11 The potential field a) and Y component of displacement b) of acoustic waves propagating in X direction of 127.86° Y-cut lithium niobate substrate.

An overlapping of the equidistant unapodized IDTs (aperture) should be chosen to adjust the IDTs impedance to the external measuring circuit (commonly applied 50 Ohm). In most cases, the aperture of IDTs satisfies the region of $20 - 100\ \lambda$.

The coefficient of electrode metallization that is defined as ratio of the electrode width to the free space between the electrodes was chosen as ½. It allows achieving a maximal efficiency of IDTs. The coefficient can be later adjusted technologically to obtain the required frequency spectrum response.

Second-order effects can disturb both the initial transmission spectrum of the SAW device and interference with the response of the phononic sensor structure. They must be compensated. Specifically the reflection of incident surface acoustic waves by IDTs is the effect that has to be considered. Waves that were reflected by the output transducer and then by the input transducer reach the output IDT giving rise to the "triple transit" signal that causes an appearance of unwanted ripples in amplitude and phase. The reflection from a single IDT element is negligible in most cases but the reflection from a periodical array of electrodes where each single reflection adds in the phase with another can be considerable. In order to eliminate an appearance of the "triple transit" signal, double electrodes (or so called split electrodes) transducers are typically utilized. The Figure 2.12 demonstrates an example of manufactured IDTs with split electrodes.
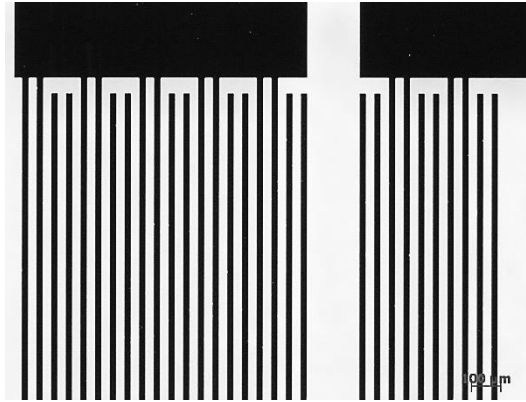
Figure 2.12 Manufactured split electrodes IDTs.

The respective displacement field generated by split electrodes on the $128°$ Y-cut lithium niobate substrate is shown in Figure 2.13.
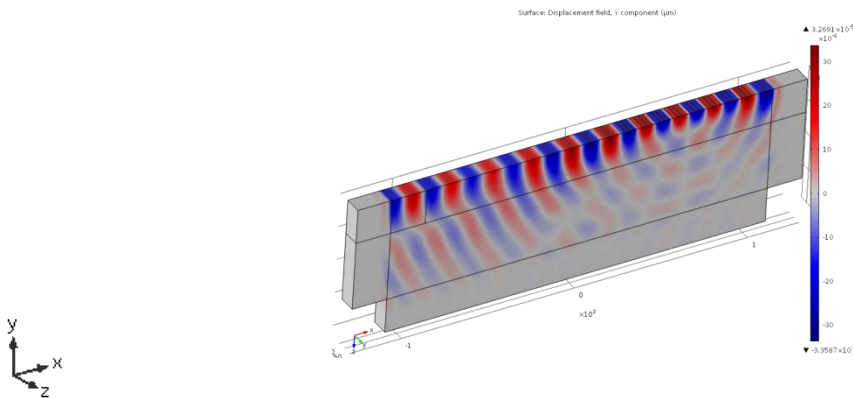
Figure 2.13 Displacement field excited by split electrodes transducer

The distance between two IDTs should be taken into account to avoid multiple reflections from the receiving IDT electrodes that can cause the disturbance of the initial transmission response. If the distance between the IDTs is lambda fold, the in phase addition of incident and reflected waves from IDTs causes a disruption of the transmission curve on a central frequency. The results of the numerical simulation are shown in Figure 2.13.
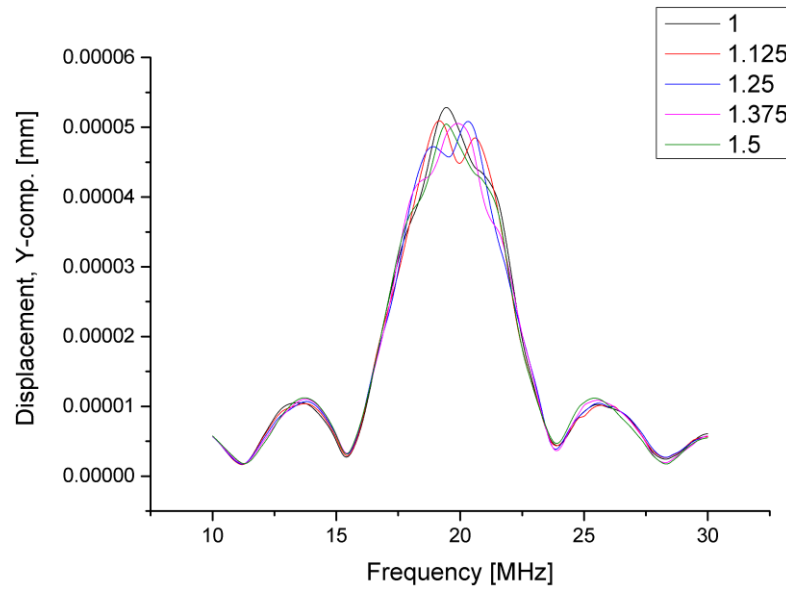
Figure 2.14 Numerical simulation results of distance variation between receiving and sending IDTs. The presented curves correspond to distances equal λ, 1.125 λ, 1.25 λ, 1.375 λ and 1.5 λ at central frequency 20MHz.

Another specific engineering parameter of unapodized SAW structures is electrical resistance. In order to reduce power dissipation in IDTs electrodes, it is required that their surface resistivity is small. Therefore, a material of electrodes has to be highly conductive and the thickness of electrodes should not be too thin. On the one hand, the electrodes thickness defines an efficient coupling of the excited surface acoustic wave and on the other hand, it provided a mass load on a waveguide surface that can cause an additional reflection of incident surface waves. From the technological point of view, it is more challenging to structure considerably thick metal films with the predefined shape because of the limits of isotropic wet metal etching techniques.

Common practice regarding electrodes thickness is 2-4% of the wavelength. In case of the 128º Y-cut lithium niobate substrate and a 20 MHz central frequency, the electrodes thickness should be 4-8 µm. Etching of metal layers of such thickness can cause the appearance of a trapezoidal electrodes shape and non-uniform mechanical load on a waveguide surface along of the SAW propagating path. The reduction of electrodes thickness can cause a coupling efficiency reduction. In order to keep a technologically convenient electrode thickness and to conserve the device efficiency, the behavior of the surface average displacement for different electrodes thicknesses was analyzed.

Figure 2.15 demonstrates the surface total displacement for three different electrodes thicknesses in frequency range of 10 – 30 MHz. It can be seen, an increase of electrode thickness improves the coupling to the surface acoustic wave but at the same time significantly disturb the uniformity within passband. The observable frequency downshift caused by an increase of mechanical load from IDTs.
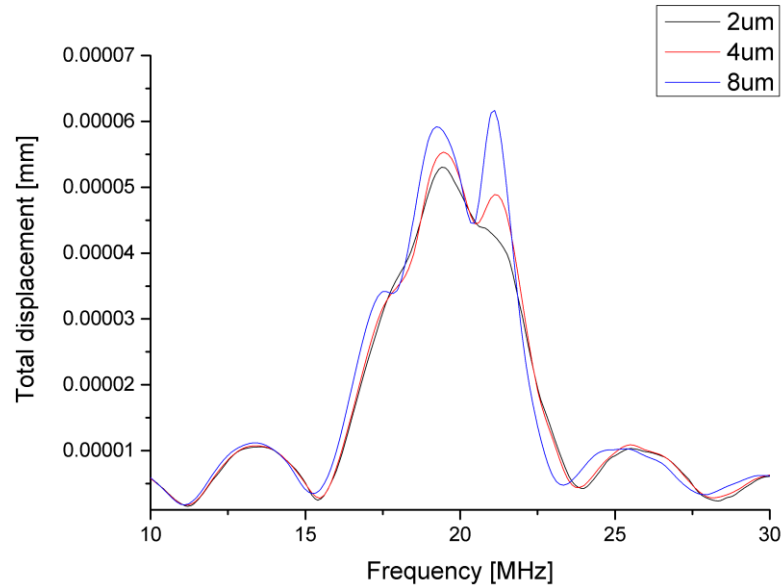
Figure 2.15 Surface average displacement of a free area excited by IDTs with the different electrodes thickness

In case of aluminum electrodes, the optimal electrodes thickness can be found at the value of the surface resistivity of 0.5 – 0.7 Ohm/□.

As mentioned already, the number of IDT pairs influences the values insertion losses and bandwidth of the SAW structure in opposite direction. In order to find an optimal ratio between the bandwidth and insertion losses, the equivalent circuit of IDTs together with matching circuits must be taken into consideration. The equivalent circuit of the IDTs with the matching circuit can be presented in a following way, Figure 2.16.
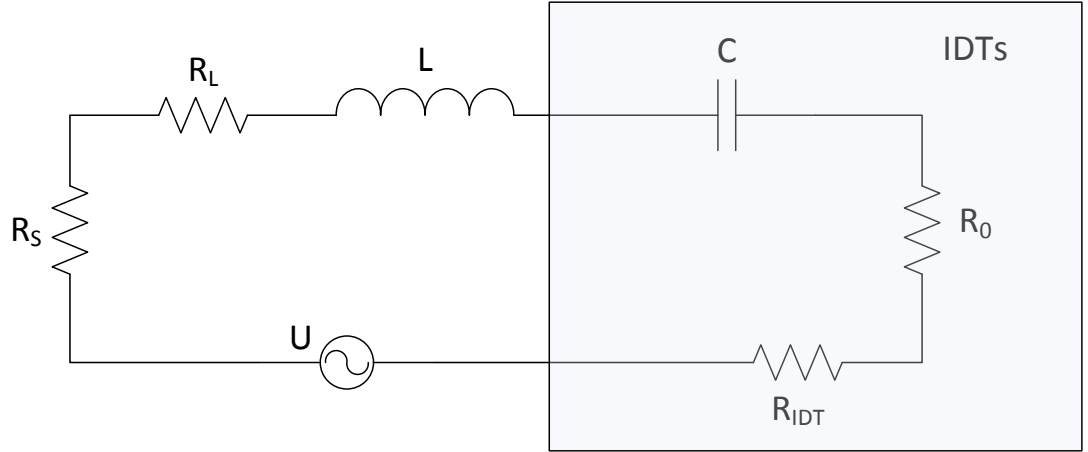
Figure 2.16 The equivalent circuit of IDT connected to a signal source with the matching circuit.

The single IDT can be described as a circuit containing the capacitor C that is defined by the capacitance between the electrodes, the electrical resistance of electrodes R_{IDT} defined by the IDTs conductivity, and the acoustical resistance R0 is defined by the power of the surface acoustic waves excited by IDT, $P_{acoustic} = I^2 R_0/2$.

The quality factor of the presented equivalent circuit can be found as:

$$Q = \frac{2\pi R_0 C}{R_0 + R_{IDT} + R_L + R_S} = \frac{2\pi R_0 C}{R_0(1 + \eta)} = \frac{Q_0}{(1 + \eta)} \quad 2.47$$

where Q_0 is the IDT quality factor.

$$\eta = \frac{R_{IDT} + R_L + R_S}{R_0} \qquad 2.48$$

The electrical bandwidth can be found as:

$$(\frac{\Delta f}{f_0}) = (1 + \eta)/Q_0 \qquad 2.49$$

The IDTs quality factor can be also found as:

$$Q_0 = \frac{\pi}{4K^2 N_{el}} \qquad 2.50$$

Then, the electrical bandwidth can be presented as:

$$\left(\frac{\Delta f}{f_0}\right) = \frac{4K^2 N_{el}}{\pi}(1 + \eta) \qquad\qquad \textbf{2.51}$$

At the same time, the relative acoustical bandwidth can be described as:

$$\left(\frac{\Delta f}{f_0}\right) = \frac{0.89}{N_{el}} \qquad\qquad \textbf{2.52}$$

An optimal number of electrodes can be defined as a balance between the electrical bandwidth that is proportional to the number of electrodes pairs N_{el} and the acoustic bandwidth that is inversely proportional to N_{el}. The maximal bandwidth is achieved on condition where acoustical and electrical bandwidths are balanced. However, designs where the electrical bandwidth twice exceeds an acoustical are commonly applied in practice.

$$\frac{4K^2 N_{el}}{\pi}(1 + \eta) = 2\frac{0.89}{N_{el}} \qquad\qquad \textbf{2.53}$$

Then, the number of electrodes pair can be found:

$$N_{el} = \sqrt{\frac{0.89\pi}{4K^2}\frac{2}{(1 + \eta)}} \qquad\qquad \textbf{2.54}$$

Minimal matching losses can be achieved when $\eta = 1$

Then, equation can be reduced to:

$$N_{el} = \sqrt{\frac{0.89\pi}{4K^2}} \qquad\qquad \textbf{2.55}$$

The minimal number of IDT electrodes pairs for $128°$ Y-cut lithium niobate substrates satisfies the balance between acoustical and electrical bandwidths:

$$N_{el} = \sqrt{0.89\pi/(4(0.053)^2)} \approx 4 \qquad\qquad \textbf{2.56}$$

Completed calculations demonstrate that the most balanced ratio between bandwidth and inserted losses can be achieved when the acoustic wave is excited with 4 pairs of electrodes. That allows keeping the broadband covering of the excited wave frequency range with considerably low signal losses

2.8.2. The apodized SAW structure design

Apodization is a commonly used technique to define the SAW filter frequency response. Changing of overlap between adjacent electrodes and modifying their polarity along the waveguide surface is the most frequently used method. A standard transversal SAW filter consists of one apodized and one unapodized IDTs. In the current work the Remez algorithm used for the design of a finite impulse response of linear phase digital filters [74] was applied for calculating the parameters of IDT apodization. A considerably broader bandwidth response with much lower inserted losses can be achieved. The computation under Remez algorithm defines the impulse response coefficients. Application for weighted electrodes design provides the designed SAW filter frequency response with predefined tolerances. The digital impulse sequence defined by the obtained coefficients provides all necessary information regarding each pair of electrodes overlapping.

A SAW filter with central frequency of 100 MHz was designed, manufactured and analyzed. The frequency response measured without matching circuits using the high frequency probe station is shown in Figure 2.17.
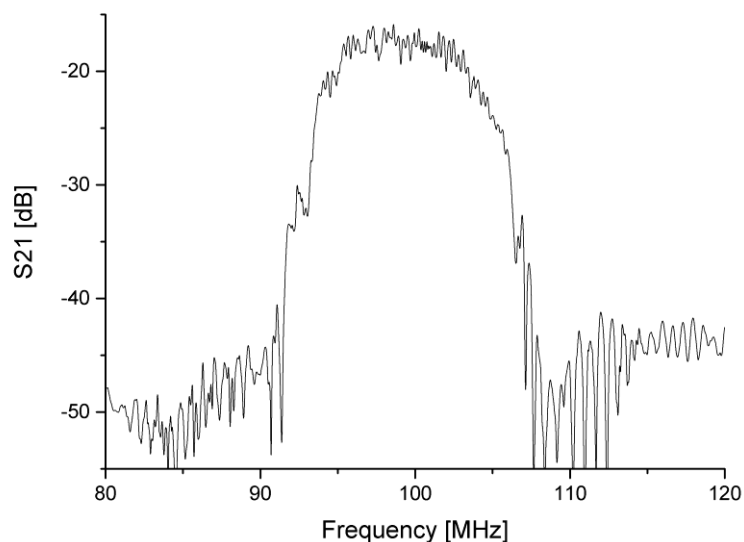
Figure 2.17 Measured frequency response of the SAW filter calculated with the Remez algorithm (none matching circuits are applied, measurements performed with high frequency probe station).

The design of the sensor applies interfacial layers for coupling of acoustic waves into the structure; therefore, the manufactured apodized SAW structures were analyzed with overlayers of different polymer materials. Two different polymer layers (SU-8 5 and AZ15nxt) were spin coated with a thickness of 5µm on the whole wafer with fabricated IDTs. Respective frequency responses are shown in Figure 2.18.
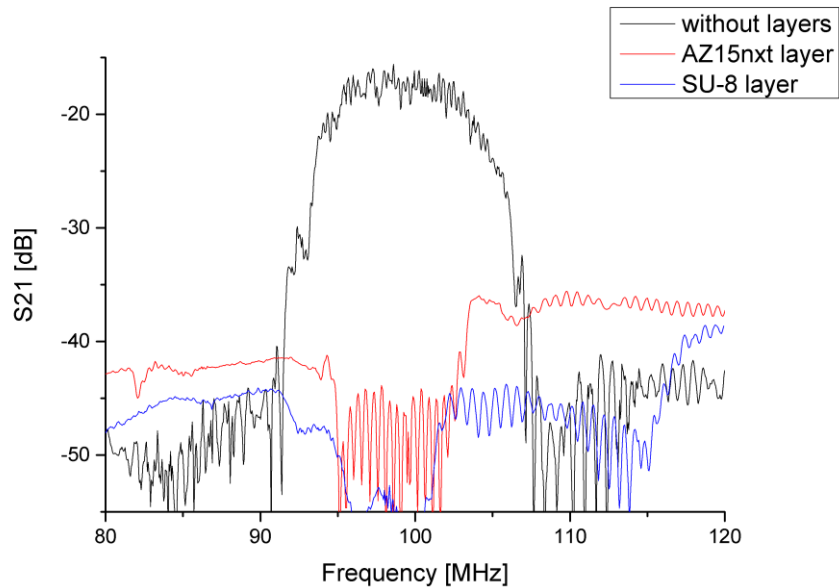
Figure 2.18 Measured frequency response of the SAW filter with overlayers of AZ15nxt and SU-8.

The deposition of overlayers on the waveguide surface completely destroys the frequency response of the apodized SAW structure. Despite all the advantages of apodized SAW structures regarding bandwidth and insertion losses, significant influence of overlayers on SAW structure response makes their application in current case relatively complicated.

3 SAW BASED PHONONIC CRYSTAL SENSOR CONCEPT

To design the sensor structure, the approach based on an adaptation of classical SAW gas sensors concept was considered at the first stage of the development. It is based on analysis of the frequency shift of sensor response caused by a change of propagation speed as result of altering the surface mass load. Nowadays this approach is used commercially in gas sensors. With respect to current work, the disadvantage of that concept that it cannot be applied for liquid sensor purposes as shown in more details in the first chapter. Our task to sense volumetric properties of liquid analytes requires a different sensor approach.

Our concept follows the idea to trap the liquid in some structure. Liquid confinement opens the gate to a concept different from mass load. Basic idea behind this approach is the excitation of resonance modes that are responding to properties of the liquid under investigation. For that reason the trapping structure must be excited in some way. Furthermore, the resonance modes of interest must be detectable. In consequence, applying the standard SAW concept, the surface wave must efficiently couple to the liquid confining structure, to excite the resonance modes that must be readable with IDTs.

In the phononic crystal sensors the confined liquid acts as a one of constitutes of the periodic arrangement. Referring to previously developed sensor structures

[55,56,59,60], initial attempts were directed to have the same kind of arrangement where the incident wave passes through the liquid containing periodic structure [57]. For that purpose the structure was integrated directly into the waveguide surface. Unfortunately, this simple approach suffers from significant scattering of the incident acoustic SAW into the bulk causing considerable losses of the sensor signal. Besides of that, etching the structure into the piezoelectric waveguide is challenging under the view of the required accuracies in all three dimensions. The manufacturing of phononic crystal structures within quartz substrate has shown the necessity to apply a thick hard metal mask and intensive long hour etching in order to achieve the required structure geometry [75,76]. The fabrication process developed here has provided sufficient etching results in quartz waveguides. Its application to stronger ferroelectric materials, specifically to lithium niobate and lithium tantalite has been insufficient for sensor applications. In conclusion, we have extended the basic design by a periodic overlayer, which contains the liquid sample.

In more detail, application of the sensor design that is similar to previously investigated millimetre scale structures was inadequate. It applies bulk acoustic waves. Mode conversion is not required. It would actually decrease the transmission factor of the sensor. By contrast, the SAW based phononic sensor approach requires on the one hand mode conversion of the SAW into an at least prevailing longitudinal mode in the liquid cavity. In the second step this longitudinal mode must couple back to the surface wave without significantly deteriorate the wave front while passing through the periodic arrangement of liquid inclusions. This resynchronisation to the SAW wavelength can make the detection of liquid cavity resonances rather complicated and inefficient. It became necessary to introduce a coupling layer (in addition to a cover slit). Now acoustic energy of incident surface wave is transferred into the whole arrangement and excites structural resonances. The number of free design parameters increases dramatically and a large set of different kinds of structural modes can be excited, including those the liquid is involved. Design optimization is two-fold: realization of highly localized structure resonances that can be utilized for liquid sensor purposes and efficient coupling of surface wave to periodic arrangement. This is a second challenging difference to SAW gas sensors where the typically applied sensitive coating is deposited uniformly onto the delay line of the SAW device.

On the other hand, the phononic structure performing these tasks must suppress any unwanted scattering or propagation of any acoustic wave into the bulk of the piezoelectric substrate. Excitation of any kind of structure resonance can cause immediate wave scattering into the bulk. To avoid that, the periodic overlayer structure has to isolate the excited resonance from the piezoelectric carrier. The solution was found by moving the overlayer structure above the receiving IDT's and analysing the transmission minima that correspond to the modes of high acoustic energy concentration within the overlayer structure.

The operating scheme can be described with following sequence. The overlayer structure couples the acoustic energy from incident surface acoustic wave only at specific frequencies that corresponds to structural resonance modes. Among all possible structure modes, the most relevant are those that have a liquid involvement. The induced structure resonances are isolated by the periodic arrangement from the waveguide surface. They appear as transmission minima at certain frequencies.

Although the role of the periodic structure in this particular case is different from commonly applied schemes, we believe that it allows the most efficient implementation of phononic crystal concept into SAW platform. Referring to previous works completed within the frame of this work, the current contribution studies in more details arrangements based on a system of periodically placed microfluidic channels that presumably can provide the expected structure behaviour and can proof the concept theoretically and experimentally. Implementation of described approach based on induced structure resonances in periodical arrangements is studied in terms of application for liquid sensor purposes utilising SAW based platform.

3.1. Phononic structure sensor design

Different phononic structures concepts were previously introduced for a broad variety of applications. Phononic structures were combined with SAW resonators as efficient reflectors as miniaturised alternative to classical metal reflecting gratings [73]. Square lattice phononic structure realized as an array of periodically etched holes was integrated in a ZnO/Si SAW device. At the central frequency of 212MHz it was demonstrated that 15 periods are sufficient to achieve a 7 dB insertion loss. The same approach was undertaken for the Lamb wave SAW resonator utilising AT-cut quartz

substrate. Theoretical investigations of phononic structures for acoustic waveguides applications were performed with a finite-difference time-domain method showing the localisation and propagation of acoustic modes within the phononic structure that is made of circular steel cylinders in a square lattice placed in an epoxy matrix [77].

In order to complete theoretical investigations of structure-surface wave interactions, finite element method (FEM) using program platform COMSOL^{TM} Multiphysics was applied. To solve the simulation task, it was necessary to combine the interactions between piezoelectric model, linear elastic model and pressure acoustic model. Piezoelectric model solves the problem of conversion of electrical potential applied to surface defined electrodes into an acoustic wave, besides the excited wave type depends completely on substrate predefined cut and electrodes design. Linear elastic model describes an interaction of solid structure with incident surface acoustic wave. The elastic deformation described by a linear elastic model describes only the elastic deformation in solid domains of the phononic structure. At the same time the pressure acoustic model describes a behavior of liquid domains of the periodic structure and calculates the pressure distribution in a liquid initiated by the solid domains of the structure.

Designed in current work SAW based liquid sensor completed as a microfluidic arrangement fabricated atop of receiving IDTs. The microfluidic part of the sensor is defined between interfacial and covering polymer layers. An interfacial layer, on the one hand, couples the incident surface acoustic wave to the microfluidic channels and, on the other hand, isolates liquid from the IDTs. The channels are closed from the above with another polymer layer that encloses liquid containing volumes.

The optimal thickness on interfacial layer that couples the incident surface acoustic wave was estimated equal to the quarter of the wavelength in SU-8 polymer. That layer can be considered as a matching layer between the structure and SAW waveguide. The Young's modulus of standard processed SU-8 layers has a value of 4.95 GPa. The SU-8 density is specified equal to 1200 kg/m^3. The speed of sound in solids can be estimated with a following relation, 3.1

$$v_s = \sqrt{\frac{Y}{\rho}}$$

<div align="right">3.1</div>

Where Y is Young's modulus, ρ is mass density and v_s is speed of sound.

Considering the calculated speed of sound in SU-8 polymer as 1830 m/s, the wavelength at central frequency 20MHz (f) can be found as $\lambda = v_s / f$ From the symmetry reasons, the thickness of the covering SU-8 layer was also prescribed equal to the quarter of the wavelength in polymer layer. The thickness of the microfluidic layer (the height of liquid volumes) was estimated with relation to the wavelength in liquid domain. Considering the possible biomedical application of developing structure, its design should be estimated for a speed of sound of water kind of liquid that is approximately 1500 m/s. The thickness of microfluidic layer was estimated as 1/5 of the wavelength in liquid domain.

In [78] we have introduced the concept for a fist time and demonstrated the advantages of this approach in comparison to waveguide etched structures. For certain designs it was possible to achieve relatively narrow structure resonances revealed as maximums of displacement taken from the top boundary of the structure. At the same time, the structure analysis also revealed a relatively complex structure vibration behavior.

The numerical simulations were performed for several structure designs. The substrate material is lithium niobate Y-cut. Simulated structure dimensions were defined with respect to the wavelengths at 80MHz.The liquid containing structure is prescribed with material properties of SU-8 polymer. The channels were defined as water filled. The displacement frequency dependence for a single channel structure, Figure 3.1 a) demonstrates a rather complex structure behavior. As an example, the Y component of displacement field distribution at frequency 75.5MHz is shown in Figure 3.1 b). As it can be seen, the single channel structure design does not allow to achieve isolation of structure resonances that is required for sensor purpose applications. Structure displacement patter also does not demonstrate efficient isolation of structure modes from the SAW waveguide.
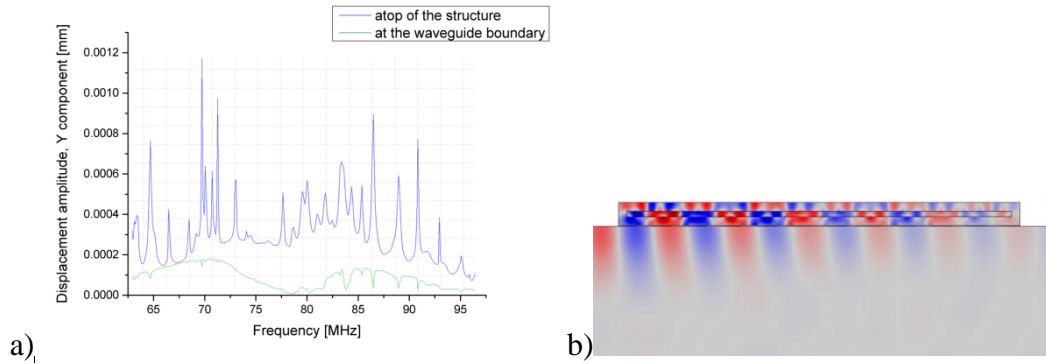
Figure 3.1. Frequency response a) and Y-component of displacement field at frequency 75.7 MHz b) for a single channel structure.

Taking the single channel structure behavior as a reference starting point, further structure development was conducted with the purpose of obtaining the isolated liquid dependent structure resonances. For that reason the separation of the fluidic structure into the channels with confined within liquid was made. The lattice constant of the microfluidic channels was as a half of the wavelength of SAW. The channels filling fraction (channel width – distance between neighboring channels) was set by the rate 0.9 – 0.1 of the SAW wavelength. The geometry of analyzed structure is demonstrated in Figure 3.2 a). As a result, separation into the channels allowed to suppress some of structure resonances and separate an isolated resonance that is responding on parameters of the liquid cavity. As it can be seen in Figure 3.2 b), the variation of the microfluidic channels thickness causes a significant shift of one of the pronounced structure mode. It is assumed that it is a resonant mode that includes the liquid volume and presumably can depend on properties of the defined in channels liquid.
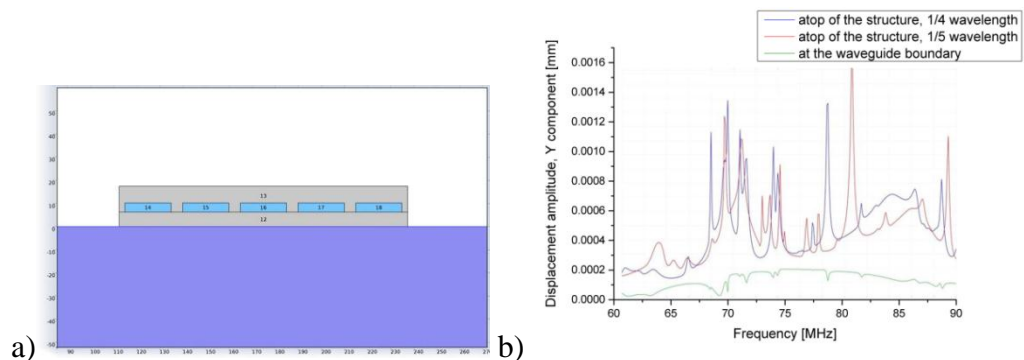
Figure 3.2. Structure geometry a) and out-of-plane displacement amplitude taken atop the structure b) with channel thickness of 1/4 (blue curve) and 1/5 (red curve) of the wavelength in water [78].

The cases of microfluidic layer thickness variation from quarter of the wavelength in water to 1/5 of the wavelength, revealed shift of one of the displacement maxima to a higher frequency. The amplitude of this displacement maximum taken from the top of the structure demonstrated a slight amplitude increase for the case of microfluidic layer thickness equal to 1/5 of the wavelength. The frequency position and amplitude of other displacement maxima that are separated in a frequency scale from the one that is affected by microfluidic channel height remain almost not effected by the microfluidic layer thickness variation.

The increase of number of channels deteriorates the structure modes that appeared in previous design responding to channel geometry, Figure 3.3 a). The displacement field taken at frequency 67,3 MHz is an example of the structure modes, Figure 3.3 b).
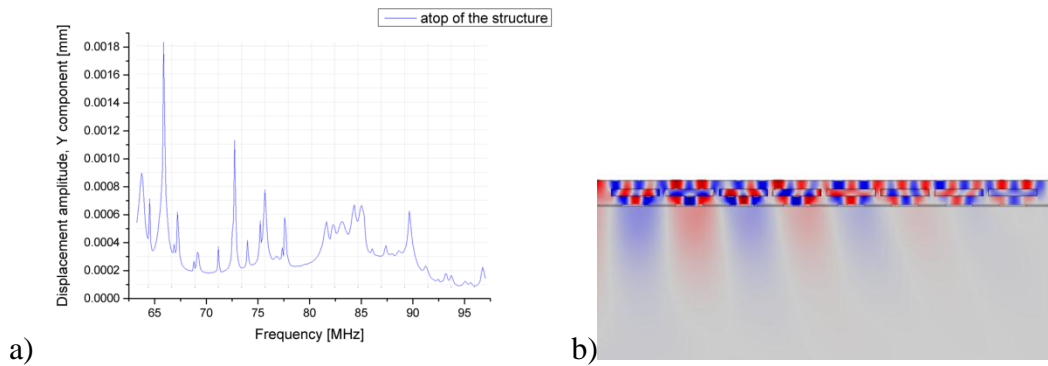
Figure 3.3. Frequency response a) and Y-component of displacement field at frequency 67.3MHz b) for 8-channels structure.

A further increase of number of channels enriches the frequency response (Figure 3.4 a) with various structure vibration modes, Figure 3.4 b).
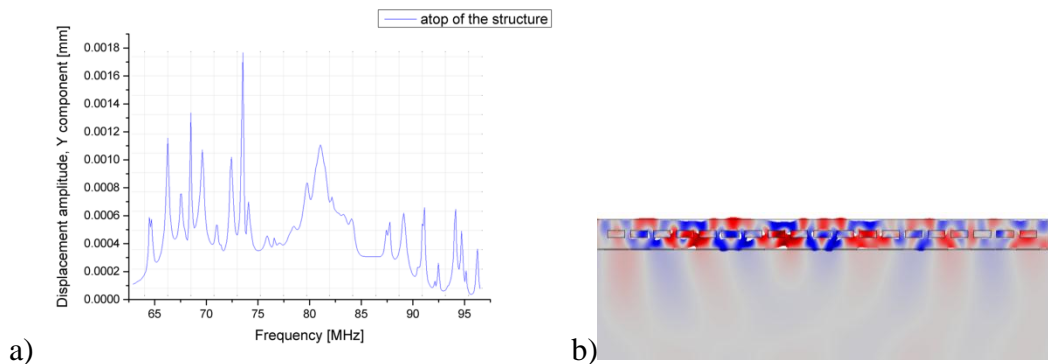
Figure 3.4. Frequency response a) and Y-component of displacement field at frequency 81.2 MHz b) for 19-channels structure.

The frequency dependence of a 19-channels structure displacement may resemble the bandgap behavior at some frequency region. At the same time the displacement spectrum becomes rather complicated and exhibits a broad variety of structural vibrations.

As a result of two dimensional simulations, it was revealed that the structure design has a certain balance between structure complexity and the structure response. The increase of number of channels improves the structure response, but, after some number of channels, the behavior becomes rather complicated with an increased variety of structural vibrations. In comparison to previously described approaches that are based on structuring of the waveguide surface, current SAW based periodic structure design demonstrate the ability to realize the phononic sensor concept as an integrated solution completed as a microfluidic arrangement coupled to the surface waves. The results of two dimensional numerical simulations vividly demonstrate the efficient coupling of incident surface wave to the sensor structure. It is seen that previously existing fundamental problem of wave scattering into the waveguide volume can be overcome with proposed microfluidic concept. On the other hand, the obtained results do not provide the complete understanding on the physical background of the structure resonances appearing in the microfluidic periodic arrangement. In order to get more insights that allow to explain structure behavior, the arrangement was numerically simulated with three dimensional model that more closely describe the sensor device that was later fabricated for experimental verification of developed sensor concept. Because of technological reasons, the central frequency of the sensor device was scaled down to 20MHz. That allows to withstand the structure geometry tolerances and easily handle the microfluidic part of the device.

The numerically simulated arrangement consists of the system of four periodically placed channels with dimensions adjusted to the frequency of 20MHz. The design of described structure with specified domains is demonstrated in Figure 3.5. The respective geometry data is specified in Appendix 1. The material data for simulation domains is described in Appendix 2.
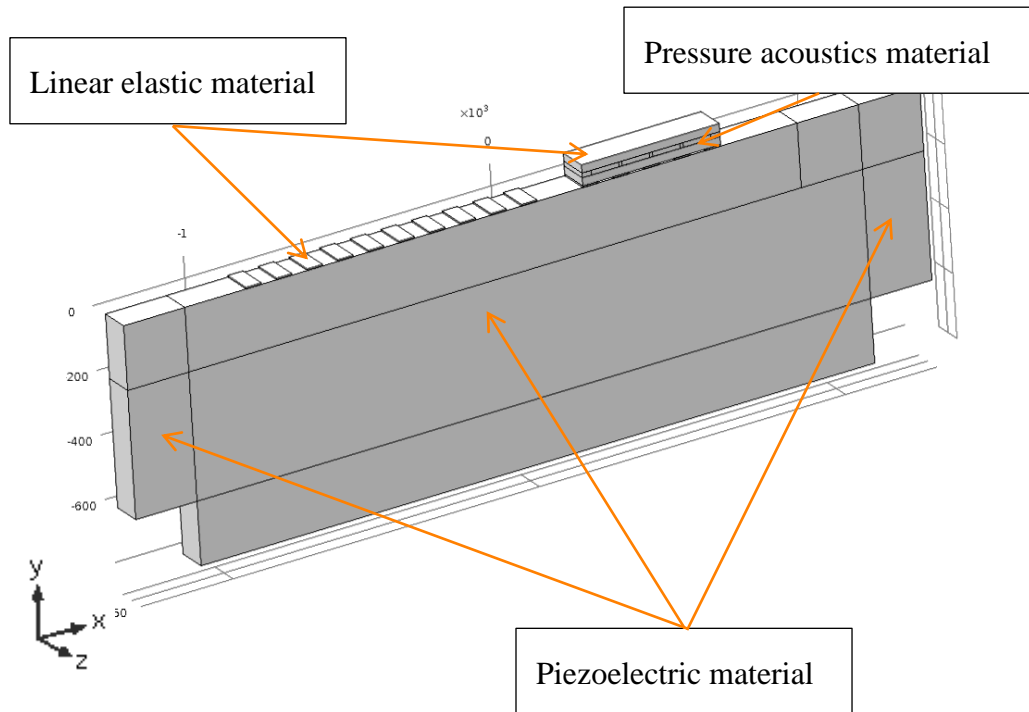
Figure 3.5. Computational model for FEM numerical simulation with specified domains.

The computational model that is shown in Figure 3.5, consist of three different types of domains, each of which is described with separate system of equations. The "Piezoelectric material" domains describe an anisotropic behavior of piezoelectric materials where deformation is coupled with induced by piezoelectric effect charge and vice versa. In current model, "piezoelectric material" prescribed domains are piezoelectric waveguide and PML domains. They are predefined as $127.86°$ Y cut lithium niobate material with wave propagation in X direction. The cut is defined with rotational coordinate system that recalculates the respective material properties in accordance with Euler angles prescribed in rotation coordinate system of the model. The "linear elastic material" domains are described with the system of motion equations for elastic waves in a solid body. The computational domains of polymer microfluidic structure and IDTs are described as isotropic materials that are mechanically coupled to piezoelectric waveguide. The "linear elastic material" model describes propagation of elastic waves in prescribed domains and contains governing system of equations for describe the periodic polymer solid structure displacement behavior. The liquid that is filling the microfluidic channels is described with pressure acoustic model that transforms the displacement of liquid-solid boundary to the pressure distribution within

liquid channels and vice versa. It describes the propagation of pressure waves in liquid domains and contains the liquid material properties that are targeted for sensing (such as speed of sound and density).

Model boundaries in Z planes are prescribed with periodic boundary conditions that makes the whole arrangement infinitely long in Z direction. This boundary condition allows significantly reduce the computational model to complete the simulation tasks within meaningful time duration. The surface acoustic wave excitation is completed with prescribed periodic potential distribution along the X direction of the waveguide surface. For that reason the electrode-waveguide boundary is prescribed with "potential" of 1 volt boundary condition and the "ground" with period of SAW wavelength. Receiving IDTs electrode-waveguide boundaries are periodically prescribed with "ground" and "float potential" boundary conditions. The periodicity of receiving electrodes is also wavelength fold. The microfluidic structure is placed directly above receiving IDTs, the same way as it was performed in two dimensional numerical simulations.

The prime aim of theoretical work is to investigate the novel concept of the SAW based phononic crystal sensor approach completed as an array of periodically placed microfluidic channels. It is not targeted to find the optimal structure design, rather to concentrate on the arrangement that is found to be optimal as a result of two dimensional simulations and deepen the understanding of its behavior, mechanism of coupling of surface wave to the structure and the wave localization. The analysis of the structure response on variation of properties of liquid domains affords to estimate the structure performance as a liquid sensor. The analysis of the structure response on variation of geometry and material properties provides an understanding of possible divergence between theoretical and experimental results.

3.2. Analysis of coupling of surface wave to the periodic arrangements by means of excitation of structure mode

The study of the coupling of incident surface waves to solid periodic arrangement by means of excitation of certain structure mode was completed omitting the liquid domains of the microfluidic structure. Despite the fact that introduction of the liquid changes the structure resonance behavior, the analysis of interaction of solid structure with incident surface wave provides initially more understanding regarding the coupling

mechanism. Previously published works demonstrate an efficient coupling of the guiding acoustic and electromagnetic waves to the defects of the periodical arrangements exciting localized defect modes. The approach of coupling of optical waveguide modes to the photonic defect mode resonator was utilized for studying of opto-mechanical coupling effects [79]. The effects of coupling of guided modes to the defects of phononic structure exciting the defect cavity mode were shown in [80]. In current structure arrangement the wave is localized within the surface of the waveguide of piezoelectric substrate and couples to the periodic structure at specific structure modes. In this arrangement, the periodic structure interacts with the guided surface wave by means of coupling and is not directly probed in terms of transmission or reflection. The periodic arrangement can be considered as a composite structure that has certain resonances. In current case it acts as a standing alone resonator (or set of resonators) that at the certain wavelength concentrate within the structure the acoustic energy of guided surface waves. Each of this composite structure resonance modes in this case can be considered as a separately coupled to the transmission line resonator.

The basic operational principle of the the sensor system is based on the coupling of an incident surface wave to the structure and excitation of a structural mode. The efficient coupling is one of the major requirements. As it was previously shown, structuring of acoustic waveguide as well as placement of the periodic structure atop of the waveguide can cause a considerable scattering of the incident acoustic wave into the waveguide volume. To analyse the interaction of the surface wave with the solid structure, the model was reduced to piezoelectric and elastic material domains, neglecting liquid domains. Separating the computational tasks to several simulation models allow to distinct the mechanisms of interrogation of surface waves with periodic microfluidic arrangement. The prime aim of current numerical simulations is to study the coupling of the incident surface wave and the structure. The numerical simulations were performed with piezoelectric module of COMSOL^{TM} Multiphysics FEM simulation tool.

Coupled to the periodic structure surface acoustic waves have to excite the structural resonances that should correlate to the structure eigenmodes. For that reason the eigenmodes analysis was completed in the frequency range of efficient SAW excitation for the periodic structure separately from the piezoelectric waveguide. The analysis was completed with the bottom boundary fix constrained at IDT areas that corresponds to

complete structure design. The arrangement was prescribed with periodic boundary condition in Z direction. The analysis revealed several possible structure vibration modes. The ones that are close to the central frequency of SAW are demonstrated in Figure 3.6.
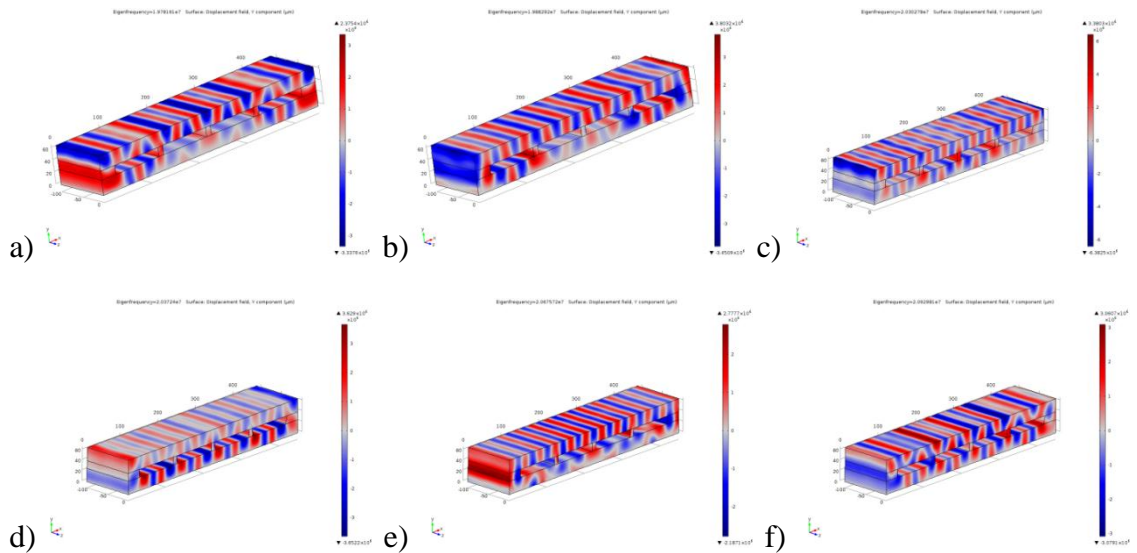
Figure 3.6. Y-component of the displacement field for eigenmodes of the periodic structure found in a frequency range near 20 MHz with fix constrained bottom structure surface at the IDT boundaries. Frequencies of structure modes are: 19.78161 MHz a); 19.88292 MHz b); 20.30278 MHz c); 20.3724 MHz d); 20.67572 MHz e); 20.92981 MHz f).

Each of defined eigenmodes can presumably be excited within the periodic arrangement depending on the excitation conditions. In current case the structure is excited with the surface acoustic wave that has a continuous phase distribution along the bottom boundary of the structure. The predefined in computational model piezoelectric waveguide material properties support efficient coupling of applied electric field to the Rayleigh surface acoustic wave.

Analysis of surface displacement taken from the top structure boundary Figure 3.7 confirms the significant amplitude displacement raise at nearly the same frequencies where the structure eigenmodes were found.
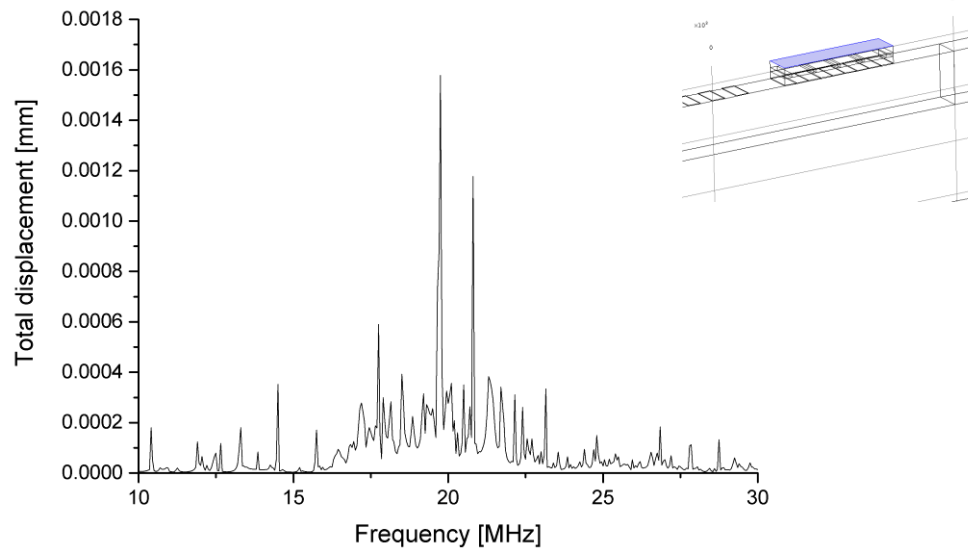
Figure 3.7. Frequency dependence of total displacement at the boundary atop of the structure (shown in an inset)

Despite the fact that eigenmodes analysis revealed existence of various structure modes, results shown in Figure 3.7 demonstrate that only several of such structure modes are pronounced. The most evident displacement maximum is found at the frequency of 19.7 MHz that correspond to the structure eigenmode revealed at frequencies 19.78161 MHz (Figure 3.6 a). Another well-defined structure displacement maximum is found at frequency 20.55 MHz. that matches to the eigenmode frequency at 20.67572 MHz. Possible frequency deviations between eigenmode frequencies and structure displacement maxima are explained by the extension of the eigenmode computational model with piezoelectric domains that changes the structure fixed constrained boundary condition to electrode - structure interface. At the same time the finite discretization step (in current simulation is 50 kHz) of completed computations in a frequency domain also introduces the mismatch of obtained frequencies. In order to get more insights, the most pronounced extremes of structure displacement frequency dependence are separately analyzed with respect to a displacement field distribution and kinetic energy density.

The structure displacement maximum at frequency 19.7 MHz demonstrate a rather complex displacement distribution with a strong wave concentration within a top and a bottom layers of the structure Figure 3.8.
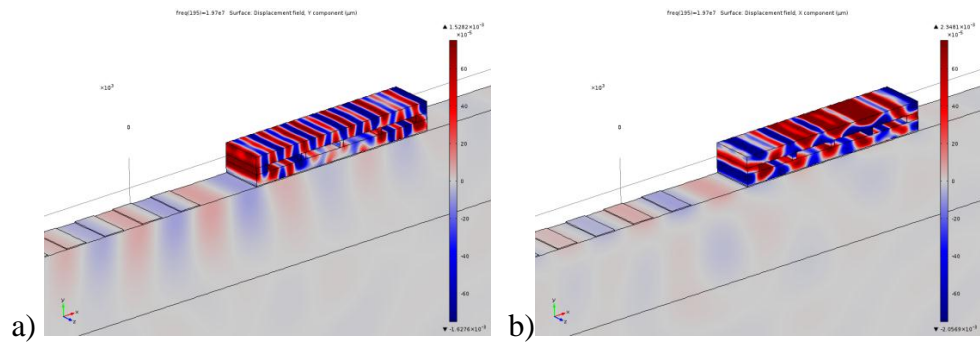
Figure 3.8. Displacement field at frequency 19,7 MHz, Y-component a) and X-component.

Demonstrated in Figure 3.8 results exhibit strong concentration of incident wave within the periodic structure with almost absolute absence of scattering of the wave into the waveguide volume. Analysis of kinetic energy density shown in Figure 3.9 demonstrates that most of the kinetic energy of incident surface wave is concentrated within the structure with only a small portion that is reflected back to the waveguide, Figure 3.9 a).
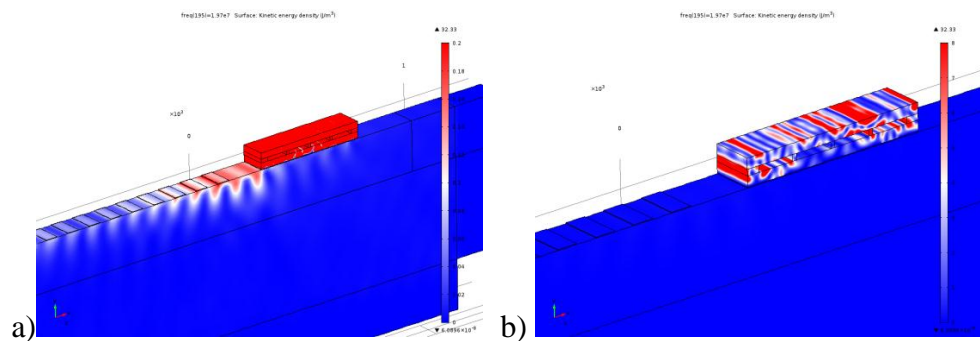
Figure 3.9 Kinetic energy density distribution at the SAW excitation frequency 19.7 MHz for the complete computational model scale a) and for the structure separately b) (adjusted scale).

The kinetic energy distribution also does not demonstrate the observable scattering of the incident surface wave into the volume of the substrate. It is seen that most of the incident wave kinetic energy is concentrated in the structure with only small portion that is transmitted along the piezoelectric waveguide. The kinetic energy density analysis that is observed within the structure (Figure 3.9 b) confirms rather complex

distribution. This observation comes together with computational results of structure displacement.

The higher frequency structure displacement maximum found at the frequency 20.55 MHz (Figure 3.7) has lower amplitude but it is more narrow in comparison to the one that is found at 19.7 MHz. The results of displacement field distribution analysis demonstrated in Figure 3.10 show the excitation of structure mode with considerable transmission of an incident surface wave along the waveguide.
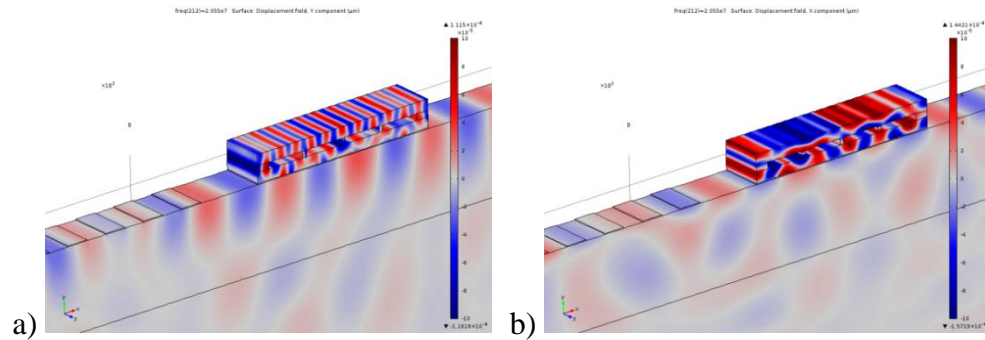
Figure 3.10. Displacement field at frequency 20.55 MHz, Y-component a) and X-component b).

Analysis of kinetic energy density shown in Figure 3.11 demonstrates that at the frequency 20.55 MHz the structure still concentrates the part of the energy, but in following case, more considerable energy reflection is observed. At the same time, part of the energy of incident SAW is transmitted along the waveguide of the structure, Figure 3.11 a).
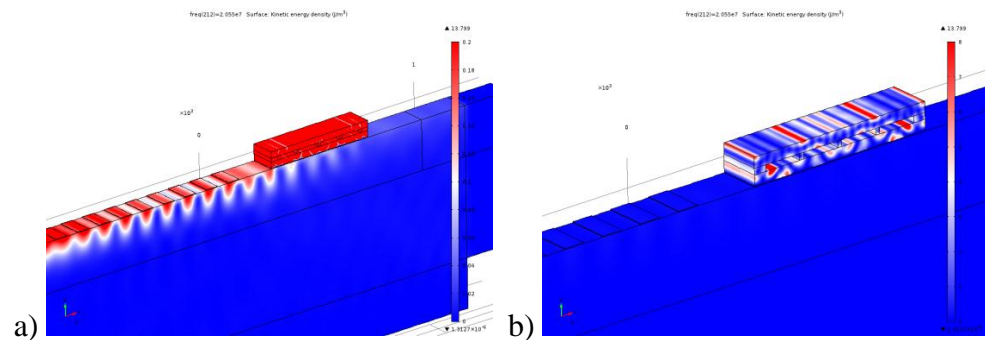
Figure 3.11. Kinetic energy distribution at the SAW excitation frequency 17.8 MHz for the complete computational model scale a) and for the structure separately b) (adjusted scale).

The kinetic energy density analysis demonstrates rather symmetrical distribution within upper layer of the structure and has a relatively complex pattern at the bottom layer of the structure, Figure 3.11 b). Scattering of incident wave into the waveguide volume that should appear as a volume distribution of kinetic energy is not observed similar to a previous case.

Analysis of one of the lower frequency displacement maximums that was found at frequency 17.8 MHz (Figure 3.7) demonstrates a contrast structure behavior in comparison to previous observations, Figure 3.12.
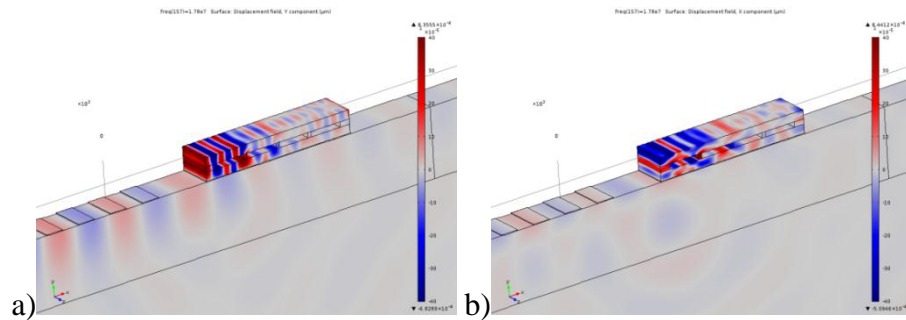
Figure 3.12. Displacement field at frequency 17.8 MHz, Y-component a) and X-component b).

In current case the coupled to the structure surface acoustic wave is significantly attenuates within two lattice periods with rapid amplitude decay after the first channel. The reason for such considerable wave attenuation is the destructive interference of propagating with different phase acoustic waves within the bottom and the top layers of the structure. The phase difference between the waves in the top and the bottom layers of the structure can be explain by the delay between coupling of incident surface wave to the top and the bottom layer of the structure. The kinetic energy density analysis displays that at the frequency 17.8 MHz (Figure 3.13), most of the energy of incident surface wave is scattered back to the waveguide.

Figure 3.13. Kinetic energy distribution at the SAW excitation frequency 17.8 MHz for the complete computational model scale a) and for the structure separately b) (adjusted scale).

Behaviour of the structure at this frequency can only be circumstantually affected by the presence of the liquid and is irrelevant considering liquid sensor application.

Analysis of the structure displacement revealed two separate frequencies at which the structure couples efficiently the incident surface acoustic wave and exhibit the structural resonance of complete microfluidic arrangement. In order to analyse the complete arrangement response, the displacement spectrum taken from the piezoelectric waveguide boundary of receiving IDTs was analysed. The results shown in Figure 3.14 demonstrate two curves, the displacement response without the structure (Figure 3.14, black) and with an integrated periodic arrangement.
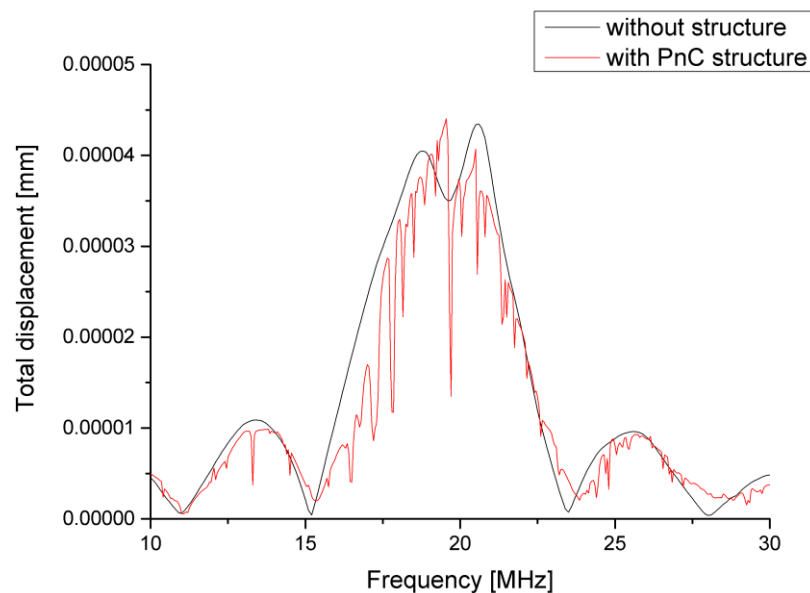
Figure 3.14. Frequency dependence of total displacement taken from the waveguide boundary (shown in an inset as a blue area)

As it can be seen in Figure 3.14, the narrow band frequency regions of rapid amplitude decay (transmission dip) correspond to structure resonances at which the incident surface acoustic wave is concentrated within the structure. The measuring scheme for the microfluidic arrangement in current case should be focused on the detection of

transmission dips at specific frequencies where most of the incident wave is coupled by the structure and isolated as a composite arrangement resonance mode.

3.3. Analysis of liquid contained sensor structure

For the sensor purposes it is advantageous to control the position of transmission maximums (or minimums) in contrast to the detection of the variation of the bandgap. Infinite periodic structures are subjected to exhibit a bandgap for a certain wavelength region and appearance of localised resonances in those structures is possible to achieve only with symmetry disruption. The finite structures on the other hand are able to exhibit the structural resonances in rather uniform periodic arrangements. In this case the complete regular periodic arrangement within its finite dimensions with prescribed boundaries supports the resonance structural modes at certain wavelengths. Behaviour of finite composite arrangements was previously analytically described in [81]. It was shown that for the two dimensional arrangements as well as for one dimensional case, the free boundaries cause local resonances that affect the response within the bandgap. Another work has shown that the local resonances in structure constituent contribute in arrangement response. In [82] the study of periodical pillars arrangement integrated to SAW device revealed that low frequency bandgap arises because of local resonances in the pillars. At the wavelength of localised resonance, the acoustic energy of incident surface wave is strongly confined in structure constitutes (pillars).

In order to investigate an ability of liquid containing periodic arrangement to exhibiting the structural resonances, the study of displacement/pressure field and energy density distribution were completed. Previously demonstrated coupling within solid domain of the structure has demonstrated that at certain frequencies that correspond to structural resonances, the acoustic energy is strongly concentrated within the structure. In transmission spectrum of complete arrangement that can be read as transmission minima (transmission dip). An appropriate periodical arrangement allowed to reduce the number of supported structure modes, and achieve an isolation of several more pronounced resonances. In current case the periodic composite arrangement consist of polymer microfluidic structure with the channels that are defined as liquid domains.

To complete the computation task, the liquid was described as independent domains with a pressure acoustic model. The computational model was extended to complete a

simultaneous simulation for piezoelectric, linear elastic and pressure acoustic domains. The simulations were performed with previously described structure geometry. Liquid domain applies the material data of deionized water with speed of sound 1500 m/s. The simulation results of liquid filled structure in conjunction with SAW transmission dependence are shown in Figure 3.15.
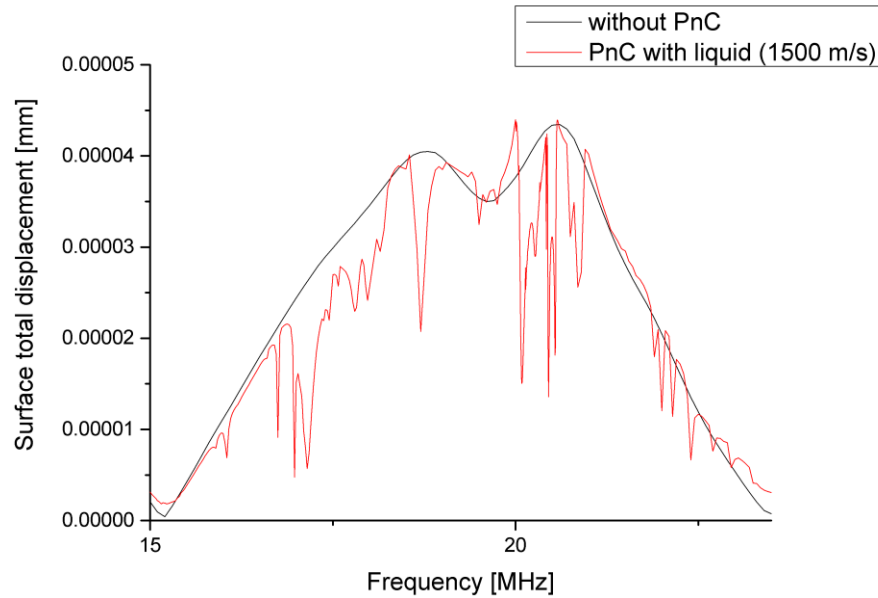
Figure 3.15. Frequency dependence of surface displacement taken from вуеусештп boundary of the waveguide for the SAW structure without periodic arrangement (black) and for the integrated liquid filled microfluidic arrangement (red).

Shown in Figure 3.15 dependences demonstrate that the integrated microfluidic arrangement considerably influence the displacement spectrum with various displacements minima that can be attributed with different effects. In order to define the most relevant in terms of liquid sensor application, the study of structure response depending on material properties of liquid was completed.

Displacement response with liquid domain specified for microfluidic channels taken from the detecting waveguide boundary for three different speed of sound values was analyzed and shown in Figure 3.16. The liquid density was defined as 1000 kg/m^3 and kept constant for completed simulations.
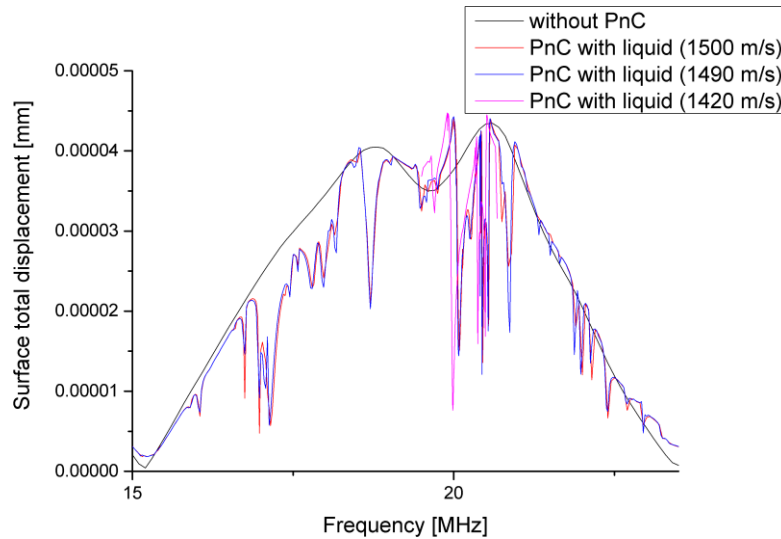
Figure 3.16 Frequency dependence of surface displacement taken from the detecting waveguide boundary.

Demonstrated simulation results revealed the frequency region within which the simulation model response demonstrates variation of displacement spectrum depending on the speed of sound of liquid domains. The frequency region of structure response where the influence of liquid material properties is more pronounced was studied with more precise frequency discretization step and the results are demonstrated in Figure 3.17.
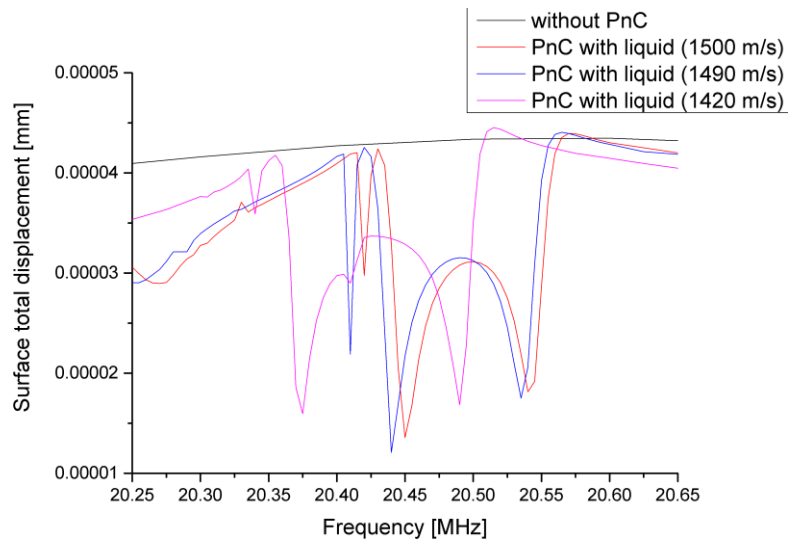
Figure 3.17 The frequency dependence of a surface displacement taken from the detecting waveguide boundary for three different values of speed of sound prescribed for liquid domains.

As it shown in Figure 3.17, the structure displacement response has several displacement minima with two of them that are more distinctive. The frequency of that displacement extremes are affected by the varied speed of sound of liquid domains. For the case of liquid with speed of sound 1500 m/s, the displacement pattern and pressure distribution in microfluidic channels of presented in Figure 3.17 minima were analyzed. The results are shown in Figure 3.18.
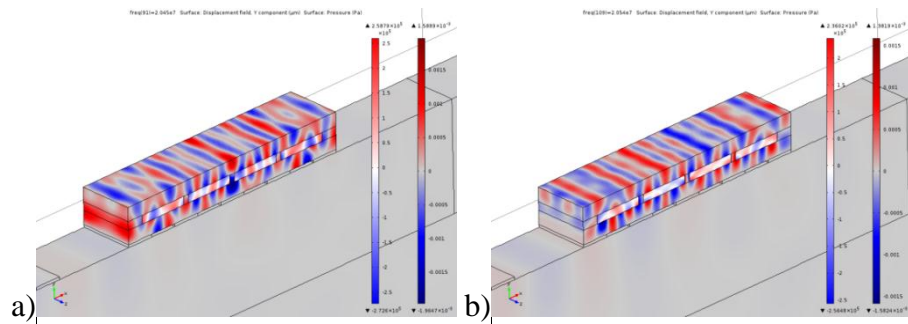
Figure 3.18 Displacement pattern and pressure distribution for the structure filled with liquid (speed of sound 1500 m/s) at frequency 20.45 MHz a) and 20.54 MHz b)

In both cases the complete arrangement exhibits the complex vibration pattern. The observable modulation of displacement field in Z direction can be attributed to the influence by the resonance mode that appears only in case of infinite boundary condition in Z direction. Omitting the influence of Z component of displacement, the structure pattern in top and the bottom layers is rather regular.

Results of analysis of kinetic energy density distribution for the displacement minima found at 20.45 MHz and at 20.54 MHz are shown in Figure 3.19 and Figure 3.20 respectively.
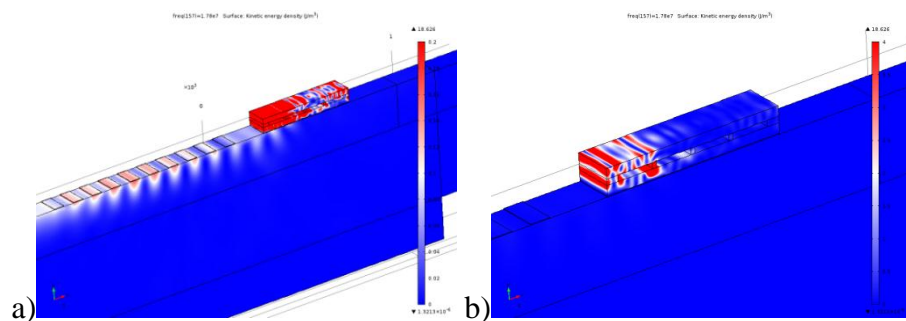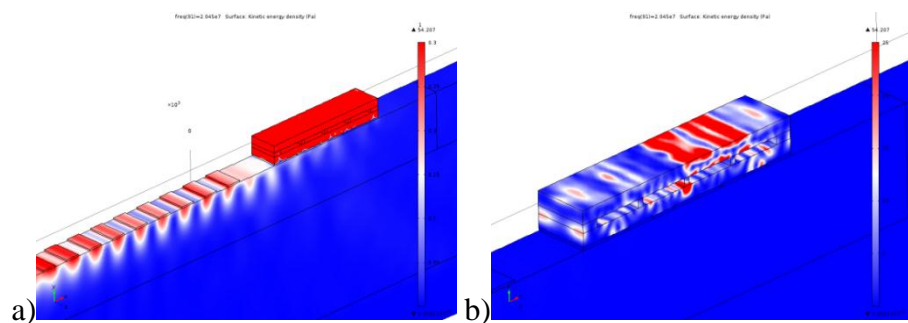

Figure 3.19. Kinetic energy density distribution at the SAW excitation frequency 20.45 MHz for the complete computational model scale a) and for the structure separately b) (adjusted scale)
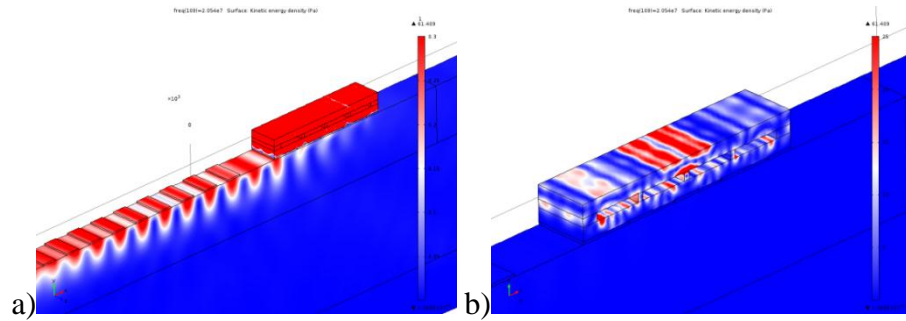
Figure 3.20. Kinetic energy density distribution at the SAW excitation frequency 20.54 MHz for the complete computational model scale a) and for the structure separately b) (adjusted scale)

The kinetic energy distribution demonstrates the behavior that was previously observed for the solid structure case. At specific frequencies at which the displacement minima taken from the waveguide detecting area is observed, the structure concentrates the energy of incident surface wave.

The microfluidic structure as a composite arrangement with finite dimensions supports an existence of structure resonance modes. These resonance modes can be attributed to the structure eigenmodes. In order to study the vibration modes of liquid filled arrangement separately from the waveguide, the eigenmode analysis of composite microfluidic structure that is fix constrained at IDT boundaries was conducted. Obtained computational results revealed two different eigenmodes (Figure 3.21) that with some approximation can match the observed resonance modes.
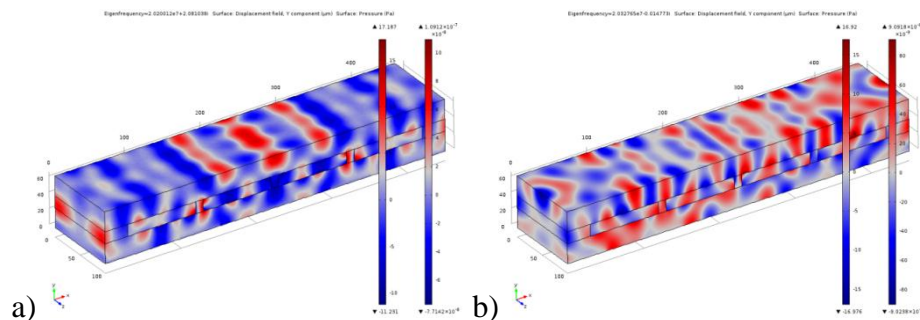
Figure 3.21. Displacement and pressure distribution of liquid containing structure at frequencies of eigenmodes 20.20012 MHz a) and 20.32765 MHz.

Despite the fact that a displacement field distribution at structure periphery is strongly affected by the displacement components in Z direction and is hardly matchable with

observable in Figure 3.18, the central part of the structure for both eigenmodes mostly repeat the displacement layout. Considering previously obtained simulation results for eigenmodes in solid periodic arrangement, they provide more distinct displacement distribution that can be brought together with obtained for complete arrangement results (Figure 3.22 and Figure 3.23).
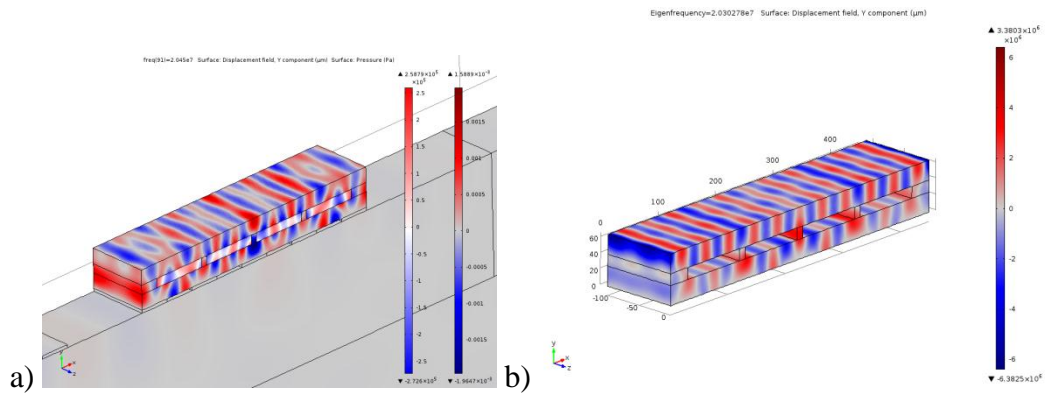
Figure 3.22 Displacements pattern of the PnC structure with SAW at frequency 20.45 MHz a) and PnC eigenmode displacement pattern at frequency 20.30278 MHz b)
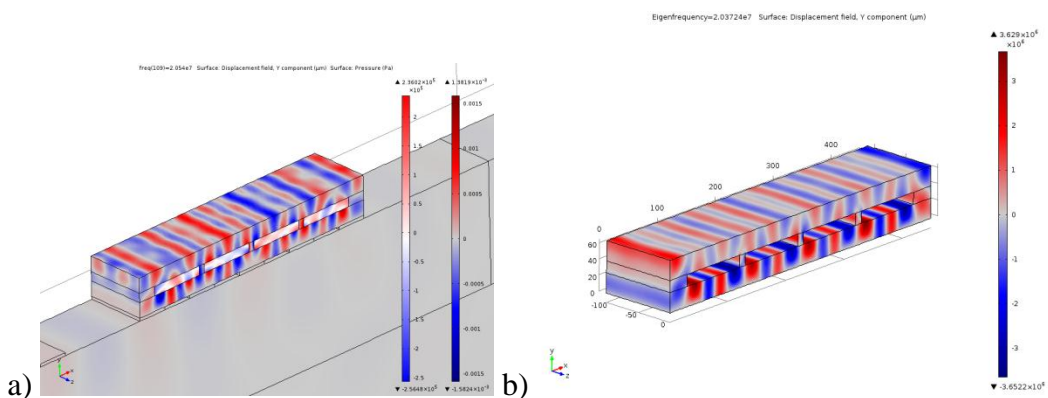
Figure 3.23 Displacements pattern of PnC structure with SAW at frequency 20.54 MHz a) and PnC eigenmode pattern at frequency 20.3724 MHz b)

In both demonstrated cases, the SAW waveguide integrated structure demonstrates less regular displacement field distribution. The disturbance of displacement pattern with an appearance of Z component of displacement can have several reasons. The phase shift between the propagating structure perturbations within top and bottom layer of the structure initiates non-uniform pressure distribution within the liquid domains that as a result can distort the displacement field in both layers. On the other hand, the

computational error for liquid-solid domains accumulated as a result of applied in Z direction periodic boundary conditions can also introduce the disturbance of displacement field distribution.

Along with speed of sound, the influence of density variation of liquid domains on displacement spectrum variation was analyzed. The obtained computational results are demonstrated in Figure 3.24.
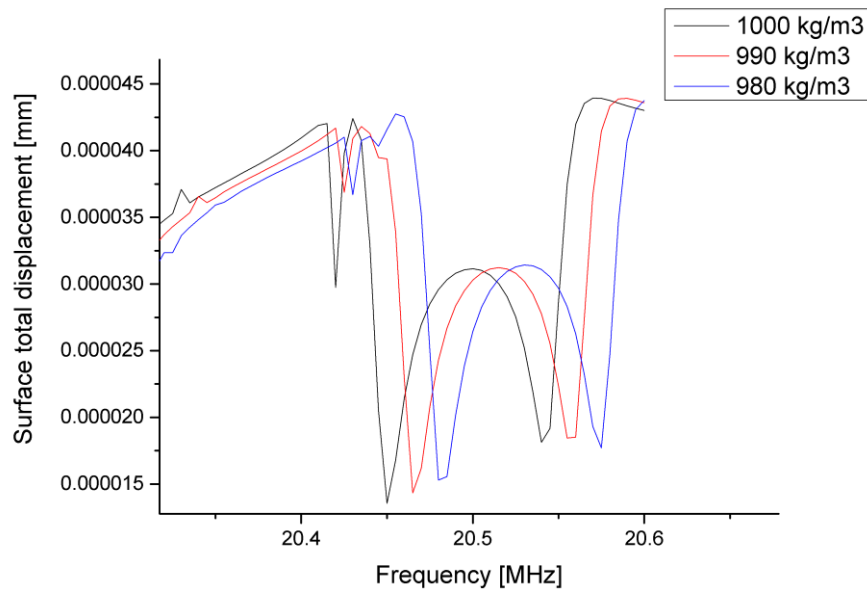
Figure 3.24. The frequency dependence of a surface displacement taken from the detecting waveguide boundary for three different values of density of liquid domains

The variation of density causes a gradual shift of the displacement dependence taken from the detecting boundary of the waveguide of the structure.

Completed simulations have shown the influence of material properties of liquid domain on the structural resonances of complete arrangement. Variation of density as well as the speed of sound of one of the constituents of composite periodic arrangement affects the resonant properties of the complete structure. Obtained results demonstrate that only several specific structure modes are sensitive to variation of material properties of liquid. The detection scheme remained as it was described in previous chapter for solid arrangement. The observed computational results of eigenmode analysis revealed an existence of structure eigenmodes that are similar to displacement distribution obtained for the SAW excited case.

Structure vibrations that are found in a transmission spectrum of the main transmission band show various structure modes that are isolated from being scattered into the bulk. The efficient coupling of the surface wave to the structure appears at the structure resonance mode. The kinetic energy density distribution analysis has shown that at the structure resonance frequency, the energy of incident surface wave is concentrated mostly within the structure. Because the speed of sound in polymer is more than twice lower than in lithium niobate, the corresponding wavelength in polymer structure is more than twice shorter than in a lithium niobate waveguide. The wavelength mismatch, as a result, does not support the recoupling of the structure modes back to the surface wave that allows obtaining the high concentration of incident wave within the arrangement. The specific frequencies at which the composite polymer-liquid arrangement exhibits the structural resonance can be read as transmission minima.

3.4. An influence of material parameters and geometry on the structure response

The fabrication process is associated with adjusting of a considerable number of technological parameters that influence directly the final structure performance. It was shown in [83] that the processing of SU-8 layers is associated with adjustment of almost 30 different technological parameters. They may result in mechanical properties of SU-8 layers different to those applied in the simulations. For example, it was shown in [20], that the modulus of elasticity can vary in a considerably broad range of $2.92 - 4.95$ GPa. Therefore it is necessary to investigate the influence of modulus of elasticity on structure response. In order to remain within the same frequency range, the deviation of modulus of elasticity was taken as 1%. The simulation results of structure response on modulus of elasticity change are shown in Figure 3.25.
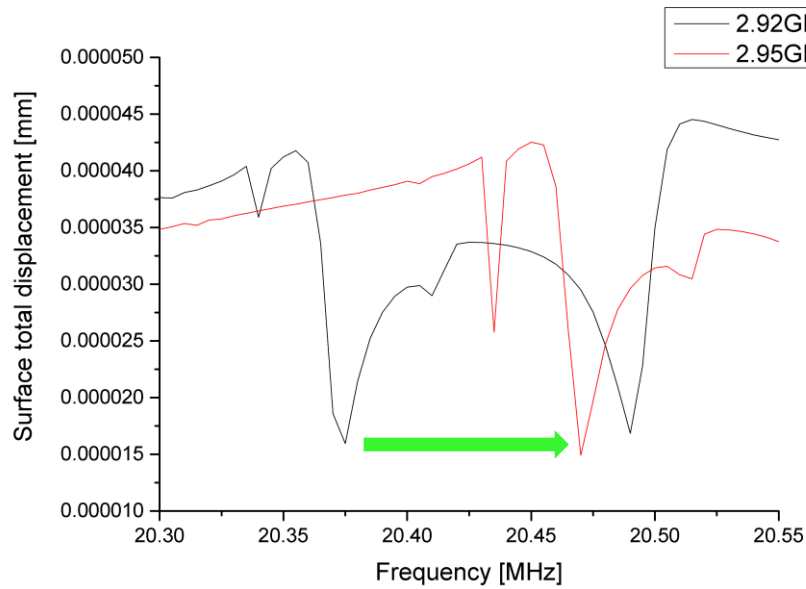
Figure 3.25 Influence of modulus of elasticity variation on the sensor response. The structure in both cases is filled with liquid (speed of sound – 1420 m/s; density - 1 kg/m³)

An increase of modulus of elasticity shifts the structure resonances to a higher frequency by 90 kHz which is approximately three times larger than the frequency shift caused by 1% change in speed of sound.

In order to validate quantitatively the influence of geometry on sensor response, the simulations with variable channel thickness, as well as interface and cover layer thickness were performed. Results of sensor response for three different channel thicknesses are demonstrated in Figure 3.26.
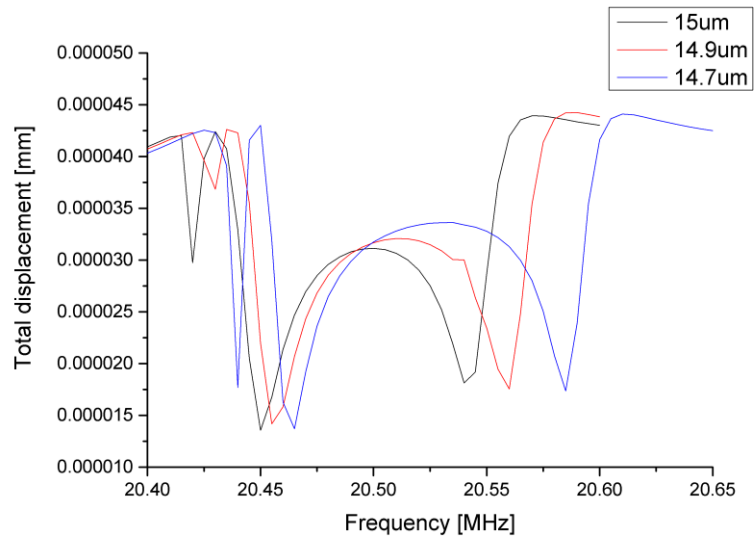
Figure 3.26 Numerical simulation results of channel thickness variation and its influence on sensor response.

The reduction of microfluidic channel thickness causes shift of transmission minima to higher frequencies, however, they do not equally move upwards. In consequence, the distance between these two minima can be different from the theoretically predicted one.

Along with a possible deviation of microfluidic channel, the thickness of interfacial and covering SU-8 layers can vary the position of observed minima. In order to quantitatively investigate the influence of each layer thickness variation, the simulations were performed for interfacial layer and covering top layer separately with a thickness change of 1%. The Figure 3.27 demonstrates the influence of a top covering layer thickness variation.
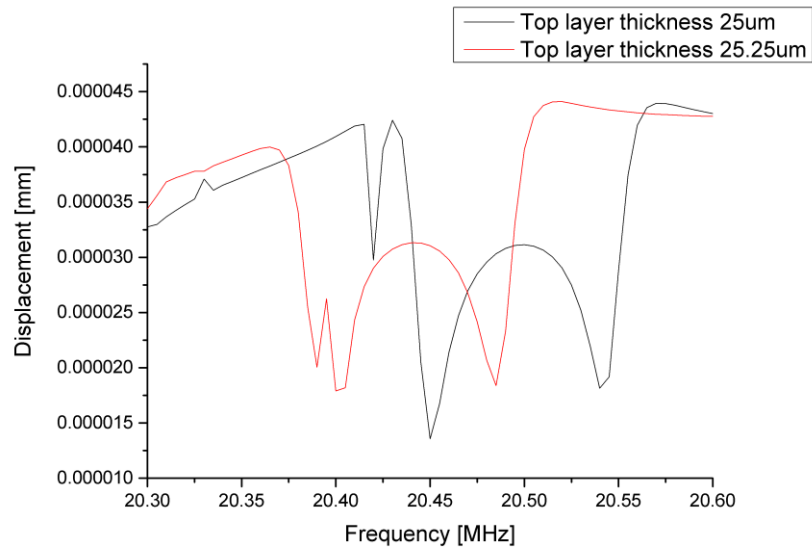
Figure 3.27. PnC structure top layer thickness variation.

As it can be seen, the alteration of the top layer thickness by 1% significantly varies the position of observed minima. The thickness increase causes a shift of both minima to a lower frequency region as it demonstrated in Figure 3.27.

The variation of the the bottom layer thickness by 1% also causes a downshift in the frequency for both minima, but, in comparison to the frequency decrease that is observed for the top layer, the alteration of the interfacial layer is less pronounced, Figure 3.28.
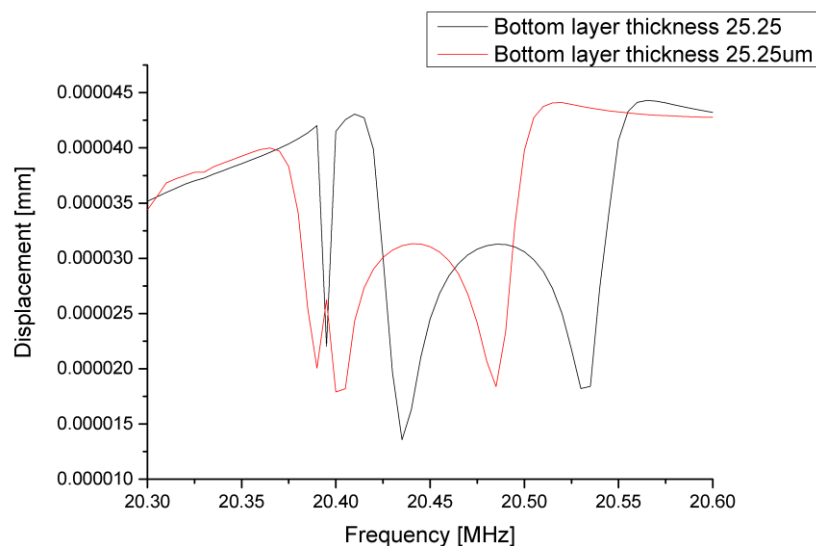
Figure 3.28 PnC structure bottom layer thickness variation.

The observed frequency changes can be explained as consequence of an increased structural element dimensions that causes the downshift of structure eigenmodes.

Another critical geometry deviation can appear during microfluidic channel fabrication. Since a considerably thick layer must be structured, deviations from the rectangular cross section are unavoidable in most cases. The influence of a trapezoidal channel shape on structure response should be also considered when theoretical predictions are compared with experimental results. For that reason, simulations of trapezoidal channel were performed and obtained results are demonstrated in Figure 3.29.
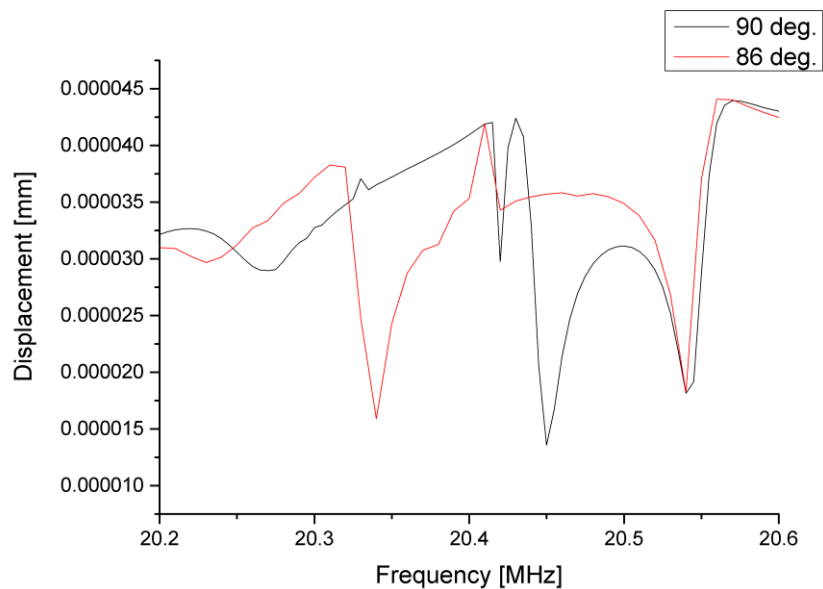
Figure 3.29. Influence of microfluidic channels sidewalls inclination on the structure response. Case of vertical sidewalls is marked as 90 deg. The structure inclined by 4° from vertical shape described as 86 deg. (trapezoidal shape with channel width at the top of the channel broader than at the bottom).

As it can be observed, a deviation from the rectangular shape causes a shift of the lower frequency minimum and almost does not disturb the higher frequency one. The displacement pattern remains similar for both minima in each case. The microfluidic layer is a coupling layer between top and bottom layers of the structure. As it was previously shown, the higher displacement dip is associated with the structure mode that is more localized in a bottom layer rather than on the top. An introduction of inclination does not affect the interface of the bottom (interfacial) layer and microfluidic layer. It is observed as a low influence on a higher frequency resonance.

On the other hand, the inclination of the structure within the microfluidic layer varies the boundary of microfluidic and top covering layers. This change causes a significant shift of the low frequency displacement minimum.

According to manufacturing process, the final structure should have an absence of the contact with the waveguide surface or exhibit a low adhesion attachment. Considering that following boundary can bring an uncertainty regarding existence of acoustic contact that is appeared as a result of technological deviations, the PnC structure directly attached to the waveguide surface was numerically simulated. Results are demonstrated in Figure 3.30.
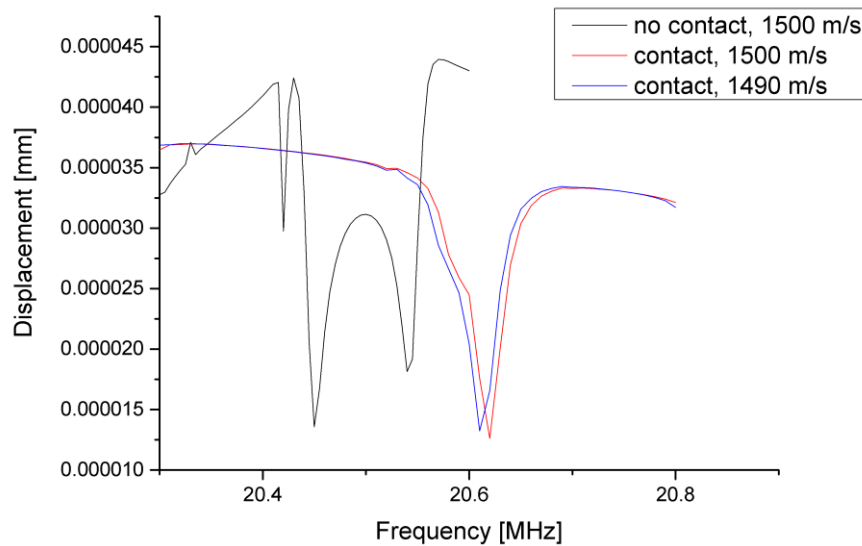
Figure 3.30 Effect of PnC structure acoustic contact to waveguide surface of SAW structure.

Figure 3.30 demonstrate that existence of acoustic contact significantly influence the structure response. The structure-waveguide acoustic contact changes the structure behavior causing the shift of two separate displacement minima to a single coupled transmission dip. The displacement and pressure distribution shown in Figure 3.31 taken at the frequencies 20.58 MHz and 20.62 MHz for the case when the structure and the waveguide are in acoustic contact, revealed the existence of the similar structure modes that were previously observed for the isolated by the electrodes arrangement.
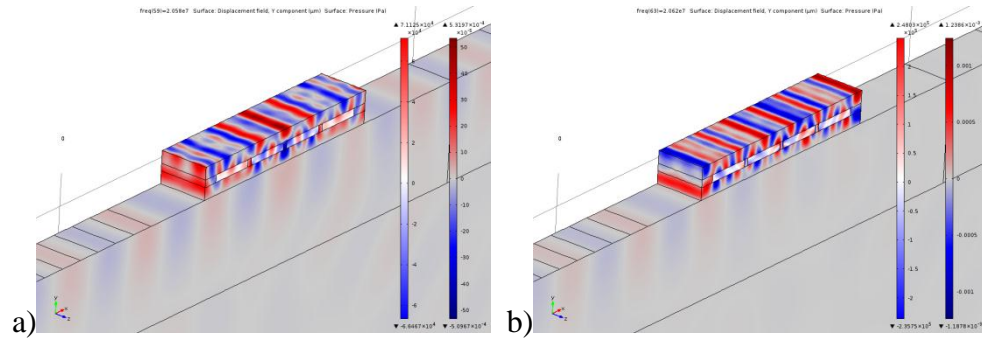
Figure 3.31. Displacement and pressure field distribution taken at frequencies 20.58 MHz and 20.62 MHz for the case when the structure and the waveguide are in acoustic contact.

Theoretically investigated influence of geometry and material properties completed on a basis of the developed PnC sensor model is demonstrated that both material properties and geometry can vary the position of sensor minima on a frequency scale. The relative deviation of parameters (1-3%) showed only the shift of minima without their significant disturbance or deterioration. The obtained theoretical results afford to bring together the theoretical predictions and experimental results considering the influences of deviations of material properties and geometry tolerances of fabricated structures.

4 FABRICATION

This chapter is focused on detailed description of the fabrication process of developed sensor structure. The technological processes were completed by the author at Otto-von-Guericke University clean room facilities in Magdeburg. Design of the process and necessary supporting instrumentation, such as photomasks design, process separate programs and etc., have been done by the author as well. The fabrication of SAW structures as well as SU-8 processing were not previously established processes that were developed from the scratch within this work. Despite the fact that separate standard processes, mostly for silicon and glass wafers, were previously established in university clean rooms, in most cases they cannot be used for strong ferroelectric substrates, such as lithium niobate. The direct application of non-optimized processes causes a wafers brakeage because of strong piezo and pyroelectric properties. This results in necessity to change of almost each single technological step of the sensor fabrication.

In current work we demonstrate the challenges and solutions of the SAW based phononic crystal sensors fabrication. The manufacturing process can be separated to several parts such as manufacture of IDTs, fabrication of the opened periodic microfluidic structure and encapsulating of the channels. Performance of the structure plays a significant role in the sensor response that leads to restricted fabrication tolerances. As a basis for microfluidic arrangement realization, the SU-8 polymer based technology was applied. Chemically stable against most of solvents, epoxy based SU-8 photoresist was previously recognized as a promising solution for building microfluidic

structures. Despite the advantages of this polymer, its usage is associated with the adjustment of up to 30 fabrication parameters of respective technological process in order to achieve designed structures. The utilization of the SU-8 adhesive bonding is an advantage of that polymer, but in order to achieve a sufficient bonding quality, the manufacturing process should be optimized for a certain structure design. In following chapters, the detailed description of each separate fabrication process and achieved results are provided.

4.1. Technological challenges of sensor manufacturing

Designed SAW based phononic crystal sensor structure is shown in Figure 4.1. It is featured with an array of periodically placed electrodes (IDTs) for excitation and reception of acoustic waves and microfluidic structure completed as a system of periodically arranged closed microfluidic channels.
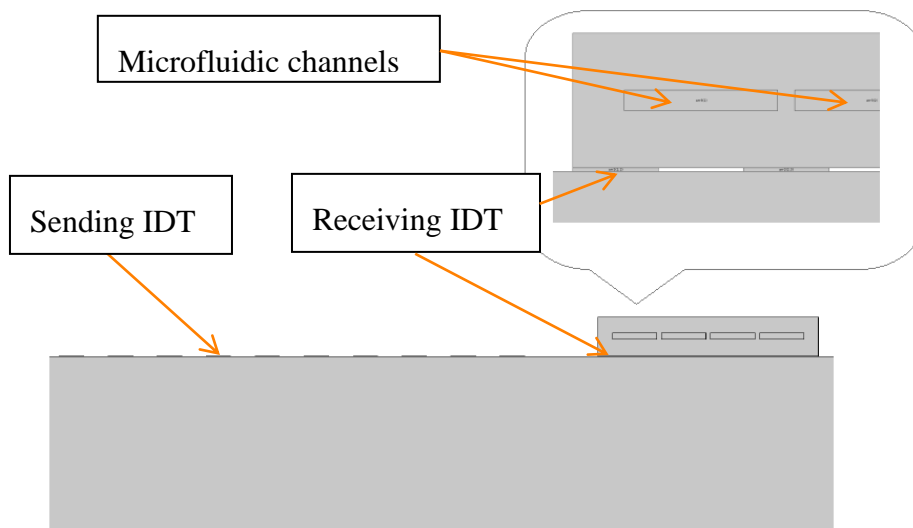
Figure 4.1 Designed SAW based phononic crystal sensor structure

The manufacture of designed structure can be completed within different approaches. By principle, all possible manufacturing processes can be split into a solid state based or a polymer based ones. Technology that is based on a solid state approach introduces several advantages such as high long term mechanical stability and application of well-established processes. However, for a demonstrated sensor design, this approach could be complicated to utilize for the sensor fabrication. On the other hand, the polymer

based technology opens an opportunity for a rapid prototyping at relatively low cost and allows simplifying technological process in general. Among all possible polymer based solutions that can be based on Polyimid, PDMS, PMMA or SU-8, chosen approach must satisfy initial design demands. At the same time, the respective technology should be adjusted in a way to obtain the expected sensor structure performance.

The SU-8 negative photoresist is currently widely applied as a construction material for microfluidic devices, sensors and other applications. Due to the number of advantages, such as chemical stability to most of fluids, controllable mechanical properties through the crosslinking process management, this photoresist can be applied for building microfluidic structures for a variety of different applications [84]. Initial approaches for creating closed microfluidic structures that are based on prescribed in SU-8 datasheet [85] processing parameters have shown an evident necessity for changes. Completed closed microfluidic structures with standard parameters featured by a low percentage of a bonded area and a high fragility [86]. In order to achieve a mechanical performance that is required for a designed sensor, technological parameters of SU-8 processing should be reconsidered. Previously, an influence of SU-8 processing on its mechanical properties were studied [83,87–89]. Moreover, it was demonstrated that considering a certain application, SU-8 layer can be differently manufactured in order to fulfill predefined requirements. Due to staged SU-8 processing, the number of variable technological parameters that directly influence the final SU-8 layer performance can exceed thirty [83].

The study of an influence of tensile properties of coated SU-8 layers has demonstrated that an increase of SU-8 curing temperature significantly changes mechanical properties of SU-8 layers [87]. It was shown that high temperature curing of SU-8 during post exposure bake (PEB) and hard bake (HB) makes layers much more fragile. Previously published results [88] have shown that changes in SU-8 processing can considerably influence following SU-8 crosslinking. It was demonstrated how soft bake conditions, an exposure dose and post exposure bake parameters influence on resolution and crack formations caused by inner SU-8 film stress accumulated during the processing of SU-8 layers. In [83] it was shown that at low soft bake temperature exposed SU-8 polymerizes at faster rate with the reduced stress. Completely crack free structures with

aspect ratios of 10 and 8 for trench and ridge structures have been achieved with the soft bake temperature of 65 °C.

In order to complete closed microfluidic channels, the SU-8 adhesive bonding process should be performed. In this case, the SU-8 polymer crosslinking reactions of bonding layers should be taken under control to achieve a high bonding quality. It was already shown that in order to achieve a sufficient bonding strength, it is necessary to apply the wafer with incompletely cross-linked SU-8 in order to perform a final mutual crosslinking step during the bonding process. At the same time, SU-8 should be sufficiently cross-linked to complete developing process. In publication [86] it was demonstrated how to achieve closed microfluidic structures with SU-8 adhesive bonding applying fully processed and only soft baked SU-8 layers that is followed by exposure during the bonding process. This method requires a utilization of specific bonding equipment that was not available for implementation in current work. Therefore, both SU-8 layers have to be exposed before the bonding process or the bonding process should be completed in a way that allows finalizing the exposure after the microfluidic structure was assembled.

In [90] the adjustment of the technological process for a wafer level adhesive bonding has been completed for the structured SU-8 50 and the adhesive layer made of SU-8 5. It was shown that for high resolution structures with a certain bake-exposure conditions it was possible to achieve bonding of fully processed SU-8 layer and only soft baked adhesive layer, without leakage of SU-8 into the channels. But at the same time the achieved bonded area was reaching only 70 %. In that process, the pre-bake conditions have been set at 95 °C for 20 min for SU-8-50 and 95 °C for 12 min for SU-8 5. Within such pre-bake parameters, final SU-8 layers are expected to be less flexible and more fragile because of low level of the solvent content. The reduction of the pre-bake time could improve the bonding completion area. However, in case of microchannels it was shown that it immediately causes channels blocking [90]. Additionally to that, the application of adhesive layer for bonding processes make it complicated to withstand the demands regarding structure geometry. It is important to have required layers thicknesses with minimal deviations to avoid the deterioration of sensor response. An application of adhesive layer brings geometry uncertainty and makes the fabrication process rather complicated.

In order to produce high resolution microfluidic structures without any SU-8 leakage inside the channels, SU-8 layers that are brought in contact should be exposed before the bonding and at least one of the layers should not be completely crosslinked. The unexposed SU-8 layers may leak inside structures and block channels that lead to impossibility to create the high resolution microfluidic structures. Therefore, the application of unexposed SU-8 requires an adjustment of baking and bonding temperatures. In these cases, when the exposure should be done before the bonding, the level of polymerization has to be taken under control in order to complete the bonding process. According to [91], it was shown that bonding layers should be only partially polymerized for multilayered structures. The exposure dose and the post exposure processing are the steps that define final level of the polymerization of SU-8. In order to complete the adhesive bonding process, it is necessary to have functional groups of the polymer chains on the surface, at least one of the layers. Based on this condition, mutual crosslinking bonds between two bonding SU-8 layers can be initiated. The challenge of that approach is in a necessity of adjustment of almost each fabrication parameter of SU-8 layer processing depending on the thickness of the layer.

In order to complete a multilayer SU-8 microfluidic structures, the appropriate technological recipe for initial layers of structures should be adjusted. The one of the main problems of the SU-8 multilayer structures fabrication is a delamination of bottom SU-8 layers during processing of subsequent layers. Such delamination occurs due to thermal expansion (layer shrinking) and accumulation of a mechanical stress after temperature treatment during processing of already cross-linked SU-8 layers. In order to complete multilayer SU-8 structures, the processing parameters of each subsequent layer have to be adjusted. In this case, SU-8 processing parameters that are recommended by the manufacturer [85] are not applicable. The optimization regarding the post exposure bake (PEB) has been already proposed in [89] for the multilayer structures. In this case, first SU-8 layer should not be completely cross-linked. Only PEB step with 65°C has to be initially performed. The completion of the PEB within second curing temperature step should be made within bake steps of subsequent layers. The short PEB step is sufficient in order to avoid diffusion from subsequently coated layers and keep off the whole top structure from significant shrinkage of handling SU-8 layer under the temperature treatment. However, due to the dependence of SU-8 processing parameters on layer thickness, the already published recipes for multilayer

structures fabrication are not applicable for customized designs. In case of developed sensor structure, technological parameters of each layer fabrication have to be manually defined.

Summarizing, it should be stated that almost each technological step of the designed structure manufacturing should be developed from scratch or reconsidered in case of recommended or already established processes.

4.2. Materials and equipment

For the fabrication of sensor structure, following materials were utilized. Titanium and aluminum targets were used in physical vapor deposition (PVD) sputtering process and were supplied by the local manufacturer. Structuring of metal layers was completed applying TI35ES positive photoresist in conjunction with TI Prime adhesive promoter that were supplied by MicroChemicals GmbH. AZ and AZ400K photoresist developers as well as acetone, isopropanol, ANPE aluminum etcher and other supplies were ordered from Carl Roth GmbH and Sigma-Aldrich Chemie GmbH. Applied for structuring of microfluidic channels SU-8-50, SU-8-5 photoresists and mr600Dev developer were supplied by Micro Resist Technology GmbH.

The deposition of metal layers was completed with LS 500 ES physical vapor deposition equipment. For photoresist spin coating, SUSS Labspin manufacturing line was utilized. The lithography was completed with SUSS_MA6_BA6 mask aligner. Processes of SU-8 adhesive bonding were conducted in SUSS SB6E substrate bonder. Manufactured SAW based phononic crystal sensor was analyzed with Zeiss EVO 50 scanning electron microscope and FTR MicroProf 300 profilometer.

4.3. Technology of IDTs manufacturing

The technological process of the SAW based phononic crystal liquid sensor manufacturing begins with fabrication of efficient surface acoustic wave structures. Referring to the sensor design, lithium niobate ($LiNbO_3$) 128° Y cut with reference flat orthogonal to X axis − the direction of the wave propagation were chosen as a sensor substrate. In order to excite and detect surface acoustic waves, the interdigital transducers (an array of periodically placed metal electrodes with two mutual bars) have to be manufactured on a surface of the substrate. For this reason, within the first

technological steps, a thin film of required metal has to be sputtered on a surface of a substrate. In SAW devices the utilization of aluminum electrodes is a common practice because of an ability to apply a standard wet etching process. Aluminum has good conductive properties and in comparison to silver or gold, it is a cost efficient material. However, despite all the advantages, aluminum has very poor adhesion to most of piezoelectric wafers, including lithium niobate. Due to that, the adhesive layer has to be sputtered prior to aluminum. An application titanium or chrome adhesive layers affords to achieve a sufficient adhesion between aluminum and lithium niobate wafer. However, the thickness of the layer should be reduced to several tens of nanometers to avoid any influence on electrodes conductance and coupling to an acoustic wave. In order to achieve the uniform metal adhesive layer distribution across the whole wafer, the sputtering should be optimized in this particular case. Titanium adhesive layer is a standard solution for the IDTs manufacturing and is used in current work. For achieving a uniform thickness distribution of titanium layer across the wafer, following sputtering feature has to be considered. Usually titanium has a strong oxide layer that significantly reduces the sputtering rate. To reach a uniform distribution, especially of thin films layers, it is necessary to complete a relatively long prior sputtering that ensures the removal of oxide and, as a result, allows achieving the uniform thickness distribution of sputtered adhesive layer. In current work, titanium adhesive layer was sputtered in LS 500 ES physical vapor deposition equipment. The pre-sputtering from titanium target was completed within 8 minutes at 200 watts. Sputtering of the adhesive layer was completed with 200 watts during 60 seconds. Achieved layer thickness was estimated approximately 35-40 nm.

After the deposition of the adhesive titanium layer, the aluminum layer was sputtered within the same vacuum process. In previous chapters, the influence of the electrodes thickness on coupling to the excited acoustic wave was already discussed. In current work, thickness of electrodes was set to 500 nm. Chosen electrodes thickness is not an optimal for SAW devices operating at 20 MHz frequency but it is sufficient to obtain a broad band frequency response and it is convenient for the subsequent IDTs structuring. As well as for titanium target, aluminum also forms a strong oxide on a surface of the target, but it can be removed during 2 minutes of pre-sputtering at 400 watts. A deposition of the aluminum electrodes layer was completed at 400 watts during 5

minutes. The deposition should be made with intervals in order to avoid the lithium niobate wafers overheating that can cause their brakeage.

Aluminum with titanium adhesive layer is a commonly used material for SAW devices electrodes. In current case this approach cannot be directly implemented for the designed structure realization, because aluminum exhibits a very poor adhesion to the SU-8 polymer that has to be deposited atop of IDTs. The low adhesion of the SU-8 multilayer structure can deteriorate the sensor response and can cause the delamination of whole SU-8 multilayer structure during the subsequent technological steps. In publication [92] the adhesion properties of SU-8 that is coated on several metals were investigated. Consequently, it was shown that among most of the metals, the strong adhesion of SU-8 can be achieved on a surface of titanium layers. For this reason, another titanium layer with thickness of 100 nm was sputtered atop of already deposited aluminum layer. The deposition was completed during 3 minutes with a generator power of 200 watts. After the deposition of all described layers, wafers remained in a vacuum chamber for another 30 minutes reaching room temperature to avoid a strong oxidation of deposited metal coatings.

Structuring of deposited metal layers was completed applying a standard photolithography technology using TI35ES positive photoresist and a contact lithography equipment. Within the first step, TI35ES photoresist was spin coated on the wafers with deposited metal layers. Prior to photoresist coating, wafers were baked at the temperature of 140℃ for 10 minutes. In order to improve adhesion of the photoresist, a TI Prime adhesion promoter was initially spin coated and baked at 120℃ for 2 minutes. In order to avoid any rapid wafer temperature change, baking steps were made with temperature ramping. Subsequently, TI35ES photoresist was spin coated on a wafer with manufacturer recommended parameters. The four milliliter photoresist volume was dispensed with the automated dispensing system on a rotating wafer. At speed of 2000 rotation per minute (rpm), the thickness of photoresist was defined close to 2.5 μm. Then, the spin coated photoresist was then baked at 100℃ for 2 minutes and left in a box for self-cooling during 10 min. After that, the spin coated wafers were exposed applying SUSS_MA6_BA6 mask aligner with an exposure dose of 100 mJ/cm² in soft contact mode where the photomask and the wafer were pressed together. After the exposure, the wafer was kept in the wafer-box for another 10 minutes before being

processed within subsequent technological steps. Then, the exposed wafers were developed in AZ developer that was mixed with deionized (DI) water in ratio 1:1 by volume. A development time that was manually controlled for each wafer takes around 1 minute. After development, the wafers were rinsed in DI water and dried with nitrogen flow. Afterwards, developed wafers were processed with a hard bake step at temperature of 130℃ for 2 minutes.

Structuring of deposited metal layers was made within several etching steps. The top titanium layer was etched in a mixture of water (60ml), hydrogen peroxide (40ml) and ammonia (20ml). Prepared mixture was kept for 15 minutes before being used. Wafers were etched during 2-3 minutes and then rinsed in DI water and dried with the nitrogen flow. Aluminum was structured in ANPE aluminum etcher. The etcher was heated up to 40℃ and etching was completed within 5 min. The etching duration was manually controlled for each wafer. In order to remove the adhesive titanium layer, the wafers were etched again in the titanium etcher for approximately 15 seconds.

After the etching, the photoresist was removed from the wafers in Technistrip NI555 remover during 5 minutes with following rinsing in a DI water. A necessity of the remover application instead of commonly used acetone is conditioned by a rapid acetone evaporation that creates a temperature impact on the wafers. The application of an ultrasonic bath for lithium niobate wafers is also undesirable because it can accumulate a mechanical stress or even break the wafers. Afterwards, manufactured structures were analyzed with the optical microscope. The examples of fabricated IDT structures are demonstrated in Figure 4.2 and Figure 4.3
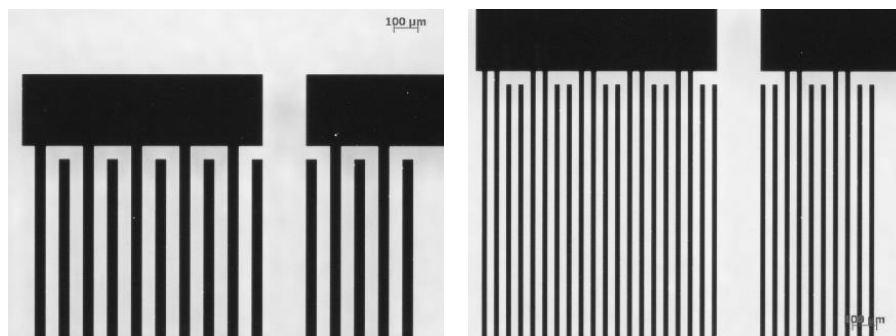
Figure 4.2. Microscope images of fabricated IDTs of SAW structures.

The fabricated IDTs are well performed without any structure underetching or shortcutting voids after several etching processes for separate metal layers.
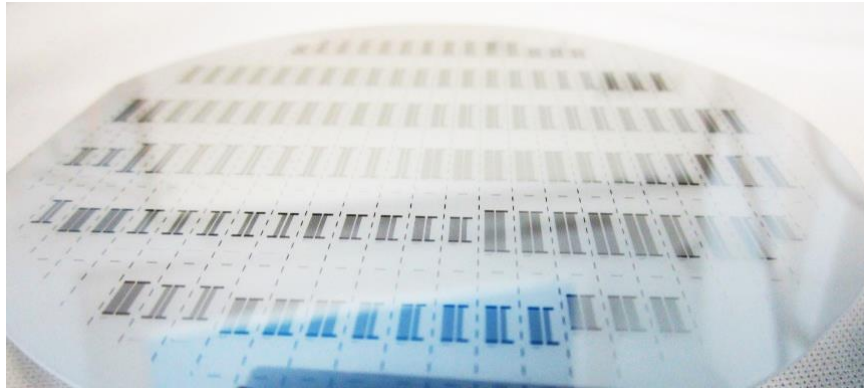
Figure 4.3. Fabricated SAW structures, full wafer view

4.4. Technology of microfluidic structure manufacturing

The manufacture of the microfluidic phononic structure was completed atop of fabricated IDTs as a system of periodically placed channels closed from the top and the bottom by polymer layers. In current work, both microfluidic structure and covering (interfacial) layers were fabricated utilizing the SU-8 polymer. The schematic representation of manufactured structure is shown in Figure 4.4.
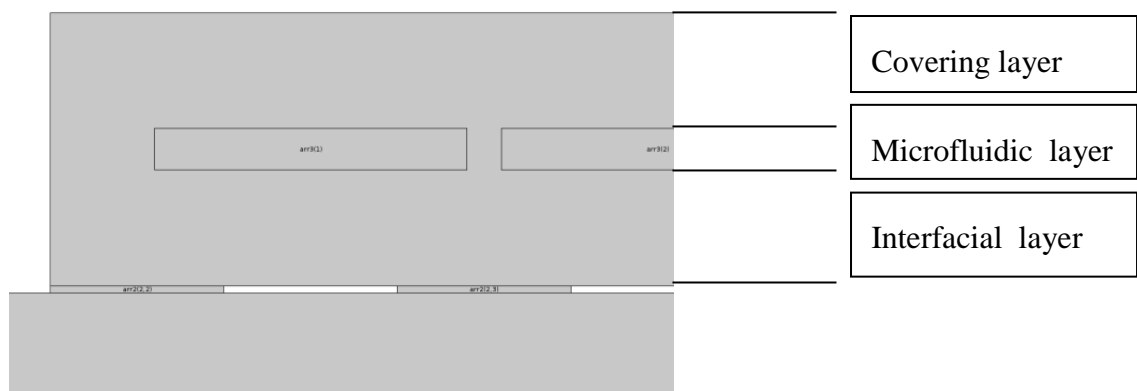
Figure 4.4 Designed layered arrangement of phononic structure based on an array of periodic microfluidic channels.

As it can be seen, the SU-8 phononic structure is restricted by IDTs area and directly defined atop of them. In order to complete the structure, the wafer has to be processed with two structured SU-8 layers. Initially, interfacial SU-8 layer should be defined atop of the IDTs area. After that, microfluidic channels have to be structured atop of the fabricated interfacial layer. Wafers with already fabricated SAW structures and alignment marks (Figure 4.3) were used in this process.

In current case, the technological approach of developed multilayer structure manufacturing should be changed in contrast to standard SU-8 layers processing. When the initial interfacial layer is completely processed and developed, a spin coating of following microfluidic SU-8 layer will be a non-uniform. Considerably thick elements of the interfacial layer will not allow a uniform distribution of the spin coated SU-8. The solution can be found by application of a spray coating technique or by optimizing the multilayer processing. In current work, we applied the incomplete layers processing approach to fabricate the multilayer structure. The interfacial layer was not developed in this process, remaining as a uniformly distributed coating across the whole wafer. At the same time it was completely processed with baking and exposure steps. The idea behind of the process is a selective completion of the interfacial layer crosslinking of parts that should remain and keep the not exposed SU-8 on a wafer for the spin coating of a subsequent microfluidic layer. In this case the interfacial layer baking and exposure steps have to be done completely. The soft bake step should be made with manufacturer recommended parameters in order to reduce possible SU-8 shrinking after the exposure step. At the same time the post exposure bake (PEB) step also has to be done completely ensuring the polymerization of exposed parts of interfacial layer. In case when the PEB step is avoided, the generated during exposure acid, that initiate the SU-8 polymerization, will interact with subsequently spin coated SU-8, causing its uncontrolled polymerization. As a result, the multilayer structure can be significantly disturbed. Completion of the process according to the described approach allows manufacturing the multilayer structure with separately crosslinked layer that can be simultaneously developed.

The technological sequence of the interfacial and microfluidic layers fabrication is demonstrated in Figure 4.5.

a)

b)

c)

d)

e)

f)

g)
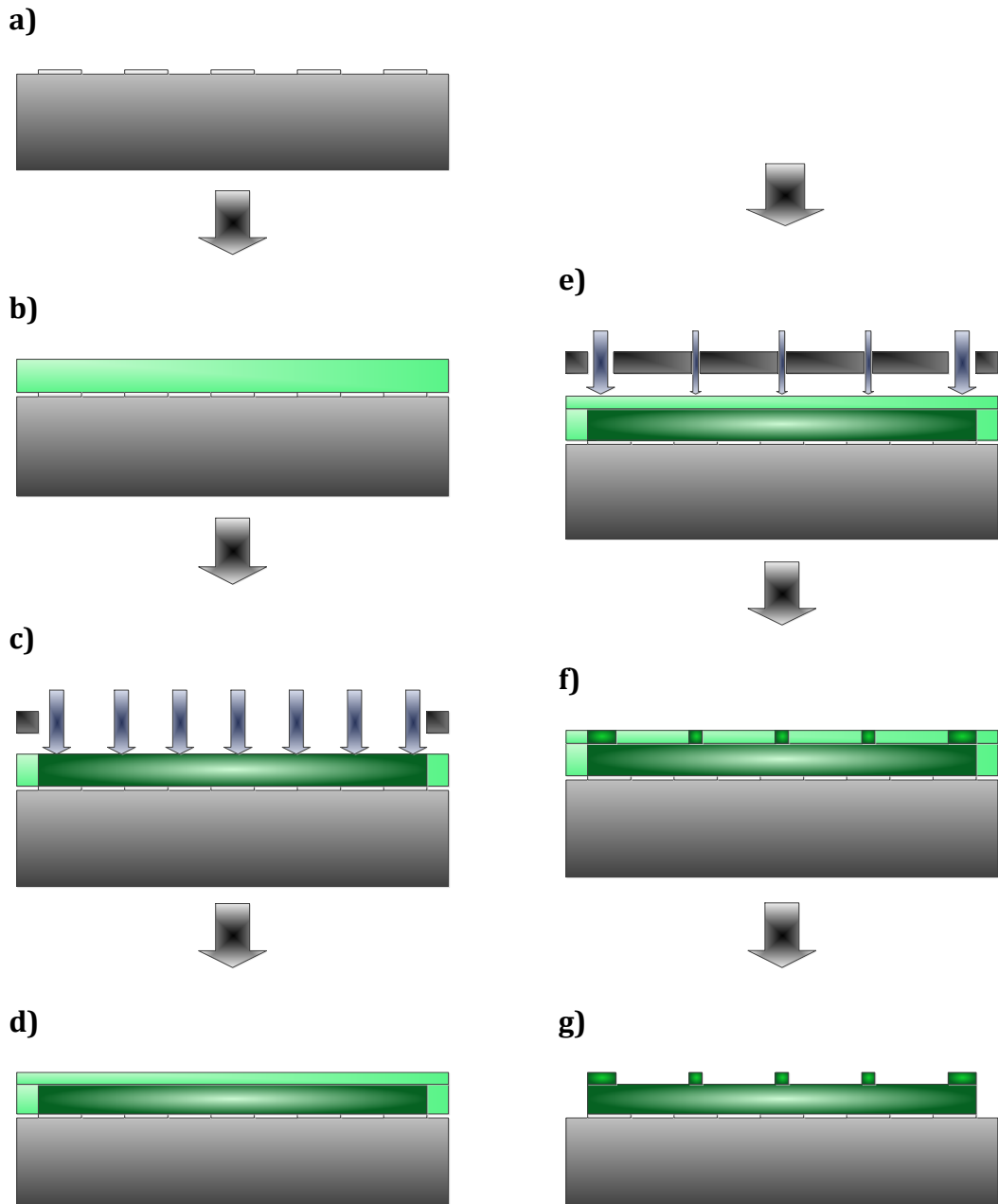
Figure 4.5 Process flow of fabrication of interfacial and microfluidic SU-8 layers.

The thickness of each of SU-8 layers has to be defined with a lower possible deviation from the predefined in structure design. For that reason, the experimental curves of SU 8 layer thicknesses depending on the rotation speed were recorded. Several rotation speed points for each fabricated layer were performed and layers thicknesses were analyzed with FRT profilometer. The layers processing (soft bake, exposure and PEB

parameters) was kept constant. Results of the thickness/rotation speed dependence for the interfacial layer are demonstrated in Figure 4.6.
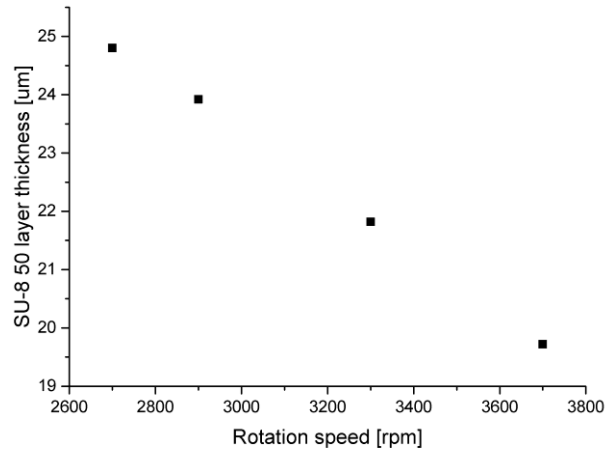
Figure 4.6 Dependence of the interfacial layer thickness on spin coater rotation speed for SU-8 50 polymer.

The respective dependence for the microfluidic layer applying SU-8 5 polymer was also analyzed. In this case the SU-8 coating was performed atop of another SU-8 layer and not on a clear wafer. Due to the SU-8 5 surface tension difference between the silicon wafer and fully processed SU-8, the distribution of SU-8 during the coating is different (for constant spin coating parameters). In a view of this fact, the calibration curve for SU-8 5 coated atop of SU-8 50 was recorded, Figure 4.7.
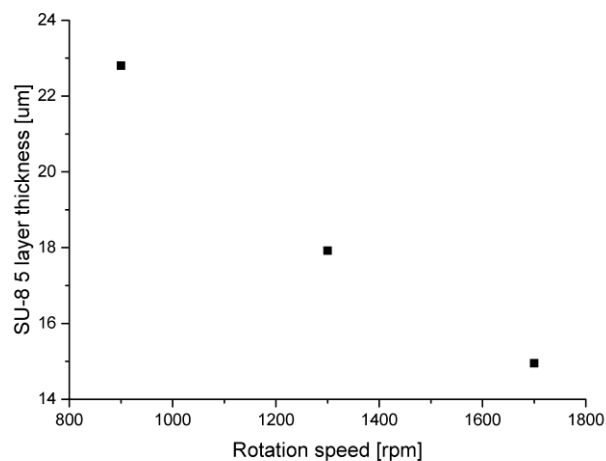
Figure 4.7 Dependence of the microfluidic layer thickness on the spin coater rotation speed for SU-8 5 polymer.

As it can be seen, spin coating parameters of SU-8 5 layer atop of already coated SU-8 50 are different from the parameters that are described by the manufacturer [93]. Experimentally achieved layers thicknesses exceed the described in a datasheet. That can be explained by reduced polymer distribution during the spin coating atop of another SU-8 layer caused by a change in the surface tension for distributing SU-8-5 (in comparison to the case where it is distributed atop of silicon or glass wafer).

Microfluidic structures were manufactured considering obtained experimental curves of layers thickness versus rotation speed. The interfacial layer of SU-8 50 was spin coated with rotation speed of 2700 rpm that corresponds to a layer thickness close to 25 μm (Figure 4.5 b). The spin coated wafer was soft baked at temperature of 65℃ for 3 minutes with following ramping of the hotplate to the temperature of 85℃ at which it was baked another 10 minutes. When the baking step was completed, the wafer was ramped back to the room temperature during 40 minutes. The edge bead removal with AZ EBR solvent was made after the completion of a soft bake. After that, the wafer was left for 5 minutes while the rest of EBR solvent evaporated from the surface of the wafer. Then, soft baked SU-8 layer was exposed in SUSS_MA6_BA6 in a contact exposure mode with an exposure dose of 160mJ/cm^2, define areas of the interfacial layer (Figure 4.5 c). Then the exposed wafer was post exposure baked (PEB) at 65℃ for 2 minutes, ramped up to 85℃ and baked another 10 minutes. Afterwards, it was ramped down back to room a temperature during 40 minutes. At this stage, the development of exposed SU-8 was omitted to keep the whole layer planar for spin coating of the microfluidic layer.

After the fabrication of the interfacial layer, the microfluidic layer was fabricated. SU 8 5 was spin coated directly atop of the undeveloped interfacial layer. The spin coater rotation speed was set to 1300 rpm. The expected layer thickness was 15 μm (Figure 4.5 d). The spin coated layer was soft baked at the temperature of 50℃ for 10 minutes. During that time the leveling of the coated layer took place. This step is required to reduce possible non-uniformity of a coated layer that can appear as a result of the surface disturbance of previously fabricated interfacial layer. As soon as leveling is completed, the hotplate temperature was ramped up to 65℃ where the layer was baked for 2 minutes. Then it was further ramped up to 85℃ and baked another 10 minutes. After the completion of baking, the wafer was ramped down to the room

temperature during 40 minutes. The edge bead removal with AZ EBR solvent was completed after the wafer was cooled down. After 5 minutes that is required for the rest of a solvent evaporation, the wafer was exposed in SUSS_MA6_BA6 mask aligner with an exposure dose of 160mJ/cm^2 (Figure 4.5 e). Afterwards, the exposed wafer was post exposure baked at 65℃ for 2 minutes with ramping to 85℃ and baking during another 10 minutes (Figure 4.5 f). Upon completion of the PEB, the wafer was ramped down back to the room temperature during 40 minutes. After the PEB step, the multilayer structure was developed in mr-Dev.600 developer (Figure 4.5 g). The development of interfacial and microfluidic layers simultaneously was finalized during 1.5 minutes.

The microscope image of the fabricated structure is demonstrated in Figure 4.8. Due to the transparency of SU-8 layers it is clearly observable that the SU-8 structure is precisely defined in the area of IDTs according to the initial design. As it was shown for the not split electrodes (Figure 4.8), the walls separating the channels are positioned directly in the middle of IDT finger electrodes.
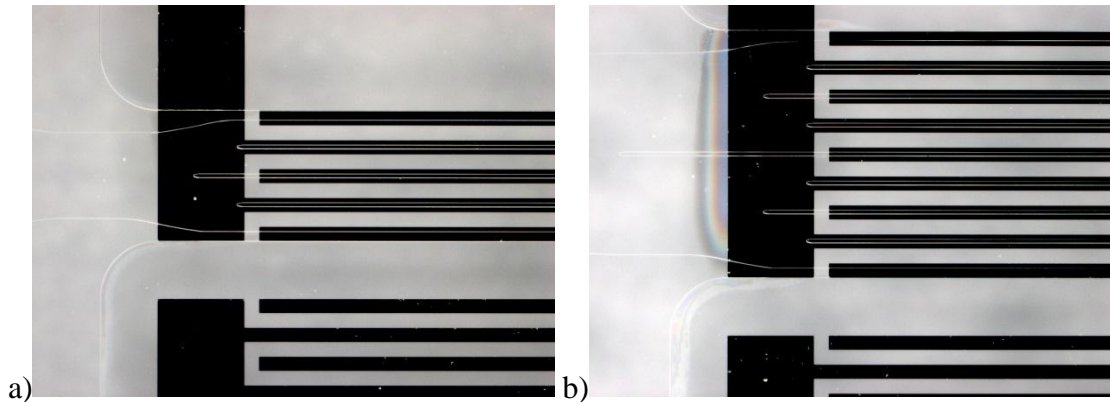
Figure 4.8 Fabricated SAW based phononic microfluidic structures with 4 a) and 8 b) channels

The microscope images of fabricated microfluidic structures with split IDT electrodes are demonstrated in Figure 4.9.
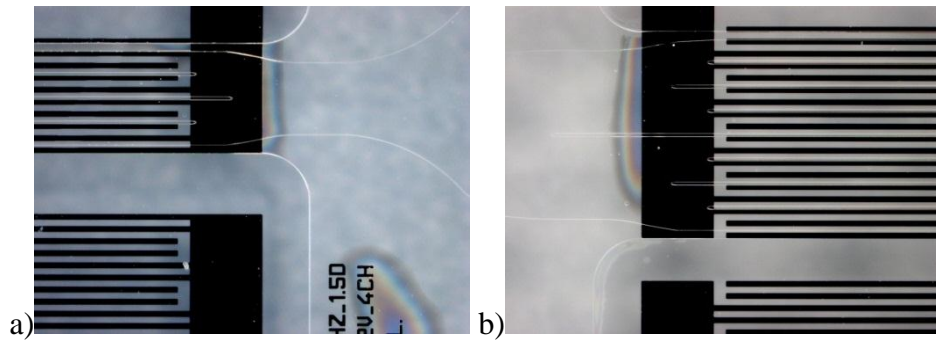
Figure 4.9 Fabricated SAW based (split electrodes) phononic microfluidic structures with 4 a) and 8 b) channels

In order to assess the SU-8 structure performance, the fabricated structures were investigated with scanning electron microscope (SEM). The obtained SEM images are demonstrated in Figure 4.10.
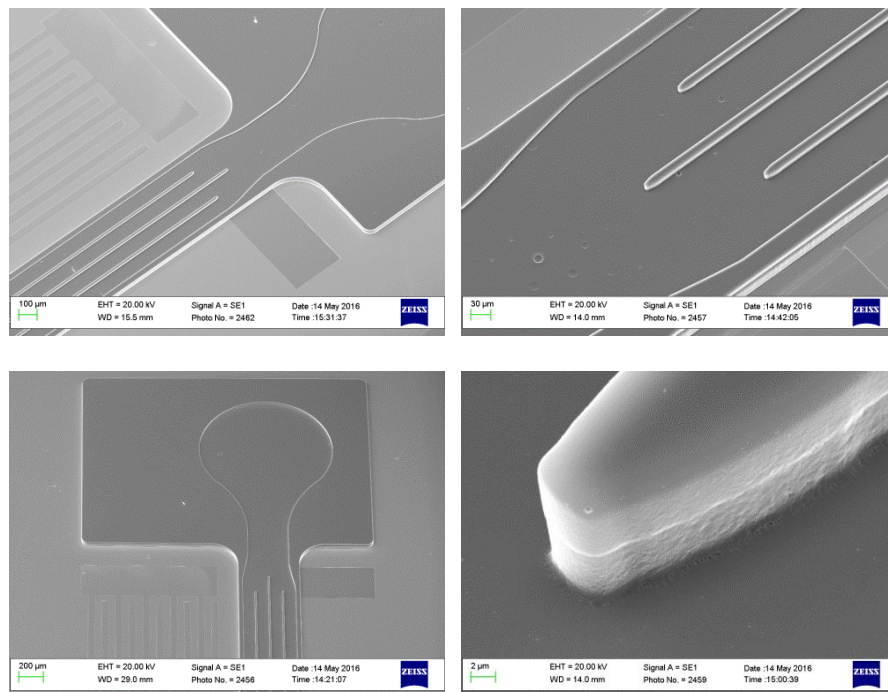
Figure 4.10 SEM images of fabricated microfluidic structures atop of interfacial layer

As it can be seen, microfluidic structures demonstrate a sufficient performance. The sidewalls are vertical with some disturbance in the middle that is probably caused by backscattering from the wafer back surface boundary. Afterwards structures fabricated at current stage were processed at the polymer bonding step where covering layers were defined for encapsulating of microfluidic channels.

4.5.   Polymer bonding technology

The application of the polymer based bonding technology for manufacturing of encapsulated microfluidic structures was applied in current work. It can be performed in several different ways. Depending on the utilized approach, the appropriate adjustment of the technological parameters of SU-8 processing should be considered. Additionally to that, each bonding approach requires a development of separate bonding recipe.

As it was previously demonstrated [91], in order to complete the bonding process for the multi-layered structures, at least one of bonding layers should not be completely polymerized. It is necessary to have functional groups of polymer chains on the surface of at least one of the bonding layers. Considering this condition, it becomes possible to initiate mutual crosslinking bonds between two bonding SU-8 coatings. The exposure dose and the post exposure processing define the final level of the SU-8 polymerization; therefore, the bonding adhesive layer should be fabricated under adjusted parameters. Another bonding approach is application of completely processed and only soft baked SU-8 layers. This process allows considerably reducing the bonding temperature, but at the same time soft bake parameters have to be optimized to avoid any leakage of SU-8 into the structure channels.

Referring to the sensor structure design, the top covering layer should have a thickness of 25 μm. The fabrication of that layer is more convenient on the basis of a handling wafer. Depending on the process, the covering layer can remain on a solid wafer during the bonding process; after the bonding it can be released in a releasing agent. As an alternative, it can be initially performed as a free-standing layer and bonded to a structure after being released. The application of the approach where SU-8 layer is coated on a wafer is an optimal solution that allows an easy handling. However, when the bonding is completed, releasing of the handling wafer is a very time consuming procedure. Due to the reduced access of a releasing agent to the under-etching area, the covering layer releasing requires long underetching time in a developer solution during which the whole structure can degrade. On the other hand, an application of free-standing SU-8 covering layer, allows completing the releasing step more efficiently, but certain adjustments of layer fabrication parameters have to be considered.

4.5.1. SU-8 bonding technology applying of soft baked adhesive layers

Initially, the structure fabrication was completed applying of a covering SU-8 layer with soft baked adhesive layer coating in a bonding process. That covering layer was brought together with a completely cross-linked SU-8 multilayer microfluidic structure. The advantage of this bonding approach is in an ability to reach high percentage of the bonded area. It allows to complete the bonding process at relatively low bonding temperature that considerably reduces the internal mechanical stress of the structure. However at the same time, the adhesive layer fabrication has to be optimized in order to avoid any leakage of the SU-8 into the structure channels.

The bonding of two different SU-8 layers can be completed in a process when both layers are defined on a solid wafers or when free-standing covering layers are applied. The application of wafer coated covering SU-8 layer for the bonding process has a disadvantage of a long releasing duration. In some cases, the releasing across 4" wafer cannot be completed at all, because of a reduced access of the releasing agent to the releasing area. On the other hand, the application of free-standing layers, allows solving this problem. During the fabrication of the free-standing covering layer, it is not stuck between two solid wafers. The pilling of an under-etched part of the SU-8 layer constantly opens an access for the releasing agent that considerably speeds up the releasing process. A disadvantage of the free-standing SU-8 layers application is their tendency to shrink more considerably in comparison with the ones that are held on the wafer. The temperature expansion of SU-8 layers causes its expansion and as a result, it induces an internal stress within bonded layers that can cause the bonding breakage. The described effect can be reduced with reduction of the bonding temperature.

The covering layer was fabricated on a silicon wafer. Initially, wafer was baked at the temperature of 200℃ for 5 minutes. Then, the releasing agent was spin coated on a surface of the wafer. Omnicoat (Micro Resist Technology GmbH) is a well-known solution for a wet releasing [94–96]. It allows completing a wafer scale releasing without an application of thick under etching layers. The solution provides a relatively clean and low temperature releasing in standard developers such as MF319. In current process the Omnicoat was spun on the Borofloat glass wafer at rotation speed of 500 rpm in a volume of 2ml with following acceleration of 100 R/s to 1000 rpm at which it was distributed during 30 seconds. The bake step was performed at temperature 200 °C

for 1 min with following cooling down to room temperature without controlled ramping. Several Omnicoat coatings were spun one after another to ensure a complete releasing of the SU-8 layer. The coating was made with 5 subsequently deposited layers with baking at 200℃ during 1 minute for each of them. After that, the covering layer was completed. In current recipe the covering layer was made as a layered structure consisting of 20 μm thick completely processed SU-8 and 5 μm of only soft baked adhesive layer. That separation of the covering layer into the double layer structure affords to reduce a possible SU-8 leakage during the bonding process, hence only 5 μm thick soft baked layer is applied. The rotation speed for fully processed layer was increased to 3300 rpm. The spin coated layer was soft baked at the temperature 65℃ during 3 minutes. Hereafter, the temperature was ramped up to 85℃ at which the wafer was baked another 10 minutes. The layer edge bead removal was completed with AZ EBR solvent after what it was left for 5 minutes to allow the rest of the solvent to evaporate. Then, the fabricated SU-8 layer was exposed with an exposure dose of 160 mJ/cm^2 in SUSS_MA6_BA6 mask aligner. The covering layer post exposure bake was made at the temperature of 65℃ during 2 minutes with following ramping up to 85℃ where it was baked another 10 minutes and then cooled down to the room temperature during 40 minutes. After completion of the covering layer, another thin layer of SU-8 5 that serve as an adhesive during the bonding process was spin coated. The thickness of that layer should be approximately 5μm that is sufficient to complete the bonding. For this reason, atop of a manufactured cross-linked layer, SU-8 5 was spin coated with 2000 rpm rotation speed and then baked at the temperature of 65℃ during 2 minutes. As soon as baking time is over, the wafer was immediately removed from the hotplate and cooled down. The edge bead removal was made the same way as it was completed for a previous layer. After that, the wafer was immersed in MF319 developer for the covering layer releasing.

The covering layer was gently placed atop of the manufactured wafer with the interfacial layer and fluidic structures and additionally covered with another silicon wafer to obtain the uniform pressure across the bonding layer. The bonding process starts with the preheating step at the temperature of 45℃ during 3 minutes, the rest of surface contaminations and SU-8 solvents supposed to be removed. After that, the structure was pressed with fabricated microfluidic arrangement applying the pressure of 1000 mBar and heated up to 50℃. At this temperature, the structure was bonded during

30 minutes and then slowly cooled down to the room temperature. Then, the bonded with covering layer wafer was exposed with an exposure dose of 160 mJ/cm^2 and then post exposure baked at the temperature of 65°C during 2 minutes and 85°C for 10 minutes with following cooling down back to the room temperature during 40 minutes.

Described process was developed as an initial approach to complete the sensor structure. Applications of this technology allowed achieving a relatively high percentage of the bonding area completion. However, an appearance of the SU-8 leakage into the structure channels is a significant disadvantage of that approach.

4.5.2. SU-8 bonding of exposed polymer layers

Prior to the coating of a covering SU-8 layer, the handling wafer was tailored with a releasing agent. Similar to previously described process, the Omnicoat solution was applied. The wafers were then spin coated with SU-8 50 with rotation speed of 2700 rpm. The spin coating parameters remain identical to the previously used for interfacial layer. The obtained layer thickness was close to 25μm. A subsequent soft bake was performed at the temperature of 65 °C for 3 minute with following ramping to 85 °C where the layer was baked another 10 minutes. A repetition of the fabrication procedure for the interfacial and for covering layer allows achieving structure symmetry with respect to layers thicknesses.

The exposure step was performed directly before the bonding without subsequent post exposure bake. The main idea of this step is to bring the exposed and not cross-linked SU-8 layer to the bonding process. At the room temperature, crosslinking reactions are considerably slow, that keeps most of the exposed SU-8 not cross-linked before the processing at the bonding step. The bonding should be started directly after the exposure step. Additionally, in order to generate more crosslinking material, the exposure dose should be increased for the covering layer. In current recipe, the exposure dose was set to 500 mJ/cm². Such high exposure dose generates more crosslinking reactions for SU-8 50 layers and ensures completion of most of the bonding area.

During the bonding process, two wafers with fabricated structures and covering SU-8 layer were brought into contact under pressure in SB6e substrate bonder. The bonding process started with the preheating step at 65 °C for 3 min during which the rest of the

solvent evaporates. That allows avoiding the appearance of voids between two bonding layers. The preheating step was completed without contact between two wafers through separation with spacers. After preheating, wafers were brought into a contact and pressed together with 3000 mbar. Pressed wafers were heated up to 120 °C and bonded under this temperature for 1 hour. In the end of the process, the temperature of bonded wafers was ramped down to the room temperature and a pressure has been released. The temperature and the tool pressure during bonding process are shown in Figure 4.11 in details.
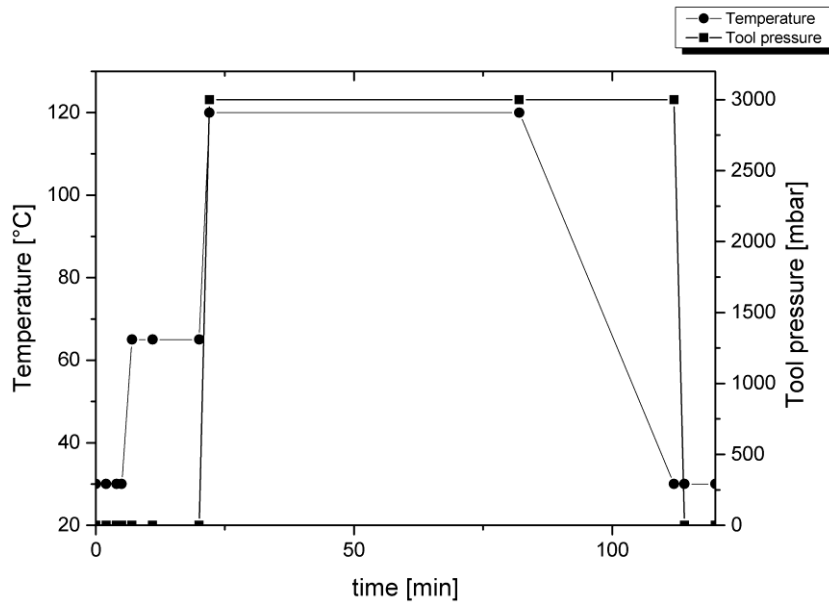
Figure 4.11 The temperature and pressure parameters applied during bonding process.

The experimental results showed that the soft bake is one of the considerably influencing parameters on the final SU-8 bonding performance. The soft bake controls a remained concentration of the solvent that directly affects mechanical properties of SU-8. The completion of a standard soft bake processing is optimal for achieving a high resolution of SU-8 structures; however, it is not always applicable for the multilayer processing or for the adhesive bonding. In presented process, SU-8 is applied as multilayer structure with subsequent bonding; thus, several features should be considered for the process parameter adjustment. During the completion of the multilayer structure, each previously processed SU-8 layer is exposed to the additional temperature treatment during subsequent layer coating. As a result, the initially

processed SU-8 layer is exposed to addition temperature impact. On the other hand, reduction of the SU-8 soft bake time and temperature affords to fabricate more flexible SU-8 layers due to the increased residual concentration of the solvent that can be easily processed in case of multilayer structures. The reduction of soft bake parameters (pre-bake 65 °C for 3 min and soft bake 85 °C during 10 min) allowed achieving more flexible SU-8 layer.

The bonding process has two temperature steps. The initial preheating step at 65 °C is required to complete a vaporization of the rest of the SU-8 solvent. During that bonding step, layers were separated by spacers and the tool pressure was not applied. Parameters of this preheating step are required to be adjusted. On the one hand, increased time and temperature can improve a solvent removal, but on the other hand, it completes a crosslinking of the adhesive layer that deteriorates the bonding quality. However, the insufficient preheating causes subsequent appearance of bonding errors (Figure 4.12a). It was experimentally revealed that optimal parameters of the bonding preheating step can be achieved at 65 °C with duration of 3 minutes. Bonding result with optimized preheating time is demonstrated Figure 4.12 b).

a)   b)
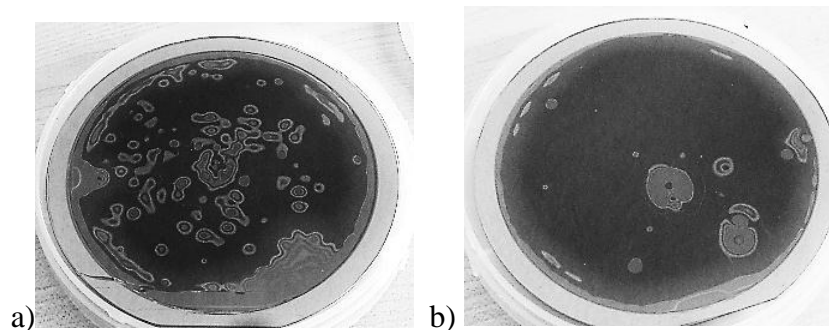
Figure 4.12 SU-8 – SU-8 bonding result on 4" silicon substrates with a different preheating time, 1 min a) and 3 min b).

The exposure dose of the pre-bonding exposure step is also one of the influencing parameters on the bonding performance because it controls a catalytic acid generation that assists crosslinking reactions. It was revealed experimentally that initially applied second exposure dose of 250 mJ/cm² for the adhesive SU-8 layer results bonding errors in the final structures. The increase of the second exposure dose up to 500 mJ/cm² provides a considerable improvement of the bonding performance. The completed

microfluidic structures were further characterized with a ZEISS SEM EVO50. Results are shown in Figure 4.13
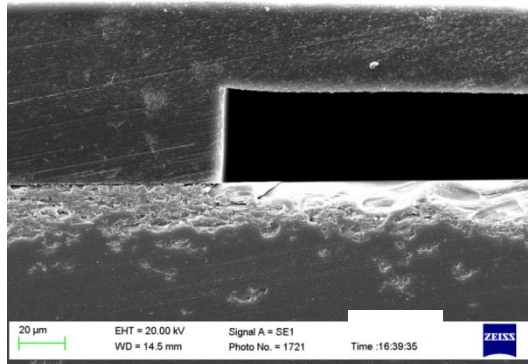
Figure 4.13 SEM images of completed microfluidic channel

Boundaries between SU-8 layers that are bonded together are hardly distinguishable due to the mutual crosslinking of polymer layers. The bonding appears to be uniform along whole bonding area without bonding errors and voids. The completed microfluidic channel within the bonding process has vertical sidewalls without SU-8 leakage inside the channel. Even within 1 micrometer scale, the bonding demonstrates no leakage of SU-8 and structure is completely bonded, Figure 4.14.
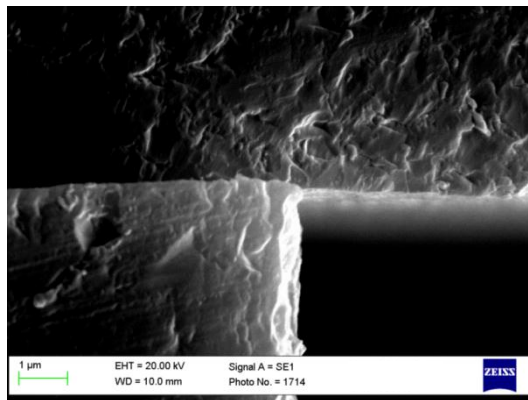
Figure 4.14 Bonding boundary between two SU-8 layers

Current bonding approach provides a possibility to create a micrometer scale structures bonding without disturbing them with the SU-8 leakage. This bonding process was utilized as a prime bonding process for the designed sensor fabrication.

5 SENSOR EXPERIMENTAL VERIFICATION

The sensor experimental verification was performed in order to confirm theoretical findings that demonstrated the sensor ability to detect volumetric properties of liquids. Speed of sound is one of the informative parameters that reflects the liquid compressibility and, as a result, gains an access to sensing properties that are directly influenced by intermolecular interactions of liquid mixtures. It allows evaluating thermodynamic quantities of the liquid mixture and indicating possible deviations caused by a non-linear mixture behaviour. That non-linearity indicates the strength of possible appearing in analyte interactions. One of the vivid examples is mixtures of water and alcohols. In current experimental verification, the binary mixture of deionized water and 1-proponol was used. Despite the fact that 1-popanol has lower speed of sound then DI water, the binary mixture of that liquids results in an increase in speed of sound for the molar concentration up to 0,058. That phenomenon was demonstrated in [97]. It was shown that by adding of alcohols to water, the properties of the mixture are affected in two ways. Firstly, the alcohol acts as one of the mixture components contributing its physical and chemical properties. And secondly, the presence of alcohols modifies the molecular structure of the water that changes intermolecular interactions in the solution. Similar manner as it can be detected for water-alcohol binary mixtures, the sensor can be utilized for a broad variety of applications such as detection of interactions within bio-substances such as, protein-protein, protein - DNA,

antigen – antibody and many other interactions. On the other hand, the scope of this work does not cover the experimental verification of the sensor application for certain bio-substances analyses. It aims to demonstrate the ability to conduct the volumetric properties analysis within the novel microfluidic sensor platform that merges the advantages of microacoustic and ultrasonic velocimetry sensor approaches, rather than target a certain bio-medical or any other application.

5.1. Measurement setup

The sensor experimental verification was completed utilising a standard approach for SAW devices by measuring of S-parameters. The sensor was designed as the 2-port SAW device. Measurements of S_{21} - parameters were performed without addition of any matching circuits. Manufactured sensors were measured directly on a wafer utilizing high frequency probe station without single sensor dicing and packaging. On the one hand it can disturb the measurement results by contacting and reflections from the neighbouring structures. But on the other hand, this approach allows completing measurements of undisturbed by dicing and subsequent packaging processes samples. Due to the sensor is performed for operation at relatively low frequency (around 20MHz), the influence of measuring circuit can be significantly reduced. The external microfluidic part was also simplified to manual handling of analytes that afforded to analyse the solutions in an easiest way, avoiding a probable influence on measuring results by attached external fluidic system.

Manufactured SAW based phononic crystal sensor was characterized with network analyzer Agilent 4395A together with S-parameter test set Agilent 87511A (100 kHz-500 MHz) on SUSS Lab probe station utilizing high frequency probes. The measuring setup is demonstrated in Figure 5.1.
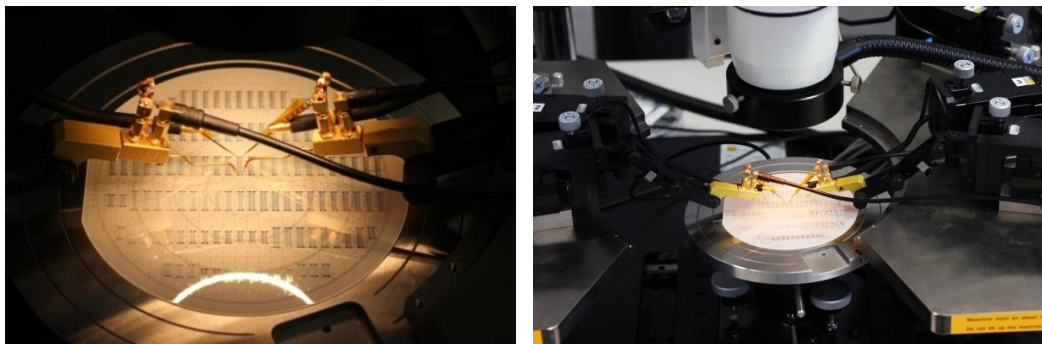
Figure 5.1 Wafer scale measurement setup utilizing the probe station.

Sensor S_{21}-parameter (transmission) magnitude and phase response were recorded simultaneously in a dual channel mode. A number of measuring points was set to the maximal device limit of 801 points. The frequency sweep type was defined as linear. An intermediate frequency (IF) bandwidth was set to 1 kHz and a source power was specified equal to 15 dBm. High frequency kelvin probes were connected to the network analyzer with CLF100 low loss coaxial cable and SSMC connectors. Analyzing liquid was manually filled in microfluidic channels with a micropipette. Experimental investigations were conducted with binary mixtures of water and 1-propanol. As it was discussed before, that binary mixture exhibits a non-linear behavior of speed of sound dependence on 1-propanol concentration at certain molar ratios. It can be easily handled without additional protection. It's not harmful and non-aggressive towards materials used in the experimental setup. At the same time the alcohol containing solutions are endowed with hydrophilic properties that assist to fill the microfluidic channels without applying an external pressure. The respective speed of sound and density data for water – 1-propanol mixture are shown in Table 1.

Table 1 Speed of sound and density for different compositions of DI water and 1-propanol [98]

Molar ratio, X	Density, kg/m³	Speed of sound, m/s
0 (DI water)	998	1483
0.021	990	1545
0.035	982	1578
0.056	974	1588
0.102	956	1531
0.158	933	1472
0.230	908	1421
0.347	881	1367
0.507	852	1233
1 (1-Propanol)	804	1220

5.2.　Measurement results

Initial investigations were aimed to select a frequency range that demonstrates a strong influence on the presence of liquids. Despite the expected frequency range that was obtained from simulations, possible technological tolerances could shift the sensor signal. For this reason, the analysis of the sensor response was completed in a broad band frequency range. The measurements were made for the sensor "clear" state where no liquid was filled into the channels as well as for mixture of water and 1-propanol with molar concentration of propanol equal X=0.021. An addition of considerably small portion of alcohol (in this case 1-propanol) considerably changes a surface tension of the liquid that allows filling the channels easily and removing the liquid when the measurement is completed.

The analysis of S_{21} - parameter (transmission) was completed and the results of amplitude response are shown in Figure 5.2.
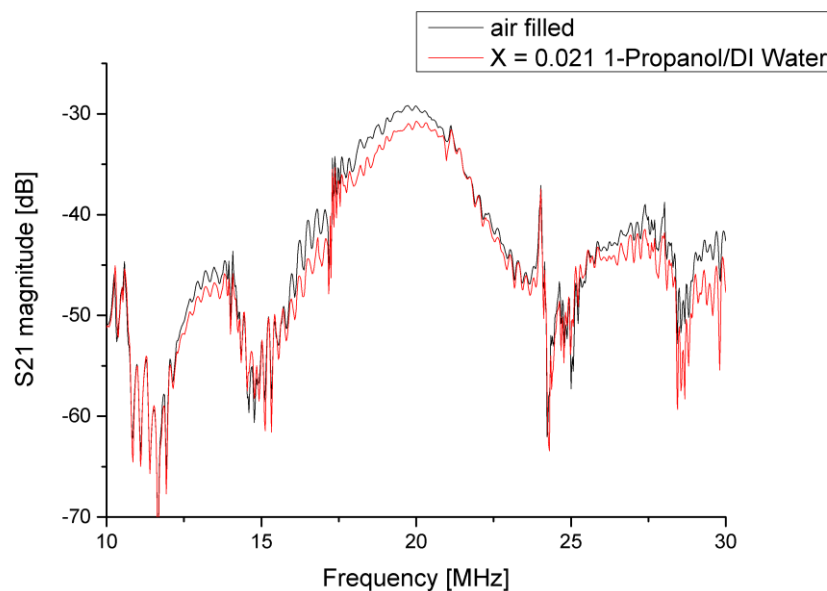
Figure 5.2 Sensor S_{21} parameter, amplitude response for air filled (black) and liquid filled channels (red)

As it can be seen, presence of the liquid is definitely causes a change in a transmission curve. However, in order to gain more information regarding exact position of respective frequency at which the liquid has most influence on sensor response, the phase frequency dependence should be taken into consideration. Based on completed numerical simulations, liquid that is filled into the channel has to influence the structure

response in a manner that it originates the appearance of analyte involving structure vibration modes. Position of that structure resonance has to be dependent on properties of the analyte. The phase response has to exhibit a rapid phase change at that specific frequency. Experimentally obtained results of the phase dependence for air filled channels and for the channels filled with DI water – 1-Propanol mixture of 0.021 molar ratio are demonstrated in Figure 5.3.
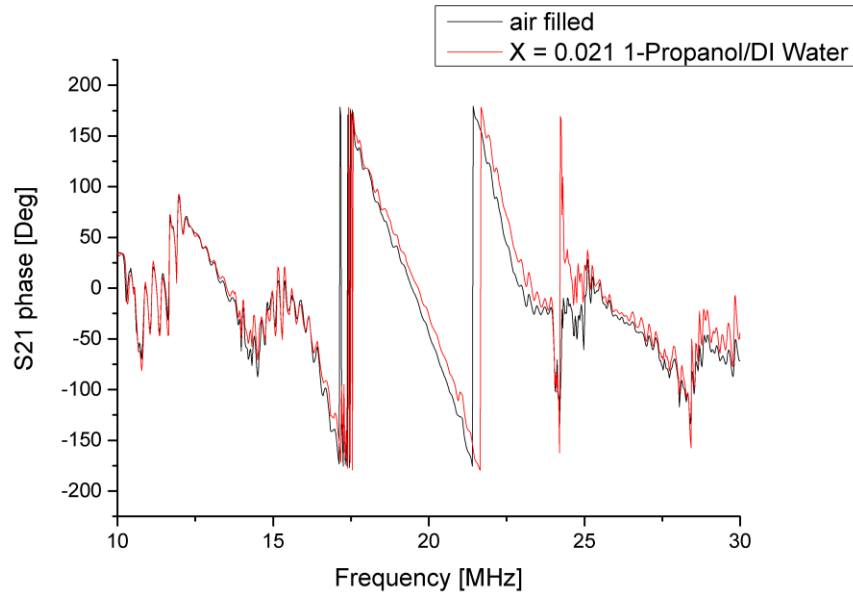
Figure 5.3 Sensor S21 parameter, phase response in degrees scale for clear state (blue) and filled with liquid (red)

Besides the obvious phase shift within the passband, the presence of the liquid (Figure 5.3 red curve) causes an appearance of rapid phase change in a frequency range between 24 and 25 MHz. That phase change indicates the origination of structure resonance that presumably has to be sensitive to the properties of the liquid that is filled into the channels. The rest of the phase response does not demonstrate a significant change caused by the liquid presence. The closer look at the frequency range of the rapid phase change provides two well-defined minima with the rapid phase change for each of them Figure 5.4. Nearly the same results were theoretically predicted where the appearance of two resonance modes of the structure were demonstrated (Figure 3.17).
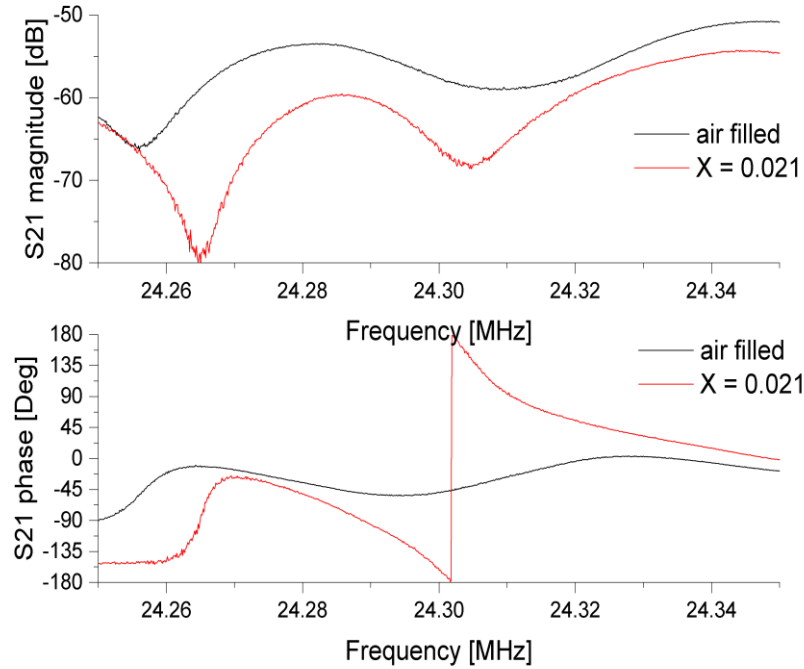
Figure 5.4 Sensor S_{21} parameter amplitude and phase response for air filled channels (black) and filled with water – 1-propanol mixture (X- 1-propanol molar ratio) (red)

In comparison to theoretically demonstrated results, experimentally measured curves are shifted to a higher frequency range. That mismatch with theoretical results can be explained by various technological factors that were discussed in the previous chapter. The change of geometry (especially channel thickness) or mismatched material properties of SU-8 that were estimated only with reference to literature sources could presumably result in the deviation of positions of structure resonances.

Results of numerical simulations demonstrated the appearance of two neighboring transmission minima with a frequency distance between them that is almost matching the experimental findings. As it was shown in chapter 3.4, the geometrical performance of fabricated microfluidic channels significantly affects the frequency difference between two structural resonances; therefore, the mismatch between experimentally obtained results and theoretical curves can be explained by finite technological tolerances of structure fabrication or, more specifically, by inclination of channels sidewalls. According to the performed numerical simulations, the 4˚ sidewalls inclination can cause a significant change of relative minima frequency positions.

As it can be seen on experimental curves (Figure 5.4), the higher frequency dip is much broader than the lower frequency. However, results of numerical simulations demonstrate that both minima should have comparable quality factor that contradicts the experimental observations. The eigenmodes analysis that revealed the structure eigenmode for the higher frequency resonance (Figure 3.23), demonstrated a significant involvement of the interfacial layer. Due to the interface between the interfacial layer and the surface of piezoelectric waveguide in current case is not under control and limited by only a low adhesion condition, the response of that specific minimum is partly damped. That increases the bandwidth of higher frequency resonance and makes the phase shift relatively smooth. The bandwidth of the higher frequency resonance can be also associated with an acoustic absorption of the analyte that is experimentally investigated later in this chapter.

The frequency region where the presence of the liquid is associated with appearance of structure resonances was analyzed with a higher resolution for several different liquid mixtures with known parameters of density and speed of sound, Table 1. As it was previously demonstrated in [56,60], the binary mixture of DI water and alcohols (1-Propanol in current case) is a convenient solution to test the sensor. At the same time, binary solutions of DI water and alcohols exhibit non-linear speed of sound dependence versus alcohol concentration. That feature allows distinguishing the speed of sound dependence of certain sensor system.

Thus, several binary mixtures of water and 1-propanol were analyzed with the manufactured microfluidic sensor. Each liquid mixture was manually filled into the channel, analyzed and subsequently completely removed. The microfluidic channels were dried with nitrogen flow. Results of experimental investigations of the amplitude response are shown in Figure 5.5. The respective phase response is shown in Figure 5.6.
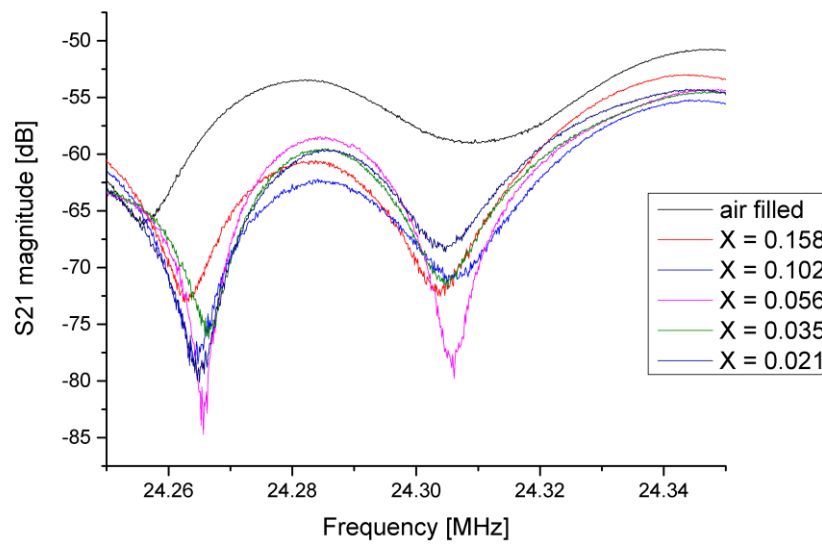
Figure 5.5. S21 – parameter amplitude response for water – 1-propanol mixture. 1-Propanol molar concentrations in a range of 0,021 – 0,158.
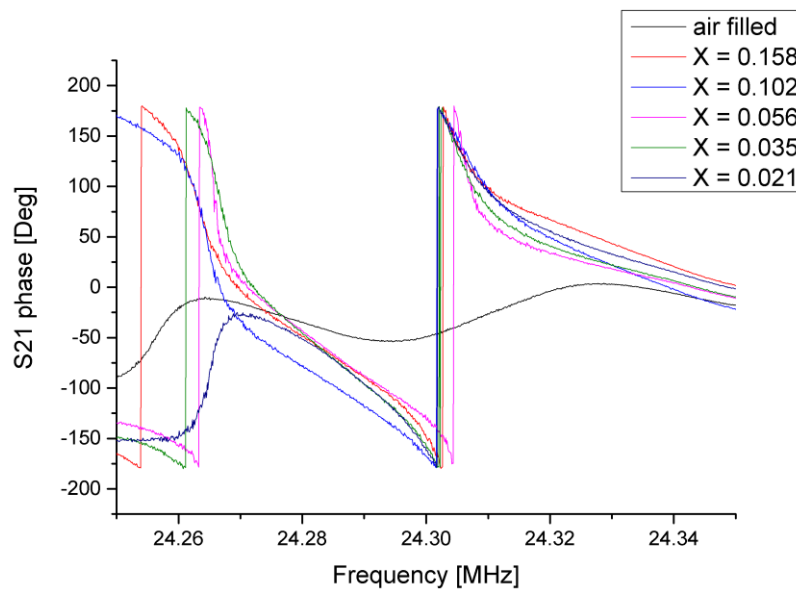
Figure 5.6. S21 – parameter phase response for water – 1-propanol mixture. 1-propanol molar concentrations in a range of 0,021 – 0,158.

S_{21} - parameter amplitude and phase responses demonstrate a frequency of transmission minima behavior that correlates with speed of sound for water – 1-propanol mixtures. The speed of sound data for that binary mixture and sensor response are demonstrated simultaneously in Figure 5.7. As it can be seen, the experimental curve and the data for

speed of sound of DI water and 1-propanol have a sufficiently high agreement with the mismatch at mixture lower concentrations. An initial increase of 1-propanol concentration shifts the transmission minimum to the higher frequency. The further raise of 1-propanol concentration turns the direction of the transmission minimum shift to the lower frequency range. The phase response provides the same analyte dependent behavior and corresponds to amplitude response measurements.
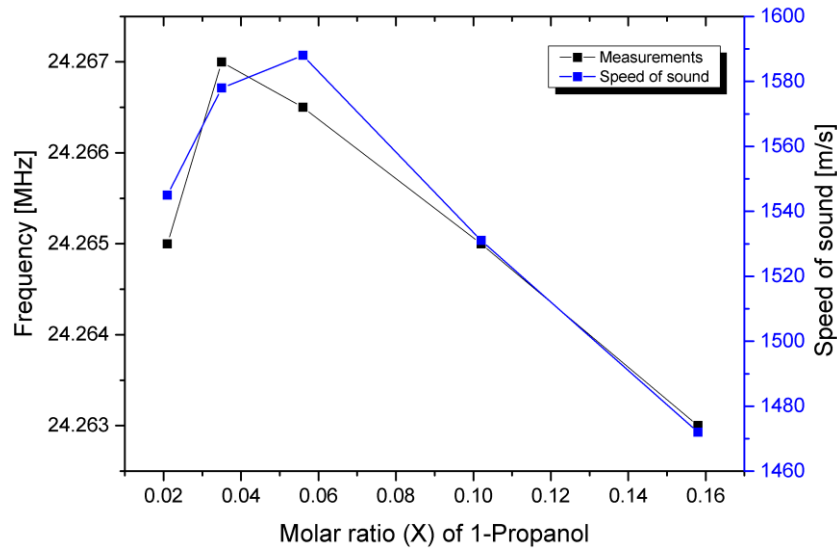
Figure 5.7. Dependence of transmission minima on speed of sound of binary mixture of water and 1-propanol for molar concentrations range of 0.021 – 0.158.

In order to confirm the experimentally achieved data for the sensor response, the water − 1-propanol concentrations with linear altering of speed of sound have been analyzed. Three different mixtures of water and propanol with the molar concentration of propanol equal X=0.23, 0.347 and 0.507 were chosen. At those molar ratios of 1-propanol, the binary mixture exhibits a linear relation to volumetric acoustic properties of each liquid separately. The non-linear mixture behavior that is associated with the change of the molecular structure of the liquid does not play a significant role at such considerably high alcohol concentrations. Results of the sensor S_{21} parameter measurements amplitude and the phase response are demonstrated in Figure 5.8.
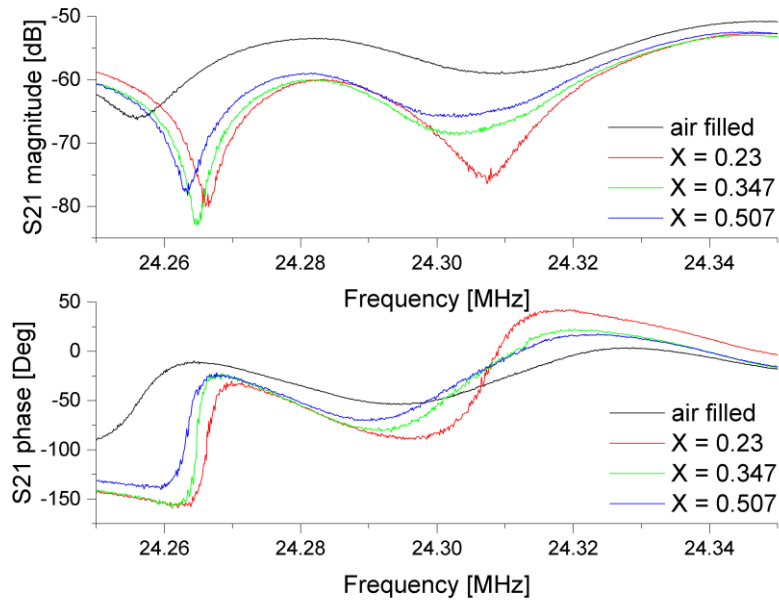
Figure 5.8 Sensor S21 parameter measurement results, amplitude response in a decibel scale and phase response in degrees scale

As it can be seen, the experimental curves of magnitude and phase response demonstrate a distinguishing sensor response on $1-$propanol concentration. Analogously to previous observation, the lower frequency transmission dip has a narrower bandwidth as the higher frequency one. The phase response demonstrates a gradual move accordingly with a magnitude response. The amplitude minima shift as well as the corresponding phase shift demonstrates a tendency to move in a direction of lower frequencies when the microfluidic channel is filled with a liquid with lower speed of sound. The response of the sensor structure on analyte speed of sound is summarized in Figure 5.9.
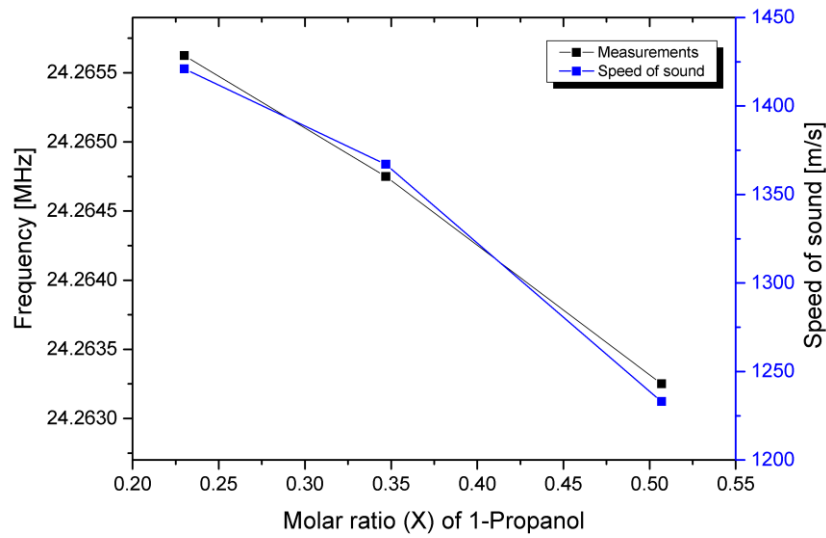
Figure 5.9. Dependence of transmission minima on speed of sound of binary mixture of water and 1-propanol for molar concentrations range of 0.23 – 0.507.

Experimental results (black curve) that are demonstrated in Figure 5.9 are in a good agreement with the speed of sound data (blue curve) for the analyzed liquid mixture. In both cases of linear and non-linear speed of sound behavior of analyzed liquid, the sensor response that is taken as a frequency of the transmission dip of the structure resonance correlates with speed of sound of the analyte. The lower frequency transmission dip bandwidth is almost irrelevant to the analyte and remains stable. Only the frequency position depending on speed of sound of liquid filling the channels is changed.

It should be noted that both observed transmission minima depend in a similar manner on analyte speed of sound as that was theoretically predicted; however, the band width of the second one deviates more considerably from one probe to another. Depending on properties of liquid analyte it changes in frequency of transmission minimum, band width and magnitude. Hence, the influence on the bandwidth can be a subject of sound absorption change, thus the associated data for different compositions of water – 1-propanol were considered [98]. A combination of the data of variation of magnitude of the higher frequency transmission dip and literature data of the sound absorption for binary mixtures of DI water and 1-propanol has revealed a conformal dependencies variation that depends on molar ratio of 1-propanol, Figure 5.10.
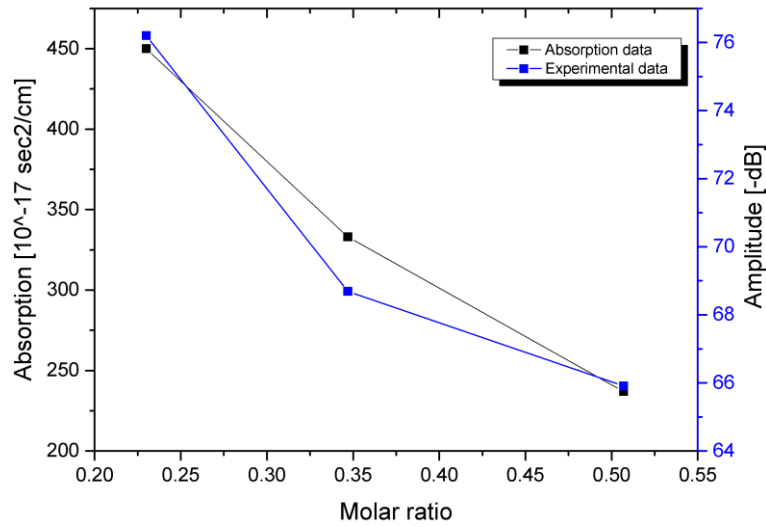
Figure 5.10. Dependence of sound absorption (literature data) and magnitude of higher frequency transmission dip for DI water and 1-propanol mixtures.

As it can be observed, the experimental data curve is in conjunction with the dependence for the sound absorption data. The higher absorption provides a dipper transmission minimum as a result and vice versa, in case of lower absorption, the transmission minima is more pronounced. That observation contradicts the classical understanding of a liquid cavity resonator, where the bandwidth should deteriorate in case of higher absorption. In current case, the structure response dependent on complex structure vibration with structural resonances that involve the analyzed liquid. The interplay between different resonating modes can initiate the case where a damping of one mode results in the variation of another structure mode distributing the localized acoustic energy. That explanation introduces rather complex structure behavior but allows to describe an unexpected dependence on the sound absorption.

In order to verify an influence of the analyte sound absorption on the structure response, similar experiment but with the use of standard alcohols was performed. The results of measured amplitude and phase responses are demonstrated in Figure 5.11.
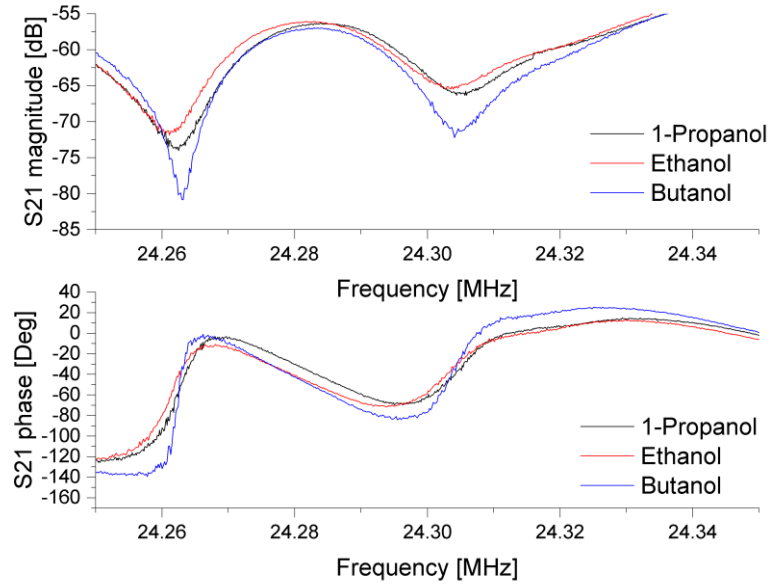
Figure 5.11 S_{21} – parameter amplitude and phase responses for different alcohols (1-propanol (black), ethanol (red), butanol (blue).

The experimental results show the obvious difference between measured dependences for standard alcohols. The range of speed of sound for measured liquids is not broad, as a result the frequency shift of transmission minima is relatively small. The summarized sensor response and speed of sound data for alcohols applied in current experiment are shown in Figure 5.12.
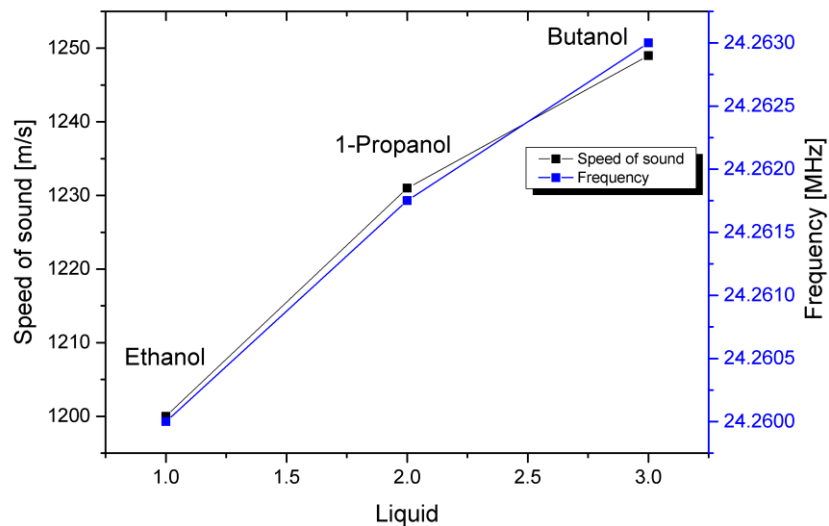
Figure 5.12. Dependence of transmission minima on speed of sound of standard alcohols (ethanol, 1-propanol, butanol) [98].

At the same time the difference in the sound absorption, especially, in case of butanol is considerable. The literature data for sound absorption and the amplitude of higher frequency transmission minima are brought together in Figure 5.13.
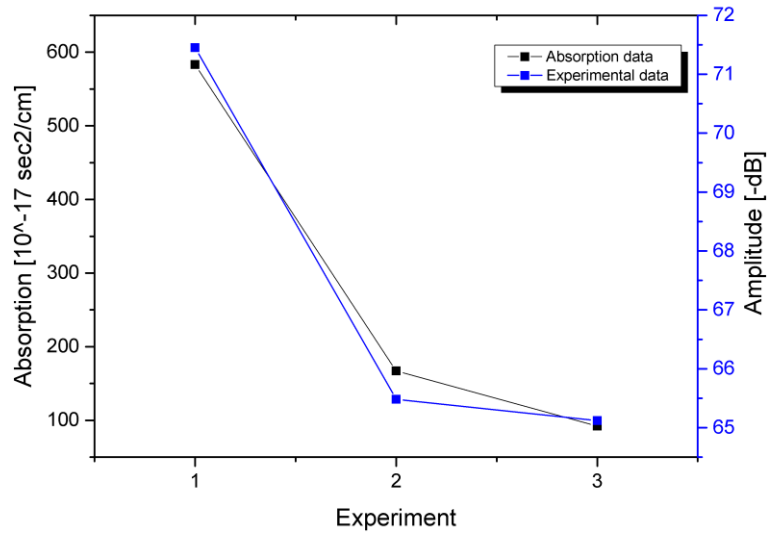
Figure 5.13. Dependence of sound absorption (literature data) and magnitude of higher frequency transmission dip for Butanol, 1-propanol and Ethanol.

It can be concluded that previous observations of influence of sound absorption on transmission minima are confirmed in case when channels of the structure are filled with standard alcohols. As it was previously observed, the higher sound absorption affects the band width and the amplitude of transmission minima in a way where the highest absorption provides a dipper transmission minimum.

At the same time it should be mentioned that in case of low 1-propanol concentrations, the correlation between the sound absorption and the magnitude of higher frequency transmission dip was not observed. Despite an experimental confirmation of the sound absorption on structure resonances for higher alcohol concentrations and for standard alcohols, the lower concentrations of water − 1-propanol do not fit to that scheme. An explanation of that observation can be associated with a significant variation of surface tension of water − 1-propanol mixture. The hydrophobic properties of the channels sidewalls can cause incomplete structure filling introducing a measurement errors. As a result the sensor response at low alcohol concentrations can be presumably deteriorated.

Summing up the obtained experimental results, it can be stated that expected dependence on speed of sound of the sensor structure is confirmed and the transmission minima that are associated with structure resonances follow the variation of speed of sound of analyzing liquid. At the same time the experiment revealed that the structure response is changed regarding the bandwidth and minima magnitude depending on the analyte. The association of amplitude of transmission minima with sound absorption has shown a considerable correlation. Obtained experimental results have shown some deviation from theoretically predicted findings that can be reduced with an improved structure fabrication process.

6 CONCLUSIONS

In this work a novel liquid sensor concept that utilizes the system of periodically placed microfluidic channels was introduced. The concept merges advantages of the SAW sensor platform and ultrasonic velocimetry methods. It was shown that application of the phononic crystal sensor concept for micrometer scale sensor structures allows obtaining the sensor system that is sensitive to volumetric liquid properties. In contrast to previously utilized sensor systems for detection of volumetric properties of analytes, developed sensor approach allows to achieve sensor performance that is compatible with Lab on a Chip planar platforms.

Current work is more particularly focused on the study of structure resonances of periodical arrangements in terms of the sensor application. It was demonstrated that utilization of SAW platform features with complexity of coupling of surface waves to the structure avoiding scattering into the bulk. It was shown that one of the promising approaches is the localization of the energy within the periodic arrangements by exciting structure resonance modes. Completing the periodic arrangement with liquid constitutes allows obtaining the structure response that is dependent on the material properties of the liquid domains.

Obtained theoretical results were confirmed with experimental investigations of the manufactured structure. In conjunction with theoretical predictions, the fabricated sensor structure responded to material properties of analyzed liquid (speed of sound). In addition to expected results, experimentally obtained dependences demonstrate a

correlation to sound absorption of the liquid analyte. That finding was observed in several experiments and theoretically fit to the physical model of investigated sensor structure.

Along with theoretical and experimental work, the respective sensor fabrication technology was developed. In order to withstand strong demands regarding structure performance, application of standard approaches was not sufficient. During the work, the optimal fabrication process was developed by the author. Each single technological step was personally validated and adjusted to withstand high structure tolerances.

Completed experimental investigations confirmed theoretically predicted findings. It was found that the sensor structure exhibits expected structure resonances that are dependent on material properties (speed of sound) of liquid analyte confined within the structure channels. It was found that the sensor structure has complex vibration behavior that contains a variety of structure localized modes. An experimentally revealed dependence of the structure response on analyte absorption confirms a rather complex interplay of structure resonance modes.

As a result of completed work, the SAW based phononic crystal sensor platform that merges the advantages of microacoustic and ultrasonic velocimetry approaches was developed. Experimentally obtained results proof the theoretically shown structure behavior. The sensor is performed as a Lab-on-a-Chip compatible planar SAW structure with integrated above system of periodically arranged microfluidic channels. The results of current work can be used for further developments in direction of SAW based sensors for detection of volumetric properties of liquid in biomedical and many other applications.

6.1. Achieved results

As a result, the concept of a phononic crystal sensor completed as an array of microfluidic channels was developed. It was shown that the new approach of the PnC sensor realization provides an ability of considerable reduction of known problems of scattering of incident surface acoustic waves into the bulk. Depending on the PnC structure design and a way of the acoustic wave excitation, the optimized structure exhibits isolated resonances that were found to be appropriate for the sensor application. It was shown that the incident surface acoustic wave is efficiently couples to the

periodic microfluidic arrangement. The sensor realization required a certain technology that was developed within the framework of completed research. The developed fabrication processes for the multilayer structure manufacturing and processes of adhesive bonding allowed to complete the PnC structure as an array of periodical closed microfluidic channels. Experimental investigations completed with several prototype sensors confirm the theoretical predictions. The measuring scheme and the sensor performance were considerably improved that afford to achieve the enhanced sensor performance in comparison to previously demonstrated solutions.

6.2.   Contributions

Presented work combines multiple tasks that were completed. The following author's contributions can be underlined.

1. The theoretical analysis and design of SAW structures with finite element analysis software COMSOL^{TM} Multiphysics. Design of IDTs and their geometrical parameters. Design of apodized SAW structures with Remez algorithm. Development of lithography masks for designed SAW structures with Autodesk AutoCAD 2013 software.

2. Numerical simulations of the SAW based phononic crystal sensor completed with finite element analysis software COMSOL^{TM} Multiphysics. Bringing the simulation model in accordance with the SAW phononic sensor design defining piezoelectric domain anisotropic properties according to the lithium niobate 127.86° Y cut substrates that are applied for the sensor structures. Completion of three dimensional simulation models of the SAW structure and the periodic arrangement completed as an array of microfluidic channels made of SU-8 polymer. Analysis of modes of the periodic structure and its eigenmodes analysis. Analysis of the interactions of surface wave with periodic microfluidic structure and analysis of structural resonances in designed periodic arrangement utilizing the acoustic structure interaction module of COMSOL Multiphysics software. Validation of the geometry and material properties deviations as the factors that are influencing the structure response.

3. Developing of technology for the SAW devices manufacturing. Due to the fabrication process was not previously established in university labs, it was developed from the scratch within the framework of presented contribution.

4. Development of the SU-8 polymer based technology for manufacturing of complete closed SU-8 based microfluidic structures on solid state substrates. The developed technology includes processes of SU-8 adhesive bonding, technology of SU-8 multilayer microfluidic structures manufacturing, adjustment of technological parameters for achieving a reduced stress accumulated SU-8 polymer microfluidic structures.

5. Fabrication of SAW structures and SAW based phononic crystal sensors. Completion and adjustment of technological parameters for each step of the sensor manufacturing. Estimation of optimal technological conditions and evaluation of effect of their possible deviations.

6. Development of the experimental measuring setup for high frequency SAW devices. Evaluation of fabricated SAW based phononic crystal sensor arrangements with various liquids of interest. Data acquisition and analysis of obtained results

6.2.1. Journal publications

Following list of publications can be related to the work presented in current contribution.

1. A. Oseev, R. Lucklum, M Zubtsov, M.-P. Schmidt, N.V. Mukhin, Soeren Hirsch, SAW based phononic crystal microfluidic sensor - microscale realization of velocimetry approaches for the integrated analytical platforms applications, Sensors (2017) in press.

2. A. Oseev, N. Mukhin, R. Lucklum, M. Zubtsov, M.-P. Schmidt, U. Steinmann, A. Fomin, A. Kozyrev, S. Hirsch, Study of liquid resonances in solid-liquid composite periodic structures (phononic crystals) - theoretical investigations and practical application for in-line analysis of conventional petroleum products, Sensors and Actuators B: Chemical (2017) in press.

3. A. Oseev, N. V. Mukhin, R. Lucklum, M. Zubtsov1, M.-P. Schmidt, D. Redka, A. Kozyrev, S. Hirsch, Towards macroporous phononic crystal based structures for FBAR applications. Theoretical investigation of technologically competitive solutions, Microsystem Technologies (2017) in press.

4. A. Oseev, M.-P. Schmidt, S. Hirsch, A. Brose, B. Schmidt, Two-component dielectric dispersion impedance biosensor for in-line protein monitoring, Sensors and Actuators B: Chemical 239 (2017) 1213–1220.

5. A. Oseev, M. Zubtsov, R. Lucklum, Gasoline properties determination with phononic crystal cavity sensor, Sensors and Actuators B: Chemical 189 (2013) 208–212.

6. M.-P. Schmidt, A. Oseev, R. Lucklum, M. Zubtsov, S. Hirsch, SAW based phononic crystal sensor, technological challenges and solutions, Microsystem Technologies (2016) 1–7.

7. R. Lucklum, M. Zubtsov, A. Oseev, Phoxonic crystals—a new platform for chemical and biochemical sensors, Analytical and bioanalytical chemistry 405 (2013) 6497–6509.

8. M. Zubtsov, R. Lucklum, M. Ke, A. Oseev, R. Grundmann, B. Henning, U. Hempel, 2D phononic crystal sensor with normal incidence of sound, Sensors and Actuators A: Physical 186 (2012) 118–124.

9. M.-P. Schmidt, A. Oseev, C. Engel, A. Brose, B. Schmidt, S. Hirsch, Flexible free-standing SU-8 microfluidic impedance spectroscopy sensor for 3-D molded interconnect devices application, Journal of Sensors and Sensor Systems 5 (2016) 55–61.

6.2.2. Conferences

6.2.2.1.   As a presenting author with oral presentation

1. A Oseev, M Zubtsov, M-P Schmidt, S Hirsch, R Lucklum, SAW based microfluidic phononic crystal sensor, Surface Acoustic Wave Sensor & Actuator Symposium 2016, Dresden, Germany

2. A. Oseev, R. Lucklum, M. Zubtsov, M.-P. Schmidt, S. Hirsch, SAW Based Phononic Crystal Liquid Sensor with Integrated Periodic Microfluidic Channels, SENSORDEVICES 2016 : The Seventh International Conference on Sensor Device Technologies and Applications

3. A. Oseev, M.-P. Schmidt, R. Lucklum, M. Zubtsov, S. Hirsch, Phononic crystal based liquid sensor governed by localized defect resonances, IEEE, 2015.

4. M.-P. Schmidt, A. Oseev, R. Lucklum, S. Hirsch (Eds.), Technology towards a SAW based phononic crystal sensor, International Society for Optics and Photonics, 2015.

5. A. Oseev, R. Lucklum, M. Ke, M. Zubtsov, R. Grundmann (Eds.), Phononic crystal sensor for liquid property determination, International Society for Optics and Photonics, 2012

6.2.2.2. As a presenting author with poster presentation

6. A. Oseev, M. Zubtsov, R. Lucklum, Octane number determination of gasoline with a phononic crystal sensor, Procedia Engineering 47 (2012) 1382–1385.

6.2.2.3. As a co-author

7. A. Oseev, R. Lucklum, M. Zubtsov, M.-P. Schmidt, S. Hirsch, SAW based phononic crystal liquid sensor-Periodic microfluidic channels approach, IEEE, 2016.

8. R. Lucklum, M. Zubtsov, A. Oseev, A. Omar, A. Martinez (Eds.), Multidimensional metamaterial fluid sensor, IEEE, 2013

9. R. Lucklum, M. Zubtsov, M. Ke, A. Oseev, U. Hempel, B. Henning (Eds.), Determining liquid properties by extraordinary acoustic transmission through phononic crystals, IEEE, 2011

10. R. Lucklum, M. Zubtsov, A. Oseev, M.P. Schmidt, S. Hirsch, F. Hagemann, Towards a SAW based phononic crystal sensor platform, European Frequency and Time Forum & International Frequency Control Symposium (EFTF/IFC) 6702207 (2013) 69–72

11. R. Lucklum, M. Zubtsov, A. Oseev, M.P. Schmidt, S. Hirsch, F. Hagemann, Phononic Crystals and Applications (2013)

12. M.-P. Schmidt, A. Oseev, R. Lucklum, S. Hirsch (Eds.), Technology towards a SAW based phononic crystal sensor, International Society for Optics and Photonics, 2015.

6.3. Future work

Presented work is aimed to develop and realise a novel SAW based sensor device for the liquid properties analysis. The work is rather concentrated on proof of the concept than on the certain application. It specifically targeted to understand the novel sensor

approach based on a utilization of periodical structures combined with the SAW devices platform. The developed sensor investigations provided promising results. Despite the fact that further improvement is still requires with regard to the fabrication technology, obtained results demonstrates consistency of proposed solution that allows to integrate a periodic sensor arrangements into micrometre wavelength scale SAW platform. The proposed sensor platform gives an opportunity to utilise it for an analysis of extremely low liquid volumes that is a demanding feature for medical application as an example. The sensor periodic arrangement includes a microfluidic system, therefore, it can be directly applied as a liquid sensor probe. The presented sensor concept can be utilised as an in-line sensor to provide the direct control of bioprocesses and conduct a real-time detection. The application of the SAW based approach allows creating disposable sensors for point of care and many other applications. An ability of the developed sensor platform to be integrated into Lab-on-a-Chip platform opens access to its further utilisation as a part of a Micro Total Analysis Systems.

A broad variety of sensor applications can be considered for the developed sensor platform. In an upcoming work the sensor will be further developed, keeping the core sensor design and adjusting according the requirements for a certain application. It is expected that demonstrated sensor principles can lead to the development of a novel miniature sensor class allowing conducting a volumetric properties analysis of liquids in a micrometre wavelength scale.

7 APPENDICES

APPENDIX 1 SIMULATION MODEL GEOMETRY

Geometry element	Parameter	Value
IDTs	IDT width	50 µm
	IDT lattice constant	100 µm
	IDT thickness	0,5 µm
	Number of input IDTs	10
	Number of output IDTs	5
Waveguide	Material	Lithium Niobate
	Substrate cut	127.86° YX
	Length	2200 µm
	Width	100 µm
	Thickness	600 µm
Interfacial layer	Material	SU-8
	Length	450 µm
	Width	100 µm
	Thickness	25 µm
Microfluidic layer	Material	SU-8
	Length	450 µm
	Width	100 µm
	Thickness	15 µm
Covering layer	Material	SU-8
	Length	450 µm
	Width	100 µm
	Thickness	25 µm

PML in X direction	Material	Lithium Niobate
	Length	200 µm
	Width	100 µm
	Thickness	600 µm
PML in Y direction	Material	Lithium Niobate
	Length	2200 µm
	Width	100 µm
	Thickness	200 µm
Microfluidic channels	Number of channels	4
	Length	90 µm
	Width	100 µm
	Thickness	15 µm

APPENDIX 2 SIMULATION MODEL MATERIAL PROPERTIES

Material	Property	Value
Lithium niobate	Density	4700[kg/m^3]
	Elasticity matrix (order: xx, yy, zz, yz, xz, xy)	{2.02897e+011[Pa], 5.29177e+010[Pa], 2.02897e+011[Pa], 7.49098e+010[Pa], 7.49098e+010[Pa], 2.43075e+011[Pa], 8.99874e+009[Pa], -8.99874e+009[Pa], 0[Pa], 5.99034e+010[Pa], 0[Pa], 0[Pa], 0[Pa], 0[Pa], 5.99018e+010[Pa], 0[Pa], 0[Pa], 0[Pa], 0[Pa], 8.98526e+009[Pa], 7.48772e+010[Pa]}
	Coupling matrix	{0[C/m^2], -2.53764[C/m^2], 0.193644[C/m^2], 0[C/m^2], 2.53764[C/m^2], 0.193644[C/m^2], 0[C/m^2], 0[C/m^2], 1.30863[C/m^2], 0[C/m^2], 3.69548[C/m^2], 0[C/m^2], 3.69594[C/m^2], 0[C/m^2], 0[C/m^2], -2.53384[C/m^2], 0[C/m^2], 0[C/m^2]}
	Permittivity	{43.6, 43.6, 29.16}
Aluminum	Density	2700[kg/m^3]
	Young's modulus	70e9[Pa]
	Poisson's ratio	0.33
SU-8	Density	1200
	Young's modulus	2.92e9
	Poisson's ratio	0.22
DI-water	Density	1000[kg/m^3]
	Speed of sound	1500[m/s]

APPENDIX 3 SUMMARIZED TECHNOLOGICAL PROCESS

Step	Process	Technological parameters
1.	Physical vapor deposition (Lithium niobate wafers)	Material: Titanium Presputtering: Generator power: 200 Watt Duration: 8 minutes Sputtering: Thickness: 30 nm Generator power: 200 Watt Duration: 1 minute
2.	Physical vapor deposition (Lithium niobate wafers)	Material: Aluminium Presputtering – 400 W * 120 sek Generator power: 400 Watt Duration: 3 minutes Sputtering: Thickness: 500 nm Generator power: 400 Watt Duration: 5 minute
3.	Physical vapor deposition (Lithium niobate wafers)	Material: Titanium Presputtering: Generator power: 200 Watt Duration: 5 minutes Sputtering: Thickness: 100 nm Generator power: 200 Watt Duration: 3 minute

4.	Physical vapor deposition (Lithium niobate wafers)	Wafer backside sputtering Material: Aluminium Presputtering – 400 W * 120 sek Generator power: 400 Watt Duration: 3 minutes Sputtering: Thickness: 200 nm Generator power: 400 Watt Duration: 2 minute

5.	Lithography (Lithium niobate wafers)	Speen coating af adhesive TI prime layer
		Baking: 120˚C 2 min
		
		Processing of TI35ES photoresist:
		Soft bake: 100˚C 2 min
		Exposure: 100mJ/cm^2
		Developing:
		   - Developing solution: AZ developer
		   - Developing time:1 min
		Hard bake: 130˚C 2 min

6.	Wet etching (Lithium niobate wafers)	Titanium top layer structuring Solution: DI Water 60 ml + H_2O_2 40 ml + NH_3 20 ml Etching time: 2 min 30 s Room temperature
7.	Wet etching (Lithium niobate wafers)	Aluminium layer structuring Solution: ANPE aluminium etcher Etching time: 8 min 30 s Room temperature
8.	Wet etching (Lithium niobate wafers)	Titanium adhesion layer structuring Solution: DI Water 60 ml + H_2O_2 40 ml + NH_3 20 ml Etching time: 25 s Room temperature

9.	Lithography (Lithium niobate wafers)	Photoresist stripping Solution: NI555 Technistrip Duration: 5 min
10.	Lithography (Lithium niobate wafers)	Interfacial SU-8 layer processing Layer material: SU-8 50 Coating rotation speed: 2700 rpm Soft bake: - 65˚C 3 min - 85˚C 10 min Exposure: 160mJ/cm^2 Post exposure bake: - 65˚C 2 min - 85˚C 10 min
11.	Lithography (Lithium niobate wafers)	Microfluidic SU-8 layer processing Layer material: SU-8 5 Coating rotation speed: 1700 rpm Soft bake: - 65˚C 3 min - 85˚C 10 min Exposure: 160mJ/cm^2 Post exposure bake: - 65˚C 2 min - 85˚C 10 min Developing: Developing solution: mr-Dev600 Developing time: 2 min
	Lithography (Glass wafers)	Processing of releasing layer Layer material: Omnicoat Baking: 200ºC, 1 min

	Lithography
	(Glass wafers)
		Covering layer processing
		Layer material: SU-8 50
		Coating rotation speed: 3300 rpm
		Soft bake:
		   - 65˚C 3 min
		   - 85˚C 10 min
		Exposure: 160mJ/cm^2
		Post exposure bake:
		   - 65˚C 2 min
		   - 85˚C 10 min
		
		Layer material: SU-8 5
		Coating rotation speed: 2000 rpm
		Soft bake: 65˚C 3 min

	Lithography (Glass wafers)	Releasing of covering layer Releasing agent: MF319 developer Releasing time: 4 hours

	Substrate bonder
	(Lithium niobate wafers)
		Bonding of covering layer
		Bonding conditions:
		   - Preheating 45ºC 3 min
		   - Bonding 50ºC 30 min
		   - Pressure - 1000mBar

	Lithography (Lithium niobate wafers)	Crosslinking of adhesive layer Exposure: 160mJ/cm^2 Post exposure bake: 50˚C 30 min

8 REFERENCES

[1]   I.A. Koshets, Z.I. Kazantseva, Y.M. Shirshov, S.A. Cherenok, V.I. Kalchenko, Calixarene films as sensitive coatings for QCM-based gas sensors, Sensors and Actuators B: Chemical 106 (2005) 177–181.

[2]   V.I. Kalchenko, I.A. Koshets, E.P. Matsas, O.N. Kopylov, A. Solovyov, Z.I. Kazantseva, Y.M. Shirshov, Calixarene-based QCM sensors array and its response to volatile organic vapours, Materials Science 20 (2002) 73–88.

[3]   L.-x. Chen, X.-w. He, X.-b. Hu, H. Xu, Calixarene-coated piezoelectric quartz crystal sensor for the detection of organic amine in liquids, Analyst 124 (1999) 1787–1790.

[4]   H. Wohltjen, Mechanism of operation and design considerations for surface acoustic wave device vapour sensors, Sensors and Actuators 5 (1984) 307–325.

[5]   C. Steinem, A. Janshoff, Piezoelectric sensors, Springer Science & Business Media, 2007.

[6]   K. Mitsakakis, A. Tserepi, E. Gizeli, Integration of microfluidics with a love wave sensor for the fabrication of a multisample analytical microdevice, Journal of microelectromechanical systems 17 (2008) 1010–1019.

[7]   G. Kovacs, M.J. Vellekoop, R. Haueis, G.W. Lubking, A. Venema, A Love wave sensor for (bio) chemical sensing in liquids, Sensors and Actuators A: Physical 43 (1994) 38–43.

[8]   N. Barié, U. Stahl, M. Rapp, Vacuum-deposited wave-guiding layers on STW resonators based on LiTaO 3 substrate as love wave sensors for chemical and biochemical sensing in liquids, Ultrasonics 50 (2010) 606–612.

[9]   J.K. Kwan, J.C. Sit, Acoustic wave liquid sensors enhanced with glancing angle-deposited thin films, Sensors and Actuators B: Chemical 181 (2013) 715–719.

[10] H. Wohltjen, R. Dessy, Surface acoustic wave probe for chemical analysis. I. Introduction and instrument description, Analytical Chemistry 51 (1979) 1458–1464.

[11] D.R. Lide, 2001, CRC Handbook of Chemistry and Physics, CRC Press, Boca Raton, Florida, 2000.

[12] S. Shiokawa, T. Moriizumi, Design of SAW sensor in liquid, Japanese Journal of Applied Physics 27 (1988) 142.

[13] H.-W. Chang, J.-S. Shih, Surface acoustic wave immunosensors based on immobilized C60-proteins, Sensors and Actuators B: Chemical 121 (2007) 522–529.

[14] E. Gizeli, N.J. Goddard, C.R. Lowe, A.C. Stevenson, A Love plate biosensor utilising a polymer layer, Sensors and Actuators B: Chemical 6 (1992) 131–137.

[15] G. Kovacs, G.W. Lubking, M.J. Vellekoop, A. Venema (Eds.), Love waves for (bio)-chemical sensing in liquids, IEEE, 1992.

[16] G. Kovacs, A. Venema, Theoretical comparison of sensitivities of acoustic shear wave modes for (bio) chemical sensing in liquids, Applied Physics Letters 61 (1992) 639–641.

[17] J. Du, G.L. Harding, J.A. Ogilvy, P.R. Dencher, M. Lake, A study of Love-wave acoustic sensors, Sensors and Actuators A: Physical 56 (1996) 211–219.

[18] E. Gizeli, A.C. Stevenson, N.J. Goddard, C.R. Lowe, A novel Love-plate acoustic sensor utilizing polymer overlayers, ieee transactions on ultrasonics, ferroelectrics, and frequency control 39 (1992) 657–659.

[19] A.C. Stevenson, E. Gizeli, N.J. Goddard, C.R. Lowe, Acoustic Love plate sensors: a theoretical model for the optimization of the surface mass sensitivity, Sensors and Actuators B: Chemical 14 (1993) 635–637.

[20] SU-8: Thick Photo-Resist for MEMS, http://memscyclopedia.org/su8.html.

[21] P. Roach, S. Atherton, N. Doy, G. McHale, M.I. Newton, SU-8 guiding layer for love wave devices, Sensors 7 (2007) 2539–2547.

[22] K. Länge, B.E. Rapp, M. Rapp, Surface acoustic wave biosensors: a review, Analytical and bioanalytical chemistry 391 (2008) 1509–1519.

[23] U. Stahl, M. Rapp, T. Wessa, Adhesives: a new class of polymer coatings for surface acoustic wave sensors for fast and reliable process control applications, Analytica chimica acta 450 (2001) 27–36.

[24] R.L. Baer, C.A. Flory, M. Tom-Moy, D. Solomon (Eds.), STW chemical sensors, IEEE, 1992.

[25] E. Gizeli, N.J. Goddard, C.R. Lowe, A.C. Stevenson, A Love plate biosensor utilising a polymer layer, Sensors and Actuators B: Chemical 6 (1992) 131–137.

[26] A. Rasmusson, E. Gizeli, Comparison of poly (methylmethacrylate) and Novolak waveguide coatings for an acoustic biosensor, Journal of Applied Physics 90 (2001) 5911–5914.

[27] K. Saha, F. Bender, E. Gizeli, Comparative study of IgG binding to proteins G and A: nonequilibrium kinetic and binding constant determination with the acoustic waveguide device, Analytical Chemistry 75 (2003) 835–842.

[28] E. Gizeli, F. Bender, A. Rasmusson, K. Saha, F. Josse, R. Cernosek, Sensitivity of the acoustic waveguide biosensor to protein binding as a function of the waveguide properties, Biosensors and Bioelectronics 18 (2003) 1399–1406.

[29] M. Hoummady, A. Campitelli, W. Wlodarski, Acoustic wave sensors: design, sensing mechanisms and applications, Smart materials and structures 6 (1997) 647.

[30] E. Gizeli, M. Liley, C.R. Lowe, H. Vogel, Antibody binding to a functionalized supported lipid layer: a direct acoustic immunosensor, Analytical Chemistry 69 (1997) 4808–4813.

[31] E. Gizeli, J. Glad, Single-step formation of a biorecognition layer for assaying histidine-tagged proteins, Analytical Chemistry 76 (2004) 3995–4001.

[32] Y. Hur, J. Han, J. Seon, Y.E. Pak, Y. Roh, Development of an SH-SAW sensor for the detection of DNA hybridization, Sensors and Actuators A: Physical 120 (2005) 462–467.

[33] O. Tamarin, S. Comeau, C. Dejous, D. Moynet, D. Rebiere, J. Bezian, J. Pistre, Real time device for biosensing: design of a bacteriophage model using love acoustic waves, Biosensors and Bioelectronics 18 (2003) 755–763.

[34] A.F. Collings, F. Caruso, Biosensors: recent advances, Reports on Progress in Physics 60 (1997) 1397.

[35] M. Tom-Moy, R.L. Baer, D. Spira-Solomon, T.P. Doherty, Atrazine measurements using surface transverse wave devices, Analytical Chemistry 67 (1995) 1510–1516.

[36] D.D. Stubbs, S.-H. Lee, W.D. Hunt, Investigation of cocaine plumes using surface acoustic wave immunoassay sensors, Analytical Chemistry 75 (2003) 6231–6235.

[37] M.A. Cooper, Label-free screening of bio-molecular interactions, Analytical and bioanalytical chemistry 377 (2003) 834–842.

[38] H. Sigrist, A. Collioud, J.-F. Clemence, H. Gao, R. Luginbuehl, M. Saenger, G. Sundarababu, Surface immobilization of biomolecules by light, Optical Engineering 34 (1995) 2339–2348.

[39] R.D. Rai, R.K. Shukla, A.K. Shukla, J.D. Pandey, Ultrasonic speeds and isentropic compressibilities of ternary liquid mixtures at (298.15±0.01) K, The Journal of Chemical Thermodynamics 21 (1989) 125–129.

[40] F. Aliotta, J. Gapiński, M. Pochylski, R.C. Ponterio, F. Saija, G. Salvato, Excess compressibility in binary liquid mixtures, The Journal of chemical physics 126 (2007) 224508.

[41] Z. Shao, A.K. Mitra, Nasal membrane and intracellular protein and enzyme release by bile salts and bile salt-fatty acid mixed micelles: correlation with facilitated drug transport, Pharmaceutical research 9 (1992) 1184–1189.

[42] R.H. Austin, K.-W. Beeson, L. Eisenstein, H. Frauenfelder, I.C. Gunsalus, Dynamics of ligand binding to myoglobin, Biochemistry 14 (1975) 5355–5373.

[43] H. Frauenfelder, F. Parak, R.D. Young, Conformational substates in proteins, Annual review of biophysics and biophysical chemistry 17 (1988) 451–479.

[44] P. Choi, J. Bae, K. Takagi, Ultrasonic spectroscopy in bovine serum albumin solutions, The Journal of the Acoustical Society of America 87 (1990) 874–881.

[45] A.P. Sarvazyan, P. Hemmes, Relaxational contributions to protein compressibility from ultrasonic data, Biopolymers 18 (1979) 3015–3024.

[46] V.N. Tsarev, N.E. Iastrebova, N.P. Vaneeva, A.I. Kalinin, [The use of immunoenzyme analysis for the diagnosis of an anaerobic infection of the maxillofacial area], Stomatologiia 74 (1994) 38–40.

[47] C.-C. Huang, S.-H. Wang, P.-H. Tsui, Detection of blood coagulation and clot formation using quantitative ultrasonic parameters, Ultrasound in medicine & biology 31 (2005) 1567–1573.

[48] P. Vennemann, K.T. Kiger, R. Lindken, B.C.W. Groenendijk, S. Stekelenburg-de Vos, T.L.M. ten Hagen, N.T.C. Ursem, R.E. Poelmann, J. Westerweel, B.P. Hierck, In vivo micro particle image velocimetry measurements of blood-plasma in the embryonic avian heart, Journal of biomechanics 39 (2006) 1191–1200.

[49] L.S. Cohen, P.F. Escobar, C. Scharm, B. Glimco, D.A. Fishman, Three-dimensional power Doppler ultrasound improves the diagnostic accuracy for ovarian cancer prediction, Gynecologic oncology 82 (2001) 40–48.

[50] E.I. Bluth, C.R.B. Merritt, M.A. Sullivan, Ultrasonic Evaluation of the Stomach, Small Bowel, and Colon 1, Radiology 133 (1979) 677–680.

[51] J.D. Joannopoulos, S.G. Johnson, J.N. Winn, R.D. Meade, Photonic crystals: molding the flow of light, Princeton university press, 2011.

[52] M.M. Sigalas, E.N. Economou, Elastic and acoustic wave band structure, Journal of sound and vibration 158 (1992) 377–382.

[53] M.S. Kushwaha, P. Halevi, L. Dobrzynski, B. Djafari-Rouhani, Acoustic band structure of periodic elastic composites, Physical Review Letters 71 (1993) 2022.

[54] R. Lucklum, M. Zubtsov, A. Oseev, Phoxonic crystals—a new platform for chemical and biochemical sensors, Analytical and bioanalytical chemistry 405 (2013) 6497–6509.

[55] R. Lucklum, J. Li, Phononic crystals for liquid sensor applications, Measurement Science and Technology 20 (2009) 124014.

[56] R. Lucklum, M. Ke, M. Zubtsov, Two-dimensional phononic crystal sensor based on a cavity mode, Sensors and Actuators B: Chemical 171 (2012) 271–277.

[57] R. Lucklum, M. Zubtsov, A. Oseev, M.P. Schmidt, S. Hirsch, F. Hagemann (Eds.), Towards a SAW based phononic crystal sensor platform, 2013.

[58] A. Oseev, M. Zubtsov, R. Lucklum, Octane number determination of gasoline with a phononic crystal sensor, Procedia Engineering 47 (2012) 1382–1385.

[59] A. Oseev, M. Zubtsov, R. Lucklum, Gasoline properties determination with phononic crystal cavity sensor, Sensors and Actuators B: Chemical 189 (2013) 208–212.

[60] A. Oseev, R. Lucklum, M. Ke, M. Zubtsov, R. Grundmann (Eds.), Phononic crystal sensor for liquid property determination, International Society for Optics and Photonics, 2012.

[61] P.d. Flory, Statistical thermodynamics of liquid mixtures, Journal of the American Chemical Society 87 (1965) 1833–1838.

[62] O. Redlich, A.T. Kister, Algebraic representation of thermodynamic properties and the classification of solutions, Industrial & Engineering Chemistry 40 (1948) 345–348.

[63] Y. Tanaka, S.-i. Tamura, Surface acoustic waves in two-dimensional periodic elastic structures, Physical Review B 58 (1998) 7958.

[64] Y. Tanaka, S.-i. Tamura, Acoustic stop bands of surface and bulk modes in two-dimensional phononic lattices consisting of aluminum and a polymer, Physical Review B 60 (1999) 13294.

[65] T.-T. Wu, Z.-G. Huang, S. Lin, Surface and bulk acoustic waves in two-dimensional phononic crystal consisting of materials with general anisotropy, Physical Review B 69 (2004) 94301.

[66] T.-T. Wu, Z.-C. Hsu, Z.-G. Huang, Band gaps and the electromechanical coupling coefficient of a surface acoustic wave in a two-dimensional piezoelectric phononic crystal, Physical Review B 71 (2005) 64303.

[67] V. Laude, M. Wilm, S. Benchabane, A. Khelif, Full band gap for surface acoustic waves in a piezoelectric phononic crystal, Physical Review E 71 (2005) 36607.

[68] Y.-Z. Wang, F.-M. Li, W.-H. Huang, Y.-S. Wang, The propagation and localization of Rayleigh waves in disordered piezoelectric phononic crystals, Journal of the Mechanics and Physics of Solids 56 (2008) 1578–1590.

[69] T.-T. Wu, L.-C. Wu, Z.-G. Huang, Frequency band-gap measurement of two-dimensional air/silicon phononic crystals using layered slanted finger interdigital transducers, Journal of Applied Physics 97 (2005) 94916.

[70] S. Benchabane, A. Khelif, J.-Y. Rauch, L. Robert, V. Laude, Evidence for complete surface wave band gap in a piezoelectric phononic crystal, Physical Review E 73 (2006) 65601.

[71] K. Kokkonen, M. Kaivola, S. Benchabane, A. Khelif, V. Laude, Scattering of surface acoustic waves by a phononic crystal revealed by heterodyne interferometry, Applied Physics Letters 91 (2007) 83517.

[72] D.M. Profunser, E. Muramoto, O. Matsuda, O.B. Wright, U. Lang, Dynamic visualization of surface acoustic waves on a two-dimensional phononic crystal, Physical Review B 80 (2009) 14301.

[73] T.-T. Wu, W.-S. Wang, J.-H. Sun, J.-C. Hsu, Y.-Y. Chen, Utilization of phononic-crystal reflective gratings in a layered surface acoustic wave device, Applied Physics Letters 94 (2009) 101913.

[74] C. Campbell, Surface acoustic wave devices and their signal processing applications, Elsevier, 2012.

[75] M.-P. Schmidt, A. Oseev, R. Lucklum, M. Zubtsov, S. Hirsch, SAW based phononic crystal sensor, technological challenges and solutions, Microsystem Technologies (2016) 1–7.

[76] M.-P. Schmidt, A. Oseev, R. Lucklum, S. Hirsch (Eds.), Technology towards a SAW based phononic crystal sensor, International Society for Optics and Photonics, 2015.

[77]   J.-H. Sun, T.-T. Wu, Propagation of surface acoustic waves through sharply bent two-dimensional phononic crystal waveguides using a finite-difference time-domain method, Physical Review B 74 (2006) 174305.

[78]   A. Oseev, M.-P. Schmidt, R. Lucklum, M. Zubtsov, S. Hirsch (Eds.), Phononic crystal based liquid sensor governed by localized defect resonances, IEEE, 2015.

[79]   V. Tsvirkun, A. Surrente, F. Raineri, G. Beaudoin, R. Raj, I. Sagnes, I. Robert-Philip, R. Braive, Integrated III-V Photonic Crystal–Si waveguide platform with tailored optomechanical coupling, Scientific reports 5 (2015).

[80]   X. Li, Z. Liu, Coupling of cavity modes and guiding modes in two-dimensional phononic crystals, Solid state communications 133 (2005) 397–402.

[81]   J.S. Jensen, Phononic band gaps and vibrations in one-and two-dimensional mass–spring structures, Journal of sound and vibration 266 (2003) 1053–1078.

[82]   Y. Achaoui, A. Khelif, S. Benchabane, L. Robert, V. Laude, Experimental observation of locally-resonant and Bragg band gaps for surface guided waves in a phononic crystal of pillars, Physical Review B 83 (2011) 104201.

[83]   T.A. Anhoj, A.M. Jorgensen, D.A. Zauner, J. Hübner, The effect of soft bake temperature on the polymerization of SU-8 photoresist, Journal of Micromechanics and Microengineering 16 (2006) 1819.

[84]   A. Ezkerra, L.J. Fernández, K. Mayora, J.M. Ruano-Lopez, Fabrication of SU-8 free-standing structures embedded in microchannels for microfluidic control, Journal of Micromechanics and Microengineering 17 (2007) 2264.

[85]   MicroChem Corp, SU-8 50-100 Data Sheet, 2015.

[86]   S. Tuomikoski, S. Franssila, Free-standing SU-8 microfluidic chips by adhesive bonding and release etching, Sensors and Actuators A: Physical 120 (2005) 408–415.

[87]   R. Feng, R.J. Farris, Influence of processing conditions on the thermal and mechanical properties of SU8 negative photoresist coatings, Journal of Micromechanics and Microengineering 13 (2002) 80.

[88]   S. Keller, G. Blagoi, M. Lillemose, D. Haefliger, A. Boisen, Processing of thin SU-8 films, Journal of Micromechanics and Microengineering 18 (2008) 125020.

[89] B. Bohl, R. Steger, R. Zengerle, P. Koltay, Multi-layer SU-8 lift-off technology for microfluidic devices, Journal of Micromechanics and Microengineering 15 (2005) 1125.

[90] S. Li, C.B. Freidhoff, R.M. Young, R. Ghodssi, Fabrication of micronozzles using low-temperature wafer-level bonding with SU-8, Journal of Micromechanics and Microengineering 13 (2003) 732.

[91] M. Agirregabiria, F.J. Blanco, J. Berganzo, M.T. Arroyo, A. Fullaondo, K. Mayora, J.M. Ruano-Lopez, Fabrication of SU-8 multilayer microstructures based on successive CMOS compatible adhesive bonding and releasing steps, Lab on a Chip 5 (2005) 545–552.

[92] R.L. Barber, M.K. Ghantasala, R. Divan, D.C. Mancini, E.C. Harvey, Study of stress and adhesion strength in SU-8 resist layers on silicon substrate with different seed layers, Journal of Micro/Nanolithography, MEMS, and MOEMS 6 (2007) 33006.

[93] MicroChem Corp, SU-8 2-25 Data Sheet, 2015.

[94] P. Wang, K. Tanaka, S. Sugiyama, X. Dai, X. Zhao, Wet releasing and stripping SU-8 structures with a nanoscale sacrificial layer, Microelectronic Engineering 86 (2009) 2232–2235.

[95] D.E. Pesántez, E.K. Amponsah, A.P. Gadre, Wet release of multipolymeric structures with a nanoscale release layer, Sensors and Actuators B: Chemical 132 (2008) 426–430.

[96] E. Mitri, G. Birarda, L. Vaccari, S. Kenig, M. Tormen, G. Grenci, SU-8 bonding protocol for the fabrication of microfluidic devices dedicated to FTIR microspectroscopy of live cells, Lab on a Chip 14 (2014) 210–218.

[97] C.M. Sehgal, B.R. Porter, J.F. Greenleaf, Ultrasonic nonlinear parameters and sound speed of alcohol–water mixtures, The Journal of the Acoustical Society of America 79 (1986) 566–570.

[98] W. Schaaffs, K.-H. Hellwege, A.M. Hellwege, Molecular acoustics, Springer-Verlag, 1967.